Surface preparation and Mn states of (Ga,Mn)As investigated by means of soft- and hard x-ray photoemission spectroscopy

Dissertation zur Erlangung des
naturwissenschaftlichen Doktorgrades
der Bayerischen Julius-Maximilians-Universität Würzburg

vorgelegt von
Benjamin Schmid
aus Augsburg

Würzburg 2010

Eingereicht am:

bei der Fakultät für Physik und Astronomie

Gutachter der Dissertation:

1. Gutachter: Prof. Dr. R. Claessen

2. Gutachter: Prof. Dr. K. Brunner

Prüfer im Promotionskolloquium:

1. Prüfer: Prof. Dr. R. Claessen

2. Prüfer: Prof. Dr. K. Brunner

3. Prüfer: Prof. Dr. E. M. Hankiewicz

Tag des Promotionskolloquiums:

Doktorurkunde ausgehändigt am:

"Ist der Soldat auf sich alleine gestellt, muss er in der Lage sein, im Sinne des Auftrags zu handeln."

Zentrale Dienstvorschrift der Bundeswehr 3/11, Gefechtsdienst aller Truppen (zu Lande), Blatt 101, Bundesministerium für Verteidigung, Bonn (1988).

Contents

List of Figures

List of Tables

Abstract

The present thesis deals with surface treatment, material improvement, and the electronic structure of the diluted magnetic semiconductor (Ga,Mn)As. The two key issues are the preparation of clean surfaces and the observation of potential valence hybridizations in (Ga,Mn)As by means of photoemission spectroscopy.

Several cleaning methods are applied individually to (Ga,Mn)As and their effects are compared in detail by various methods. Based on the results of each method, a sophisticated recipe has been elaborated, which provides clean, stoichiometric, and reconstructed surfaces, even if the sample was exposed to air prior to preparation. Moreover, the recipe works equally well for intentionally oxidized surfaces. The individual advantages of *ex situ* wet-chemical etching and *in situ* ion-milling and tempering can be combined in an unique way.

In regard to the post-growth annealing in order to optimize the electronic and magnetic properties of (Ga,Mn)As, the effect of surface segregation of interstitial Mn was quantified. It turns out that the Mn concentration at the surface increases by a factor 4.3 after annealing at 190°C for 150 h.

The removal of the segregated and oxidized species by wet-chemical etching allows a tentative estimate of the content of interstitial Mn. $19-23\,\%$ of the overall Mn content in as-grown samples resides on interstitial positions.

The complementary results of core level photoemission spectroscopy and resonant photoemission spectroscopy give hints to the fact that a sizeable valence hybridization of Mn is present in (Ga,Mn)As. This outlines that the simple Mn $3d^5$-configuration is too naive to reflect the true electronic structure of substitutional Mn in (Ga,Mn)As. Great similarities in the core level spectra are found to MnAs. The bonding is thus dominantly of covalent, not ionic, character.

Transport measurements, in particular for very low temperatures ($\leq 10\,\mathrm{K}$), are in agreement with previous results. This shows that at low temperature, the conduction is mainly governed by variable-range hopping which is in line with the presence of an impurity band formed by substitutional Mn.

In the light of the presented results, it is therefore concluded that a double-exchange interaction is the dominant mechanism leading to ferromagnetic coupling in (Ga,Mn)As. The valence hybridization and the presents of an impurity band, both of which are inherent properties of substitutional Mn, are indications for a double-exchange scenario, being at variance to a RKKY-based explanation. Contributions from a RKKY-like mechanism cannot definitely be excluded, however, they are not dominant.

PACS numbers: 75.50.Pp, 82.80.Pv, 79.60.Bm, 81.65.Mq, 81.65.Cf, 61.72.Ji, 71.55.Eq, 61.72.Cc, 71.20.Nr, 66.30.Lw, 81.65.Rv, 68.35.Dv

Keywords: Ferromagnetic semiconductors, (Ga,Mn)As, photoemission spectroscopy, surface preparation

Zusammenfassung

Die vorliegende Arbeit befasst sich mit der Oberflächenbehandlung, der Materialoptimierung und der elektronischen Struktur des verdünnten magnetischen Halbleiters (Ga,Mn)As. Die beiden Hauptaspekte sind dabei die Präparation sauberer Oberflächen und die Identifikation einer möglichen Valenzhybridisierung in (Ga,Mn)As mithilfe von Photoemissionspektroskopie.

Mehrere Reinigungsmethoden wurden einzeln auf (Ga,Mn)As Oberflächen angewandt und deren Wirkung anhand mehrerer Untersuchungsmethoden verglichen. Basierend auf den Einzelergebnissen wurde eine spezielle Reinigungsprozedur ausgearbeitet, welche stöchiometrische, reine und wohldefinierte Oberflächen liefert, selbst wenn die Proben Umgebungsluft ausgesetzt wurde. Die beschriebene Vorgehensweise funktioniert des Weiteren auch bei absichtlich oxidierten Proben. Hierbei werden die individuellen Vorteile von *ex situ* nass-chemischen Ätzen, *in situ* Ionenstrahlätzen und Erhitzen auf besondere Art und Weise kombiniert.

Im Hinblick auf das Ausheilen nach dem Wachstum konnte die Oberflächensegregation von interstitiellem Mangan quantifiziert werden, wobei sich zeigte, dass die Mangankonzentration an der Oberfläche um einen Faktor 4.3 nach 150 Stunden Ausheilen an Luft zunahm.

Ein Vergleich zwischen ausgeheilten und anschließend geätzen Proben lässt eine vorsichtige Abschätzung des Anteils an interstitiellem Mangan in nicht ausheilten Proben zu. Hierbei zeigt sich, dass sich $19 - 23\,\%$ das Gesamtgehalts an Mangan auf interstitiellen Gitterplätzen befindet.

Komplementäre Untersuchungen mit Photoemissionsmethoden an Rumpfniveaus und mithilfe resonanter Photoemission geben Hinweis darauf, dass für Mangan in (Ga,Mn)As eine Valenzhybridisierung vorliegt. Dies führt zu dem Schluss, dass die simple Annahme eines zweifach positiv geladenen Mn-Atoms in $3d^5$-Konfiguration zu pauschal ist, um die tatsächliche elektronische Struktur von substitutionellem Mn in (Ga,Mn)As widerzuspiegeln. Die Spektren zeigen eine große Ähnlichkeit zu Manganarsenid, was beweißt, dass die Bindung vorherrschend kovalenter und nicht ionischer Natur ist.

Darüber hinaus sind ebenfalls durchgeführte Transportmessungen im Einklang mit bereits veröffentlichten Ergebnissen aus der Literatur. Dabei zeigt sich, dass der Ladungstransport, vor allem bei tiefen Temperaturen unterhalb von 10 K, durch variable-range hopping statt findet. Dieses Verhalten steht im Einklang mit dem Vorhandensein eines Stoŕstellenbandes, welches von substitutionellem Mn gebildet wird.

Angesichts der hier gezeigten Daten kann gefolgert werden, dass ein Doppelaustausch der ausschlaggebende Mechanismus für das Auftreten ferromagnetischer Kopplung in (Ga,Mn)As ist. Sowohl die Valenzhybridisierung substitutionellem Mn als auch die Ausbildung eines Störstellenbandes durch selbiges, deuten auf einen Doppelaustausch in, was im Gegensatz zu einer RKKY-basierten Erklärung steht. Hierbei kann ein gewisse Bedeutung des RKKY-Modells nicht vollständig ausgeschlossen werden, jedoch ist diese definitiv nicht dominant.

1 Introduction

In 2008, the International Technology Roadmap for Semiconductors (ITRS) increased its prognosis for the slated gate length in 2022 from 4.5 nm in the 2007 report[1] to 8.1 nm. This fact shows that even industry already considers the expected difficulties of a further decrease of the integrated circuit size. For the last four decades the semiconductor industry was able to fulfill Moore's prophecy.[2] However, the call for new materials gets louder every year.

In order to circumvent the problems faced in the course of further miniaturization and increasing energy consumption, ferromagnetic semiconductors (FS) or diluted magnetic semiconductors (DMS) are among the most promising candidates in the context of spintronics. The term spintronics summarizes all effects harnessing the spin of the carriers in addition to their charge. The resulting possibilities of manipulating both spin and charge of the carriers in semiconductors by external stimuli, would result in new device functionality and logical architecture.[3] A seamless integration of a ferromagnet into a semiconductor would offer the possibility of injection, storage, and manipulation of spins in a single solid-state device, leading to, e.g., nonvolatile memories and components for quantum computation. However, such an integration of ferromagnetism into a semiconductor device is usually unsuccessful, since the large resistance mismatch of metallic contacts and the semiconductor leads to a Schottky-barrier. This barrier results in an increased spin scattering at the interface. The generation of long-range ferromagnetic ordering in the semiconductor itself, as done in DMS, solves this problem.

Among the great family of DMS, (Ga,Mn)As, or sometimes referred to as $\mathrm{Ga}_{1-x}\mathrm{Mn}_x\mathrm{As}$, has attracted the most interest and is thus currently the most studied ferromagnetic semiconductor. (Ga,Mn)As is a supersaturated solid solution of Mn (with x in the percentage region) in a GaAs matrix, where the cation is heterovalently substituted by Mn ions. The Mn thereby takes a double role in providing free charge carriers (in this case holes) and a local magnetic moment.

The paradigmatic role of (Ga,Mn)As within the vast field of DMS is mainly caused by three reasons. First of all, it adds ferromagnetism to the mature GaAs/(Al,Ga)As-system which, in the last few years, has been the benchmark for interesting physics in high-speed electronic and optoelectronic devices, and offers long spin lifetime and spin coherence. Secondly, since magnetism and carriers are strongly interlinked in (Ga,Mn)As, the magnetic state in DMS can easily be manipulated by varying the carrier density using light, co-doping, electric field and lattice strain. Thirdly, and most important for future applications, (Ga,Mn)As shows the highest ordering temperature of all DMS, with a current record of 183 K.[4]

Even though it has long been hailed as a possible room-temperature DMS and first proof-of-concept spintronic devices have successfully been fabricated,[5] (Ga,Mn)As has yet to gain in Curie temperature in order to achieve technological significance. The Curie-temperature T_c has steadily been increased since its first synthesis in 1996,[6] from initially 60 K, however, it is still far below room temperature. It is therefore essential to gain a detailed understanding of the fundamental magnetic properties of (Ga,Mn)As and the underlying mechanisms. Only then, the ultimate aim of a room-temperature DMS can be achieved. This ambitious goal has not been reached, despite intense research over the last 14 years.

More crucial, a theoretical understanding of the ferromagnetism in (Ga,Mn)As is still elusive. It is generally agreed upon the hole-mediated origin, however, the detailed mechanism is unclear. The central open question is if the carriers reside in the valence band (VB) of the host or if they form a narrow impurity band (IB) in the band gap. This characteristic of the carriers determines, if the interaction is of Rudermann-Kittel-Katsuya-Yoshida (VB) or of double-exchange (IB) type. Evidences for both mechanisms have been claimed, making a consensus impossible.

In addition, the interest in (Ga,Mn)As turned more and more away from the applicational point of view to another facet of this fascinating material in recent years. (Ga,Mn)As has become a model system for the investigation of ferromagnetism in a highly frustrated and disordered alloy. This is an old and important problem of solid state physics and led to even more attention to (Ga,Mn)As, in particular, from the fundamental point of view. The random distribution of the substitutional Mn and a large amount of compensation defects, caused by the non-equilibrium growth conditions, results in a fail of any mean-field approximations.

The incomplete picture of the mechanisms driving magnetic ordering in (Ga,Mn)As outlines the need for further theoretical and experimental investigations. In order to gain deeper insight into the rich physics of (Ga,Mn)As, this thesis is intended to provide further valuable data, especially on the electronic structure of (Ga,Mn)As. The findings help to concretize the understanding of the ferromagnetic coupling and the electronic structure. It is organized as follows. Chapter 2 gives the most important properties of the host matrix GaAs and a summary of the present level of knowledge on (Ga,Mn)As. In chapter 3, various aspects of photoemission spectroscopy (PES) are explained. Special interest is focused on angular dependent measurements and depth profiling. The possibility of post-growth surface preparation and its effects on the electronic structure is explored in chapter 4. Using an elaborated surface preparation information on the electronic structure is obtained by core level PES and resonant PES as discussed in chapter 5. Complementary temperature dependent transport measurements are presented in chapter 6. The results are summarized and an outlook is given in chapter 7.

2 Diluted magnetic semiconductors

2.1 Gallium Arsenide

As most of the properties of (Ga,Mn)As, except the transport and magnetic ones, are determined by the host material GaAs (due to the low concentration of Mn) the basic features of GaAs shall be reviewed prior to introducing (Ga,Mn)As. Particular interest is focused on the behavior of GaAs under exposure to air and consecutive *ex situ* and *in situ* surface treatment, since clean and ordered surfaces are a prerequisite for photoemission spectroscopy.

2.1.1 Physical properties of GaAs relevant for spintronic applications

Gallium arsenide (GaAs), firstly synthesized in 1929,[7] is a heterogeneous semiconductor with a direct band gap of 1.42 eV at room temperature. It is built up of two face-centered cubic sublattices of Ga and As, shifted by $\left[\frac{1}{4}\frac{1}{4}\frac{1}{4}\right]$ with respect to each other along the body diagonal, forming a zinc blende lattice (space group $F\bar{4}3m$) [*cf.* Fig. 2.1 (a)]. This structure (sphalerite) is the most common natural structure of GaAs, however, GaAs can also rarely crystallize in the hexagonal wurtzite structure (space group $P6_3mc$).

Being a heterogeneous III-V compound has some interesting consequences. The metalloid gallium and the non-metal arsenic have electronegativities (Pauling notation) of 1.81 and 2.18, respectively. This results in a sizeable ionicity of the bonding with a fraction of $i = 0.31$.[8] As a consequence, all crystallographic planes including both elements (e.g., $\{111\}$) are polar. This becomes important for the adsorption of adatoms or the behavior under chemical treatment (*cf.* Sec. 2.1.4).

In view of the fact that photoemission spectra make up the largest part of the upcoming results, two spectroscopic consequences of the ionicity of the bonding should be noted. The missing bonding partners at the surface lead to shifts in the binding energies for both elements. In the case of Ga the binding energy shifts to larger values whereas for As the shift is to smaller binding energies.[10,11] For elemental Ga or As on GaAs, which may result from sample preparation methods, the opposite tendency is observed. The gallium, in the absence of the electron affine As, shifts to lower binding energies whereas As exhibits higher binding energies.[12] Both shifts are an exclusive consequence of the ionicity of the Ga-As bonding.

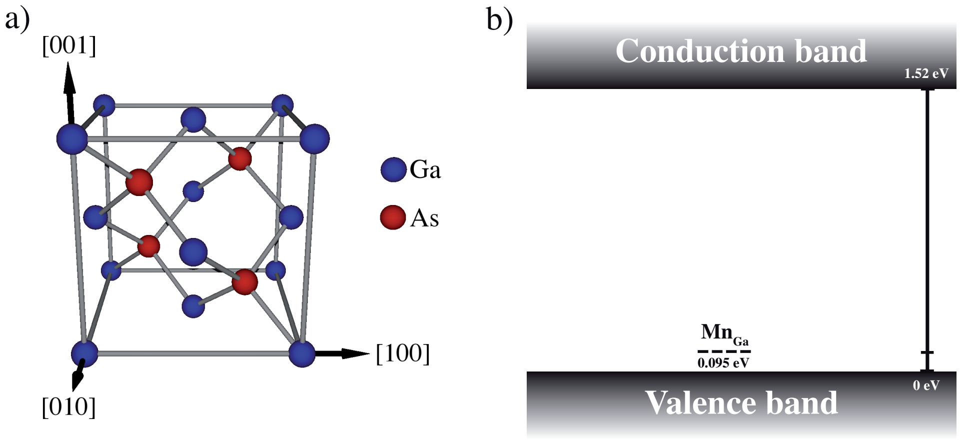

Figure 2.1: *Panel (a): Sphalerite (zinc blende) crystal structure of GaAs. The lattice consists of two fcc sublattices of Ga (blue) and As (red) shifted by* $\left[\frac{1}{4}\frac{1}{4}\frac{1}{4}\right]$ *with respect to each other along the body diagonal. Panel (b): Band diagram of GaAs. The band gap at* $T = 0\,K$ *is* $1.52\,eV$ *and* $1.42\,eV$ *at* $T = 300\,K$*. Manganese as an isolated impurity on Ga-sites acts as acceptor with an ionization energy of* $0.095\,eV$*.*[9]

From the applicational point of view GaAs is the second most widely used semiconductor in nowadays communication industry. The advantageous properties of GaAs are:

- direct band gap (Si: indirect) (*cf.* Fig. 2.2)
- high electron mobilities
- tuneable (direct) band gap between 1.42 eV to 1.92 eV (at 300 K) by co-alloying with Al ($\leq 37\,\%$)

However, GaAs has the following drawbacks compared to Si:

- both elements are rare in comparison to Si
- As is outmost toxic
- the hole mobility is lower

Therefore, GaAs is currently not able to provide the same circuit density as Si. GaAs is mostly used in niche applications, e.g., high efficiency solar cells, high frequency devices and near-infrared diodes. Concerning the magnetic properties, GaAs is a diamagnet with a susceptibility of $\chi \approx -1.3 \times 10^{-6}$ (at 100 K).[13]

The triumphant advance of semiconducting materials in the second half of the 20th century is principally based on only one fact. Their conductivity can easily be adjusted both during the growth via co-doping of impurities and even during the device operation by applying external fields. Electron or hole conductivity can readily be chosen by the proper choice of dopant. One particular dopant, manganese, shall be addressed in more detail.

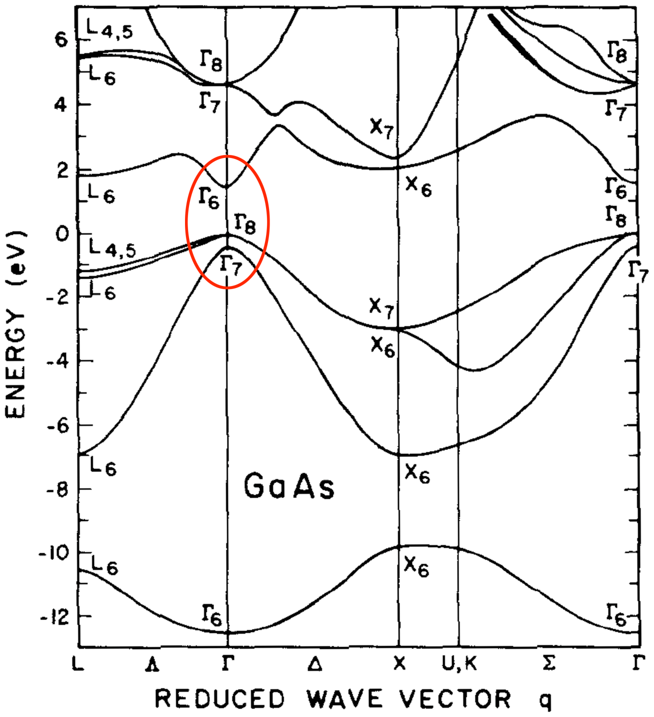

Figure 2.2: *Band structure of pure GaAs. The direct band gap at the* Γ*-point as well as the four-fold degenerated hole bands at* Γ_8 *with the split-off band at* Γ_7 *are indicated. Taken from Ref. 8.*

The transition metal (TM) manganese with its open d-shell is a well known element in the physics of highly correlated systems. Mn compounds show phenomena such as colossal magnetoresistance (manganites) or strong antiferromagnetic ordering. So, Mn compounds are already very interesting for future computation devices, in particular for data storage.

Mn as a dopant substitutes a Ga atom in the lattice. Due to its electron configuration [Ar] $4s^2 3d^5$ on the site of the trivalent Ga, a $3d^4$-configuration is expected at $T = 0\,\mathrm{K}$. However, with an ionization energy between $0.095\,\mathrm{eV}$[9] [see Fig. 2.1 (b)] and $0.113\,\mathrm{eV}$[14,15] Mn provides a loosely bound hole in the valence band with a binding energy of $E_{bin} \approx 4\,\mathrm{meV}$[16] and a Bohr-radius of $\approx 1\,\mathrm{nm}$. Hence, the Mn impurity is left back in the d^5-configuration (high-spin, $S = \frac{5}{2}$).[17]

Due to the high mobility of TMs in GaAs under equilibrium growth conditions, the TM is not easily built into the lattice, resulting in a limited solubility of Mn in GaAs (in the order of $10^{18}\,\mathrm{cm}^{-3}$).[18] Thus, the Mn impurities are separated far enough from each other to show no correlated behavior. However, when the doping concentration can significantly be increased, the semiconductor starts to become degenerated.

By definition,[9] a semiconductor is regarded as being degenerated if the carrier concentration, in particular by doping, is so high that its transport properties tend to be more metal- than semiconductor-like. For instance, the resistivity decreases by decreasing temperature. The carrier concentration by doping is then larger than the effective density-of-states (DOS) in the conduction (for n-doping) or in the valence band (for p-doping), respectively. The usual approximation that the Fermi energy of the semiconductor is at least $3k_BT$ separated from the valence or conduction band edge is no longer fulfilled. The wave functions of the dopants overlap and an impurity band is formed which increases in width with increasing doping. The impurity band starts to overlap with the bands of the host and, in the extreme, the Fermi energy is shifted into the host-bands.[19] Thus, the conduction takes place mainly in the impurity band and the semiconducting behavior is lost. At low temperatures the conductivity is limited by the hopping probability from one to another impurity scaling in analogy to a Mott-Insulator[20] with $\exp(1/T^4)$. Mott also formulated a criterion for the degeneracy of a semiconductor. The critical dopant concentration x_c is thus given by:[20]

$$x_c = \frac{0.25^3}{4}\left(\frac{a_0}{a_B}\right)^3 \tag{2.1}$$

with the lattice constant of GaAs a_0 and the effective Bohr's radius of Mn in GaAs a_B. With the aforementioned values this gives a boundary for degeneracy of $x_c \geq 0.0007$. In consequence, GaAs with a Mn doping in the percentage range can surely be called degenerated.

Under normal circumstances such heavy doping (commonly denoted as n^{++} or p^{++}) is avoided. However, for contacting MOSFET it is being used since the Schottky-barrier is not as high as for a metal-semiconductor interface and the device architecture is more monolithic.[9] For GaAs, the density-of-states (DOS) at 300 K is listed in Tab. 2.1.

Table 2.1: *Density-of-states (DOS) in units of cm^{-3} for the valence and conduction band of GaAs at $T = 300$ K; for comparison also the extrinsic carrier concentration for uncompensated and compensated (only 15 % of the dopants are active) of $Ga_{0.95}Mn_{0.05}As$ is given.*

N_c	4.7×10^{17a}
N_v	7.0×10^{18a}
n_p $Ga_{0.95}Mn_{0.05}As$ (uncompensated)	5.56×10^{20}
n_p $Ga_{0.95}Mn_{0.05}As$ (85 % compensated)	8.34×10^{19}

^{a}: from Ref. 9

The DOS of the valence band is by one order of magnitude larger than the DOS of the conduction band due to the coincidence of the heavy-hole and light-hole band. In view of (Ga,Mn)As also the carrier concentrations for a (Ga,Mn)As sample with a Mn concentration of 5 % is given in Tab. 2.1. The extrinsic carrier concentration is here two orders of magnitude larger than the maximal DOS in the valence band. Even for a highly compensated sample, i.e., only one out of seven Mn impurities is active (a reasonable value for as-grown samples widely reported in the literature),[21,22] the carrier concentration is still one order of magnitude larger than the DOS of the host. This back of an envelope calculation already visualizes that (Ga,Mn)As has to be expected being a degenerated semiconductor in accordance with its transport behavior.[23]

2.1.2 Natural oxide layer on GaAs

At the interface from the bulk to the vacuum bonding partners for the constituents are absent which results in unsaturated bonds. For semiconductors the bonding orbitals are s- or p-like-orbitals (sp^3 hybridized) and are referred to as *dangling bonds* sticking out of the surface. Those bonds are highly reactive and lead to the consequence that contaminations such as oxygen are not only weakly physisorbed (by van-der-Waals forces) but chemisorbed (covalently-chemically bound) at the surface. This oxidation is an exothermal process and therefore occurs as soon as the sample leaves the vacuum in the growth chamber. So-called room-temperature-oxidized (RTO) samples—in contrast to intentionally oxidized samples—are the starting point for any measurement after the growth and thus, the oxide layer with all its characteristics is of high interest.

In contrast to a homogeneous semiconductor such as Si or Ge, the situation with two elements in GaAs complicates the oxidation. Ga_2O_3 in the bulk has a considerably higher (240 kcal/mol) heat of formation than As_2O_3 (158 kcal/mol).[24] Thus, the oxidation does not proceed equally for Ga and As. All stages of the oxidation are illustrated in the phase diagram shown in Fig. 2.3.

Starting from the stoichiometric GaAs the Ga is preferentially oxidized and elemental arsenic is left behind. Under further exposition to oxygen also the arsenic is oxidized. Only when these compounds are saturated the formation of higher oxidation states such as $GaAsO_4$ and As_2O_5 begins. The consequence, especially of stage 1, is that the oxide layer looses the stoichiometry of the bulk. The preferential oxidation of Ga leads to a gallium-rich oxide layer with a pile-up of elemental arsenic at the GaAs-oxide interface. This has been shown in the literature qualitatively,[25] however, a quantitative estimation of the composition gradient has not been analyzed and will be addressed later. The overall oxide layer thickness of epi-ready GaAs is in the range of $2-3\,\mathrm{nm}$ with a roughness not exceeding 0.3 nm.[26]

In this context, a beneficial characteristic of low-temperature grown GaAs (LT-GaAs) has to be pointed out. The huge amount of impurities (especially As-antisites, As built in on a Ga-site) has two consequences. First of all, the Fermi level is pinned in the impurity states. Secondly, the lifetime of the *minority* charge carriers (holes for n-doping As-antisites) is dramatically reduced. Both processes tend to make the surface less reactive and both chemisorption and physisorption occur on a longer time scale.[27]

This suggests that short (a few seconds), unavoidable exposures to air during the sample preparation or rest-amounts of argon and nitrogen have minor influences on the surface quality. It is not clear yet, if this situation is transferable to (Ga,Mn)As, where the *majority* charge carriers are holes. However, the upcoming results indicate that the surface reactivity is low enough to allow the acquisition of reproducible results, even after a short exposure to air.

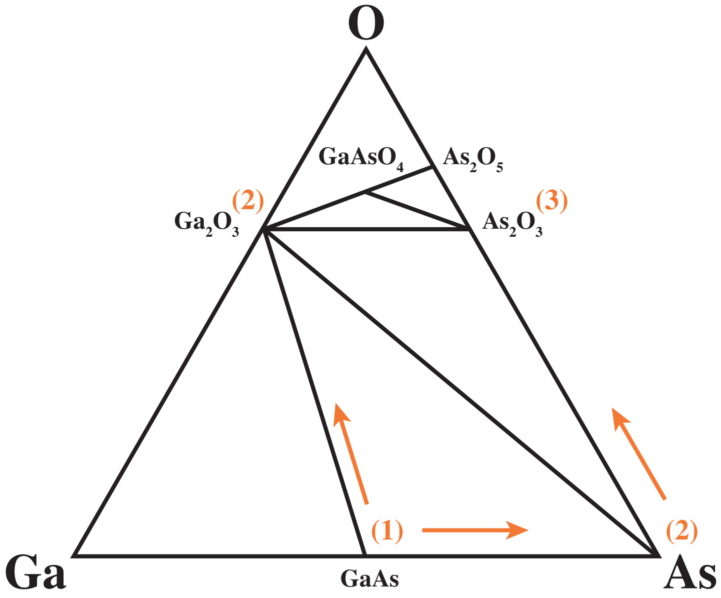

Figure 2.3: *Ternary Ga-As-O equilibrium phase diagram; Oxidation of pure GaAs (stage 1) leads firstly to a formation of* Ga_2O_3 *and elemental arsenic (stage 2). On further oxidation also the As is oxidized to* As_2O_3*. Higher oxides (*$GaAsO_4$ *and* As_2O_5*) are formed by the products of the primary oxidation process. According to Ref. 28.*

2.1.3 Thermal desorption of oxides

The thermally induced evaporation of species is a common technique in ultrahigh-vacuum (UHV) technology. In particular for the desorption of adsorbates from the sample it has been used ever since experiments were performed under UHV conditions. The process is based on the fact that contaminations are thermally activated and blown off the surface. Especially for metals and semiconductors, where it is one of the most common procedures, it works astonishing well,as the surface is well ordered after the heating.

Again, for a heterogeneous compound such as GaAs the situation is much more complicated. The desorption rate is naturally very sensitive to the temperature. However, the evaporated compound is also crucially determined by the temperature. The process is very complex and depends on various variables such as heating rate, additional

Ga or As flux, and so forth. Details can be found in the literature.[29–31] In few words the processes can be imagined as follows: below 400°C the most volatile As-oxides are sublimated or reduced. This has the consequence that tempering can in fact lead to an increase of the oxide layer thickness. Between $400 - 500$°C elemental As (as dimer or tetramer) and galliumsuboxide (Ga_2O) start to evaporate. Above 500°C the gallium trioxide is vaporized via a reduction to galliumsuboxide. Beginning from 600°C GaAs dissociates. The basic chemical reaction can be found in Tab. 2.2. The fact that a reduction of both elements occurs prior to the evaporation results in the fact that tempering GaAs below its dissociation temperature leads to so-called pit formation. The oxygen freed by the reduction corrodes the material and leads to a further loss of material. This process starts at already thinner parts of the oxide layer leading to localized corrosion.

Table 2.2: *Set of basic chemical reaction taking place during tempering of GaAs and its oxide layer; the reductive character of all the reactions (except the last one) leads to an enhanced corrosion of the material and pit formation is the consequence.*

$$\begin{array}{lcll}
6GaAsO_4 & \xrightarrow{\leq 400^\circ C} & 3As_2O_3 + 3Ga_2O_3 + 3O_2 & \mathrm{I} \\
3As_2O_5 & \xrightarrow{\leq 400^\circ C} & 3As_2O_3 + 3O_2 & \mathrm{II} \\
4GaAs + 3O_2 & \xrightarrow{\leq 400^\circ C} & 2Ga_2O_3 + 2As_2\ (As_4) \uparrow & \mathrm{III} \\
As_2O_3 + 2GaAs & \xrightarrow{\leq 400^\circ C} & Ga_2O_3 + 2As_2\ (As_4) \uparrow & \mathrm{IV} \\
Ga_2O_3 + 4Ga & \xrightarrow{\geq 500^\circ C} & 3Ga_2O \uparrow & \mathrm{V} \\
4GaAs & \xrightarrow{\geq 600^\circ C} & 4Ga + 2As_2\ (As_4) \uparrow & \mathrm{VI}
\end{array}$$

Nevertheless, cleaning of GaAs by heating is the most common technique to remove the native oxide layer. In order to circumvent the complex chemistry taking place below the actual dissociation temperature, GaAs is usually heated to well above 600°C in the MBE chamber. After that the substrate is covered by a clean buffer layer. However, as will be discussed later, such temperature cannot be used for (Ga,Mn)As. If thermal activation of the surface is required, temperatures below 250°C have to be maintained, in order to preserve the thin film character and suppress Mn out-diffusion. On the other hand, tempering is necessary after damage to the surface has been made, e.g., by sputtering or in order to get rid of volatile contaminations such as water.

2.1.4 Wet-chemical etching of GaAs

As a result of the extensive use of wet-chemical etching in device production, a phenomenological understanding of the different etching processes is needed. Wet-chemical etching is a widely used technique in nowadays semiconductor industry, for instance in forming a mesa isolating device, recess etching prior to gate metallization, and vertical pattering.[32] Unlike elemental semiconductors, e.g., Si or Ge, the heterogeneity of GaAs and also the polarity of certain crystallographic planes has to be considered. Except for the {110} planes, all directions are of polar nature.

Wet-chemical etching of semiconductors is basically a reaction of oxidation-reduction type. Therefore, an etchant for GaAs usually consists of three agents. One oxidation agent such as H_2O_2, a complexing agent like HCl, HF, or H_2SO_4 and a dilutant, mostly deionized water (DIW, $\rho \approx 1\,\mathrm{M\Omega cm}$). The oxidation agent oxidizes the surface atoms which are mainly insoluble in water. However, the complexing agent hybridizes the oxides forming water-soluble complexes which are subsequently washed away. The effectivity of the etching process is a complex interplay of all three ingredients which makes the situation far from simple. Highest etch-rates (nm s) require an optimal ratio. One of the most effective is H_2SO_4:H_2O_2:H_2O, in a mixing ratio of 1:8:1. An etch-rate of 130 nm s is obtained here.

Table 2.3: *Tabular comparison of the characteristics of reaction-rate limited and diffusion-limited etching relevant for the upcoming sections.*

reaction-rate limited	diffusion-limited
strong temperature dependence	temperature independent
preferential etching of ⟨111⟩As	nearly isotropic etching rates
etching rate linear with time	etching rate saturates $\propto t^{1/2}$
doping dependent	marginal doping dependence
largely maintains surface topography	smoothes surface
no significant change by agitation	increasing etch-rates by stirring

If the concentration of the oxidation agent is too high, the complexing agent cannot maintain a sufficiently fast removal of the oxides. The process is limited by the chemical activity of the surface and is hence titled reaction-rate limited. If the concentration of the oxidizer is too low or the etchant is comparably viscous, the diffusion of the oxidizer is the limiting factor. The reaction is then diffusion-limited. The main feature of both limits (disregarding the absolute etch-rate which is additionally affected by the concentration of the dilutant) are given in Tab. 2.3. In view of the upcoming experiments they shall be discussed here.

The first point of T-dependence is of less importance since the chemical etching was always performed at room temperature. Secondly, preferential etching has to be avoided as microstructures induced by the etching along certain crystallographic directions are unfavorable for a flat surface. Thirdly, the etching rate depends naturally on the duration of the etching process. In order to avoid a saturation of the etching process the etching was performed under flowing acid. Furthermore, the basic reaction is of oxidation-reduction type, which is a charge-transfer between the reactants. Therefore, a dependence on the charge balance of the semiconductor, i.e., carrier concentration, is obvious. This connection between doping and etching behavior is crucial. Since experiments on samples with different Mn concentration (and As antisites) will be performed a dependence on the amount of impurities is undesirable. Closely related to the second point is the fact that diffusion-limited reactions tend to smooth the surface out whereas reaction-rate limited processes tend to conserve or even enhance pits and hillocks. A strong crystallographic dependence of the etching rate of reaction-rate limited processes tends to enhance structure present on the surface prior to the chemical process. Hence, surface structures become more pronounced. In contrast to this, diffusion-limited processes tend to attack surface structures preferentially and result in a smoothed surface. Finally, if the reaction is just limited by the speed of the reaction it is apparent that stirring should not affect the process efficiency. If the supply, for instance of the oxidation agent, is the limiting factor an agitation (stirring or supersonic bath) of the etchants increases the etch-rate significantly. However, the composition of the etchant, especially the concentration of the dilutant, is far more critical.

Another point is the previously mentioned etch-rate. As the main goal of this work is the cleaning of thin films ($\approx 50\,\mathrm{nm}$) high etch-rates are not required, in fact undesired. Altogether, preparation of GaAs with a diffusion-limited etchant appears to be the best choice. In this context, also etching with pure acids (hydrochloric, hydrofluoric, and sulphuric) has to be considered as diffusion-limited since the possible oxidizer, for instance solved oxygen in the acid, has to reach the denuded surface in order to lead to further reactions on the same. However, etching rates can be minimized by this method, which is required due to the thin film character of the investigated samples. Therefore, the etching of the films was performed with highly concentrated acids so that only the natural oxide of the GaAs is removed. However, the advantage of smoothing the surface, non-preferential etching, doping independence, and low etch-rates comes at the price of remaining contaminations.

A large scale removal of the first μm ensures also the dissolution of other contamination such as carbon compounds. Those compounds are hardly affected by the etching itself but are literally taken away by the eroded substrate. Secondly, not diluting the acid with additional water enhances the probability for the remaining anions of the acid (Cl^-, F^-, or SO_4^{2-}) to be chemisorbed on the exposed, clean surface. This effect can be minimized by a subsequent flow with DIW. There is no consensus on the second point in the literature. Massies *et al.*[33] do not see a re-oxidation of the clean surface by rinse with DIW but blame the sample handling in air for the observed oxide peaks in the spectra. In contrast to this, they showed that a steady storage of the sample in DIW subsequent to the etching leads to a tremendous oxidation of the surface. Similar results are shown by Liu *et al.*[12] In contrast to that, Song and co-workers[34] observe an increasing oxide signal after subsequent rinse by water. However, they do point out the necessity of a water treatment since the etching leaves back a considerable amount of anions on the clean surface. Based on this, a rinse with DIW was taken as the method of choice.

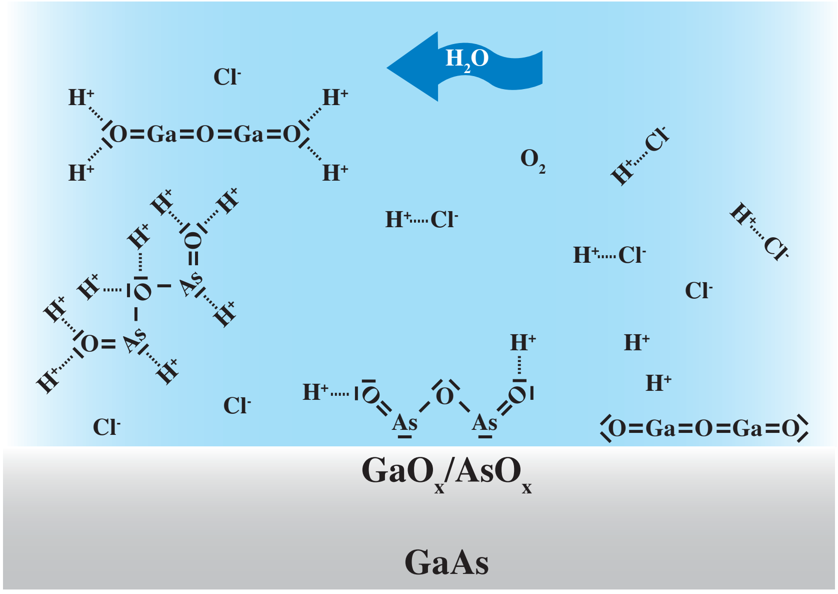

Figure 2.4: *Sketch of the wet-chemical etching of GaAs with pure HCl; the natural oxides of Ga (mainly Ga_2O_3, insoluble in water) and of As (As_2O_3, hardly soluble in water) form a hydrogen bridge with the H^+ ions of the rocksalt acid at the free electron pairs. This complexation leads to soluble compounds which are washed away by the flowing solution. The Cl^- anions left behind may either stuck on the surface or are also washed away. Although the water is deionized it is likely to be oxygen-saturated leaving some O_2 molecules which can act as (weak) oxidation agents.*

A point not mentioned up to now is the fact that all etchants of the characteristic composition acid-oxidizer-water leave a thin residual oxide layer behind which needs further treatment. This is due to the fact that the oxidation is the primary process which is followed by the complexation. When the reaction is stopped the last grown oxides remain unsolved.

The necessity to avoid this remaining oxide layer further outlines the use of highly concentrated acid and a subsequent rinse with water *without* an oxidation agent. So, only the natural oxide layer is solved via complexation. In order to illustrate the processes taking place, Fig. 2.4 shows a sketch of the wet-chemical etching.

The loosely bound oxides of As and Ga (only the sesquioxides are shown whereas the higher oxides can safely be expected to show an analogous behavior) form a hydrogen bridge with their free electron pairs of oxygen and arsenic, respectively, and the proton of the acid. The so formed complexes are now highly soluble in water and washed away by the rinse flow. Thus, the rinse with the acid ensures on the one hand the washing away of complexes and on the other hand the steady supply of protons. The remaining anions (in this case, the chloride) may stuck to the surface as seen in Ref. 34. The consecutive rinse with DIW (not shown) deals with the obviously physisorbed anions and leaves an oxide and anion free surface. However, possible carbon contaminations are hardly affected. A protolysis or reaction with the anions seems to be unfavorable.

The water is deionized, thus, contaminations from the water should be negligible. However, the water contains surely molecular oxygen. This can be an advantage since it may act as a weak oxidizing agent further supporting the cleaning processes.

Finally, a benefit of wet-chemical etching shall be outlined. Since the volume compound GaAs is almost inert to wet-chemical etching, the protolysis is obviously unfavorable, no selective etching occurs. Selective etching is defined as the significantly faster removal of one compound. In contrast to preferential etching (along certain crystallographic directions), which can be a pronounced effect in GaAs, one does not have to worry about selective etching when using wet-chemistry.

2.1.5 Dry etching (ion beam etching)

In contrast to Sec. 2.1.4 all processes not including liquids are referred to as dry-etching. Besides methods such as plasma induced etching the focus here is on ion beam etching, subsequently named sputtering. The technical aspects of sputtering are addressed later. Here, the behavior of GaAs upon sputtering shall be shortly described.

Basically, the technique consists of the bombardment of a substrate with accelerated particles. The collision of the sputter gas and the target causes surface atoms to be removed from the surface. This is the great advantage, in particular for the cleaning of surfaces, since ion beam etching is more or less elemental insensitive. The sputter-rates differ from element to element significantly but in general all elements are sputtered away. This is in sharp contrast to wet-chemical etching which, for instance, does not affect the carbon on GaAs.[12]

Within ion beam etching there can be made another classification. Depending on the chemistry of the used gas one distinguishes between ion milling (positively charge ions of an inert gas such as Ar^+) or reactive beam etching (using, e.g., CF_4 or CCl_4). In the former case the effectivity of etching depends only on the impact of the gas atom whereas in the latter case the projectile atoms react chemically with the substrate and form gaseous products.

Chen and co-workers[35] showed for GaAs that reactive ion beam etching yields smoother surfaces whereas ion milling provides a higher etching rate, a linear dependence of the etch-rate on the ion current density (A/cm^2), and a carbon-free surface. From their data a sputtering rate for GaAs under the conditions used later in this thesis can be extrapolated. At an energy of 500 eV they give an etching rate per unit current density $[(\text{Å}/\text{min})/(\text{mA}/\text{cm}^2)]$ of 1170. Using the current density of $2.30\,\mu\text{A}/\text{cm}^2$ ($1.44 \times 10^{13}\,\text{cm}^{-2}\,\text{s}^{-1}$) calculated for the Omicron ISE10 Sputter Ion Source (ion current $23.4\,\mu$A at 600 eV, beam diameter 1.8 cm, angle to sample normal 45° or 54.7°) this would yield an etching rate of 16.15 nm/min. However, the author stated that the linearity of the etching rate on ion current density may not be valid for lower current densities. Due to the lower gas pressure (3×10^{-6} mbar compared to 1.7×10^{-4} mbar in Ref. 35) used later on, the current density is approximately two orders of magnitude smaller. Pearton *et al.*[36] give an etching rate of 6.0 nm/min for Ar^+ ions with a kinetic energy of 600 eV under an angle of 45°. This points out that the determination of the milled thickness is affected with a large error. Nevertheless, it is a good starting point as a rule of thumb.

Furthermore, the authors of Ref. 35 outline that the etching rate does not depend significantly on the beam energy within the range of $500 - 1200\,\mathrm{eV}$ (increase by 20 % by doubling the beam energy).[36] This point will also be addressed later.

Sputtering can lead to deterioration of the surface structure which can eventually lead to a complete destruction, i.e., an amorphous surface. Displacement damage can reach as deep as tenths of nm[36] into the material and thus, the sample needs further treatment such as tempering. The literature is, however, not consistent on the matter of amorphization.[37]

The mean value for the sputtering yield Y (Y=number of sputtered molecules per number of incident atoms) for GaAs with 600 eV Ar^+ ions (disregarding the crystallographic orientation) is approximately unity,[37] which is in remarkable agreement with the more recent results of Ohring and co-workers[38] (0.83 at 500 eV and 1.52 at 1000 eV). Furthermore, especially for compounds, the bombardment of the surface causes changes in the composition due to different individual sputtering coefficients of the constituting elements. This is accredited to the differences in surface binding energies of atoms.

Complementary to the model of preferential sputtering solely due to the difference in surface binding energies another, more elaborated mechanism was included in a more comprehensive model. Sputter-assisted surface diffusion of As has also been proposed as mechanism.[39] This Gibbsian segregation is capable of explaining the stoichiometric topmost layer of sputtered GaAs with an As-depleted region underneath. Stoichiometry is restored at the topmost layer by the replenishing of As by diffusion from the subsurface layer. The As-depleted region coincides with the penetration range of the sputtering ions.

Summing all up, the most important advantage of ion-milling is the fact that it is the only method, which reliably removes carbon related contaminations. Both tempering and wet-chemical etching remarkably reduce the carbon peak in the spectra but fail to push the signal below the detection limit. Hence, subsequent dry-etching is essential after tempering and wet-chemical etching.

2.2 Gallium Manganese Arsenide

2.2.1 Crystallographical and transport properties of (Ga,Mn)As

As mentioned above in Sec. 2.1.1 transition metals as dopants exhibit a very low solubility ($x \leq 10^{18}\,\mathrm{cm}^{-3}$) in GaAs when bulk samples are grown by standard procedures such as Czochralski or Bridgman-Stockbarger.[18] Thus, in order to reach Mn concentrations in the percentage range, which are required for the occurrence of ferromagnetism, special non-equilibrium growth conditions have to be met. The method of choice for producing (Ga,Mn)As thin films is low-temperature molecular-beam epitaxy (LT-MBE).[40,41] In conventional MBE, GaAs thin films are grown at substrate temperature somewhere in the range of 500 − 600°C on a GaAs bulk sample. By lowering the substrate temperature to around 240°C the co-evaporated Mn is not able to constantly remain at the surface of the substrate or form a second phase (MnAs),[42] but is directly incorporated into the lattice. A detailed description of LT-MBE and the elaborated procedure required to obtain high-quality (Ga,Mn)As thin films can be found in the literature.[40,41] All (Ga,Mn)As samples investigated in the course of this thesis have been grown by the Molenkamp group at the University of Würzburg.

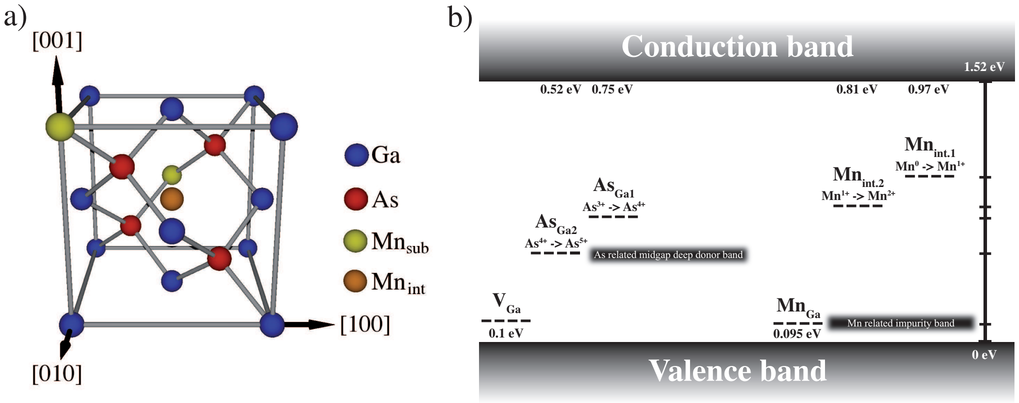

Figure 2.5: *Panel (a): Sphalerite (zinc blende) crystal structure of (Ga,Mn)As predetermined by the GaAs host. Substitutional Mn is indicated in yellow whereas the (As-terminated) interstitial Mn is highlighted in orange. Panel (b) Location of the doping levels; the band gap at* $T = 0\,K$ *is* $1.52\,eV$ *and* $1.42\,eV$ *at* $T = 300\,K$ ($E_{gap} = 1.23\,eV$ *at* $T = 300\,K$ *in the case of (Ga,Mn)As);*[43] *Manganese on Ga-sites acts as acceptor, whereas both As on Ga-sites and Mn on interstitial sites act as "deep" donors with two different levels. For GaAs it has been shown,*[44] *that both As-antisites together form an impurity band within the band gap* ($E = E_v + 0.5\,eV$)*, in contrast to (Ga,Mn)As were the impurity band is located at* $E = E_v + 0.7\,eV$*. Gallium vacancies* (V_{Ga}) *act as acceptor with an ionization energy of approximately* $0.1\,eV$*. The location of the Mn donor levels from DFT-calculations*[14] *has not been observed experimentally yet,*[22] *but is given for reasons of completeness as well as the expected location of the Mn-related impurity band. Values from Refs. 9,14,44,45.*

However, the increased Mn content comes at a price. The low temperature conditions result in a huge amount of defects already known from pure GaAs.[27] Most crucial among the resulting defects in pure GaAs are As-antisites (As$_{Ga}$). The low temperatures together with As-rich growth conditions in the MBE system (typical flux ratio: Ga:As$_4$ $\leq 1:4$)[40] lead to a considerable amount of these defects. As-rich growth conditions are needed to countervail the low sticking probability of As as a result of the high equilibrium vapor pressure of As.[46] As$_{Ga}$ acts as a two level deep double donor [see Fig. 2.5 (b)]. Those two levels form an As related electron impurity band in the middle of the band gap. In the light of the fact that Mn is an acceptor this becomes crucial since a part of the Mn-induced hole carriers will be compensated. Defect concentrations of As_{Ga} as high as $10^{19}\,cm^{-3}$ at a growth temperature of 200°C have been reported.[47] On the other hand, the As-rich conditions lead to a suppression of other possible defects such as Ga vacancies (V_{Ga}), Ga-antisites (Ga_{As}), or Mn on As-sites (Mn_{As}).[14] However, all these defects turn out not to be the major limiting factors for the extrinsic carrier concentration in (Ga,Mn)As.

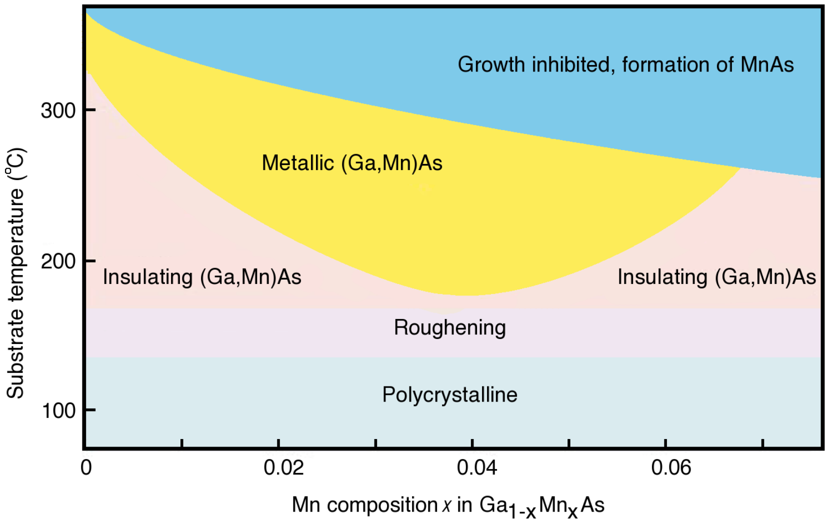

Figure 2.6: *Phasediagram of (Ga,Mn)As. The sample properties depend crucially on the substrate temperature during the growth and the Mn content. Homogeneous and metallic samples are desired. Adopted from Ref. 48.*

Mn is intended to be incorporated on a Ga site [yellow in Fig. 2.5 (a)]. However, a certain amount of Mn is also incorporated on interstitial sites, preferential on As-terminated sites [in the middle of an As tetrahedron, orange in Fig. 2.5 (a)]. This interstitial Mn (Mn_{int}) also acts as a double donor, since there is no space for its 4*s* electrons,[49] which then compensate the desired substitutional Mn (Mn_{sub}). The more electronegative environment favors an incorporation in an As-tetrahedron over that in a Ga-tetrahedron,[49,50] whereas other authors report the opposite.[51,52] Optical conductivity measurements have shown that in as-grown samples $70-80\,\%$ of the manganese atoms (of the nominal content) are compensated. The effects of growth temperature and Mn content are best visualized in the (Ga,Mn)As phase diagram in Fig. 2.6. Focussing on the effect of the Mn content under constant growth temperature it is observed that both lightly and highly doped samples are insulating. For low doping levels there are not enough charge carriers whereas for high doping levels compensation effects become dominant. This can also be seen in resistivity measurements on various doped (Ga,Mn)As samples in Fig. 2.7.[23]

Now, the justified question arises in how far this obvious compensation of induced charge carriers can be ascribed to interstitial Mn or if other effects are more important.

Transport, magnetometric, and x-ray diffraction (XRD) measurements on samples with various As-antisite defect concentrations with fixed Mn content ($x = 4,3\,\%$) have

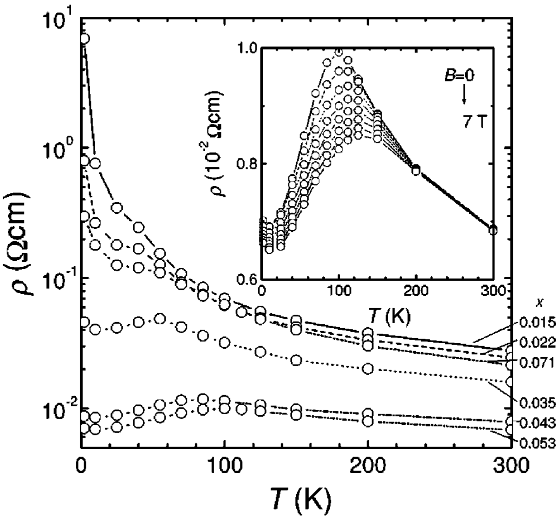

Figure 2.7: *Doping dependence of the resistivity ρ of as-grown (Ga,Mn)As. Both lightly and highly doped samples show semiconducting behavior (increase of the resistivity for lower temperatures). Only intermediate doping levels ($3.5 - 5.3\,\%$) show metallic behavior (decrease of the resistivity for lower temperatures). Taken from Ref. 23.*

shown that As_{Ga} defects have a huge impact on the sample properties.[53] For instance, well known from LT-MBE GaAs,[54] the lattice constant scales with the As_{Ga} concentration taking higher values for higher antisite concentrations.[53,55] Nevertheless, the lattice constant of (Ga,Mn)As follows quite remarkably Vegard's law:

$$a_{(Ga,Mn)As} = (1-x)a_{LT-MBE\ GaAs} + x a_{MnAs} \tag{2.2}$$

with $a_{(Ga,Mn)As} = 0.56572\,\mathrm{nm}$ and $a_{MnAs} = 0.6014\,\mathrm{nm}$.[56] Thus, Eq. (2.2) is used to determine the Mn concentration and the thickness of (Ga,Mn)As thin films.[55] The Mn concentrations and film thicknesses of all samples investigated in the course of this thesis have been determined by XRD measurements and with the aid of Eq. (2.2).

The results of Shimizu *et al.*[53] suggest that the growth of (Ga,Mn)As at comparable high temperatures (≈ 250°C) and low As_4/Ga-flux ratio results in the smallest As-antisite concentrations. This is in agreement with results known from the growth of LT-MBE pure GaAs.[47]

Nevertheless, there are overwhelming evidences that the major compensation effects are Mn_{int} and not As-antisites. Theoretical and experimental results have shown that As_{Ga} defects become relevant only for very low Mn concentrations ($x \leq 0.01$).[57] This becomes plausible by realizing that 1 % Mn corresponds to $10^{21}\,\mathrm{cm}^{-3}$, which is two orders of magnitude larger than typical As_{Ga} concentrations ($10^{19}\,\mathrm{cm}^{-3}$). The neglect of As_{Ga} in regard to the carrier compensation was also shown experimentally.[58] Additionally, Monte-Carlo simulations[59] as well as full potential linearized augmented plane wave (FPLAPW)[49] calculations suspect Mn_{int} being responsible for the compensation of holes in the entire doping range. Channeling Rutherford Backscattering (c-RBS) experiments on more highly doped samples have shown that interstitial Mn is the main cause of the sub-optimal transport properties, more precisely, the discrepancy between carrier concentration and the Mn content.[51] So, the insulating phase in the highly doped range is surely to be affected by Mn_{int} whereas for the limit of low doping other effects might become more important. It should be noted that Mn_{int} also has an effect on the lattice constant, i.e., a increases with higher Mn_{int} concentrations.[60] However, this effect is—even though the concentration of Mn defects is much higher than the concentration of As defects—small in comparison to the lattice expansion by As-antisites.

From the applicational point of view, the spin polarization of the charge carriers is of outmost interest since a possible application of a ferromagnetic semiconductor (FS) is the realization of a semiconducting spin injector or aligner providing a spin polarized current for computation processing. Theoretical calculations predict a very high spin polarization for (Ga,Mn)As of 100 %[61] (pure half metal) and 91.9 %, respectively.[62] Experimentally this value was not reached, nevertheless Braden and co-workers measured a spin polarization of 87 % at the Fermi level.[63]

2.2.2 The valence band – RKKY picture

Besides the structural properties (a high structural integrity leads to less scattering at the interface) and transport characteristics the question arises what causes long-range ferromagnetic order in (Ga,Mn)As. The origin of interaction is under debate since the first growth of Mn-doped GaAs, which showed ferromagnetism.[6] However, it was obvious very early that transport and magnetic properties are strongly interlinked.

Combined magnetometric and transport measurements on (Ga,Mn)As with various Mn concentrations are shown in Figure 2.8.[23] Higher conductivities directly result in higher Curie temperatures T_c, which is a strong evidence that magnetism and carrier concentration are strongly connected. A comparison of T_c and resistivity of various Mn concentrations x led to the derivation of the following semi-empirical formula for the Curie temperature in dependence of the concentration. This equation may seem rather bold, however, it was able to give the T_c, in particular for samples grown in the early stage of the interest in (Ga,Mn)As, astonishing well. Even today, with samples of improved crystalline quality available, this equation still works for a rough estimation and provides reasonable values for T_c:[48]

$$T_c = 2000 \cdot x \pm 10\,\mathrm{K} \tag{2.3}$$

Based on this apparent dependence a model was proposed. The correlation between carriers and ferromagnetism is particularly strong in rare earth $4f$-elements such as neodymium or gadolinium. Here, the interaction between the localized $4f$-electrons with their large magnetic moment is mediated by the itinerant conduction electrons. This is theoretically explained in the framework of the so-called Ruderman-Kittel-Kasuya-

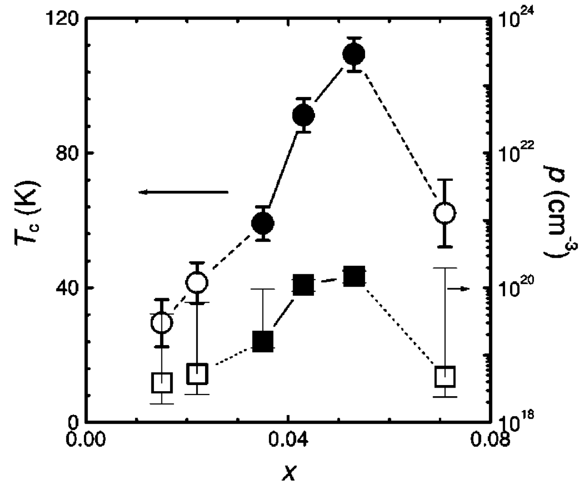

Figure 2.8: *Relation between Curie temperature T_c and carrier concentration p in as-grown (Ga,Mn)As; a higher conductivity is correlated with a higher Curie temperature T_c and vice versa. This is a clear evidence that the magnetic interaction is directly linked to the carrier concentration. For details see Ref. 23.*

Yosida (RKKY)[64] interaction. Roughly speaking, it states that localized magnetic moments at the lattice site lead to an antiferromagnetic polarization of the carriers. In the next step, those itinerant carriers can couple with the next atom leading to an effective magnetic coupling between the atoms even though the wave functions of the f-electrons causing the high magnetic moment are strongly localized and do not overlap. This interaction can now be either ferro- or antiferromagnetically depending on the spatial separation of the localized moments and the Fermi vector (k_F) of the conduction electrons. This oscillatory character of magnetic interaction can readily be seen in the form of the modified Heisenberg-Hamiltonian for the RKKY-interaction:[65,66]

$$\mathcal{H} = -9\pi \frac{J^2}{\epsilon_F} \left(\frac{N_e}{N} \right)^2 F(2k_F|\mathbf{R_n} - \mathbf{R_m}|)\mathbf{S_n} \cdot \mathbf{S_m} \tag{2.4}$$

with the exchange integral J between spins $\mathbf{S_n}$ and $\mathbf{S_m}$ at positions $\mathbf{R_n}$ and $\mathbf{R_m}$. The function $F(x) = \frac{-x\cos x + \sin x}{x^4}$ includes the oscillary character of the RKKY interaction, the so-called Friedel-oscillations.[67] In particular, the period length depends crucially on the distance between interacting spins and the Fermi vector.

This RKKY-model was the basis for the proposal of a carrier mediated interaction in (Ga,Mn)As.[68,69] It turned out that for (Ga,Mn)As the simpler Zener-model[70,71] is applicable. It is similar to the RKKY-model in its main aspects, but the Friedel-oscillations are neglected. This is justified by the low carrier concentrations and comparable large separations of the individual Mn atoms, both a result of the low Mn doping level. The "first" oscillation is dominating and further contributions are discarded since the length scale of the oscillation is $l_{osc} \propto 1/k_F$ (see Fig. 2.9).

The inset of Fig. 2.9 visualizes the whole situation. Mn takes an ambivalent role. First, it provides p-like itinerant holes as an acceptor. Secondly, by remaining in the high-spin configuration $3d^5$ it provides a localized magnetic moment. The hole becomes spin-polarized antiferromagnetically to the first Mn ion. Then, it couples again antiferromagnetically to the next Mn ion. As a result, there is a net ferromagnetic interaction between the Mn ions.

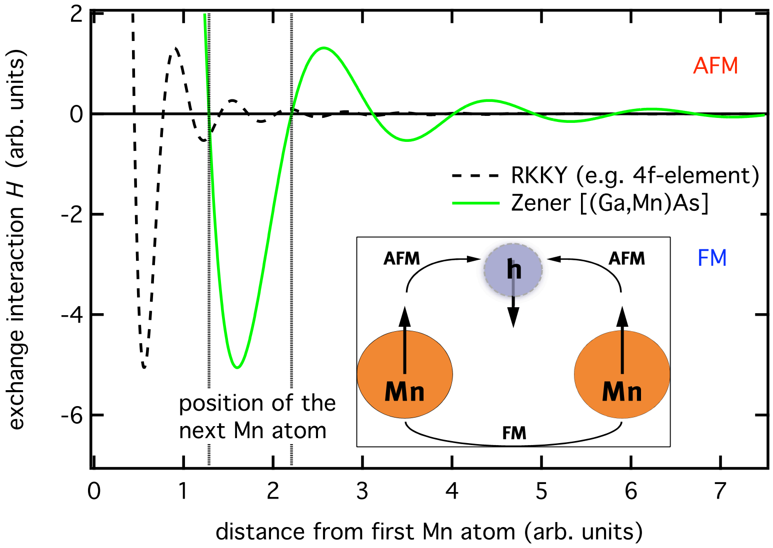

Figure 2.9: *Sketch of the Friedel oscillations; the comparison of the RKKY Hamiltonian [Eq. (2.4)] for two different carrier concentrations. The black dotted line shows a high carrier concentration, which leads to spatial oscillations with shorter wave lengths. Low carrier concentrations (green solid line) as in the case of (Ga,Mn)As lead to a larger width. So, the first negative amplitude dominates the magnetic behavior since it includes the typical Mn-Mn distance.*[49] *The primal Mn atom is located at the origin. Negative values on the ordinate indicate ferromagnetic, positive values antiferromagnetic interaction. The inset shows a sketch of the interaction. One Mn ion couples antiferromagnetically to an itinerant hole, which, in the next step, couples antiferromagnetically to the next Mn ion. Thus, both Mn ions couple ferromagnetically.*

Based on the Zener-model, a mean-field approximation gives an analytical relation for the Curie temperature in (Ga,Mn)As:[72]

$$T_c^{MF} = J_{pd}^2 \cdot x \cdot p^{1/3}/t \tag{2.5}$$

here, J_{pd} is the coupling between TM d- and host p-states (sometimes also referred to as $N_0\beta$), p is the hole concentration, x the Mn concentration and the bandwidth $t \propto 1/m^*$ (m^* being the effective mass of the carriers). The cubic root of the hole concentration enters the equation via the Fermi vector k_F which depends on $\sqrt[3]{p}$.[58] In Eq. (2.5) the hole and Mn concentrations are not set equal since this formula already accounts for possible compensation effects by interstitial Mn or As-antisites.

Throughout the literature, this model is currently the most widely accepted one. Though it is capable to explain most of (Ga,Mn)As properties both qualitatively and quantitatively, it exhibits some weaknesses. The mean-field approximation, which is the basis of the RKKY-like interaction, is valid only if the interaction radius is much larger than the average inter-spin distance. Due to crystal imperfections the former is in the same order as the latter (typically $0.5 - 0.7\,\mathrm{nm}$).[73] Additionally, the validity of a mean-field approximation in the presence of strong disorder, as given in (Ga,Mn)As, remains questionable. Furthermore, the charge carriers are assumed to be in an unperturbated valence or conduction band, which brings the effective mass into the calculation. Taking a GaAs host, the carriers are hence p-like. However, as has been outlined in Sec. 2.1.1, doping a semiconductor in the percentage range ultimately leads to degeneracy. Mn acceptor centers can not be seen as isolated impurities any more. The wave functions begin to overlap and to correlate with each other. Therefore, doubts arise if the valence band – RKKY picture is appropriate for (Ga,Mn)As.

2.2.3 The impurity band – double exchange picture

In recent years, more and more theoretical[74,75] and experimental[16,22,76] evidences suggest, that the simple picture of an unperturbated hybridization of Mn $3d$-states and host $4sp$-states is not correct. For instance, magnetic circular dichroism (MCD) measurements show that ferromagnetism behavior is not simply explained by a spin-polarized hole.[77] On the other hand, band structure calculations[75] clearly show the formation of an impurity band by the Mn $3d - t_{2g}$ orbitals, which are above the valence band edge (the Mn $3d - e_g$ levels lie within the valence band of the host due to the tetrahedral symmetry of the zinc blende lattice) for $x = 6.25\,\%$. The carriers have thus a predominantly d-character.[75]

Especially transport measurements have provided many evidences for the presence of an impurity band in (Ga,Mn)As.[78–80] It has been confirmed that the Fermi energy lies within the impurity band[22,78] and it was concluded that the carriers have a significantly higher mass compared to pure GaAs. The effective mass of the holes is $m^* \approx 10 m_e$, whereas for pure GaAs: $m^*_{lh} = 0.076 m_e$, $m^*_{hh} = 0.5 m_e$.[9,78] Interestingly, the mass also shows a dependence on the magnetic transition temperature, what is known from the double exchange manganites.[81] A further result of the considerably heavier charge carriers is a reduced mobility ($1 - 2\,\mathrm{cm^2/Vs}$, highly doped GaAs without magnetic ions: $\mu_D = 400\,\mathrm{cm^2/Vs}$). The increased mass can be seen as a direct consequence of the impurity band, which, in general, has little dispersion.

Furthermore, a perturbation of the crystal potential by the substitution of As by other pnictides (P or N) has drastic consequences.[80] Isovalent substitution of As in the per mill range does not only lead to a dramatic decrease in T_c and a metal-to-insulator transition at lower temperatures. Also the magnetic anisotropy, the orientation of the magnetic easy and hard axes, is changed. This is a direct consequence of the carrier concentration dependence of the anisotropy.[80]

In this sense, the transport properties have been explained in the framework of a valence band anticrossing.[82] This explains the mobility and high effective mass by the formation of an impurity band. Also, the strong sensitivity of the resistivity on pnictide co-doping is a direct outcome of the alloy disorder scattering, which is strongly dependent on the effective mass. Complementary methods, like cross-section scanning tunneling microscopy (XSTM), also deliver direct evidence for the presence of an impurity band.[83]

In order to keep the RKKY-model alive, even though an impurity band is formed, a merge of impurity band and valence band has been proposed. It is believed that valence band and impurity band are separated in the low doping limit ($< 1\,\%$). Upon doping the impurity band broadens and finally overlaps with the valence band as shown in Fig. 2.10.[76] Electrochemical capacitance-voltage measurements indicated, that within a Mn concentration of $5 \times 10^{18}\,\mathrm{cm}^{-3}$ ($0.045\,\%$) and $2 \times 10^{20}\,\mathrm{cm}^{-3}$ ($1.8\,\%$) an impurity band is present which merges with the valence band for higher doping levels. Theoretical studies support this picture where the unification of the impurity band and the valence band is a strong function of Mn concentration x, exchange coupling J, and Coulomb attraction V (between Mn impurities and holes).[84] In short, (Ga,Mn)As in the relevant x regime and with reasonable J and V values is calculated always to be in the merge picture.

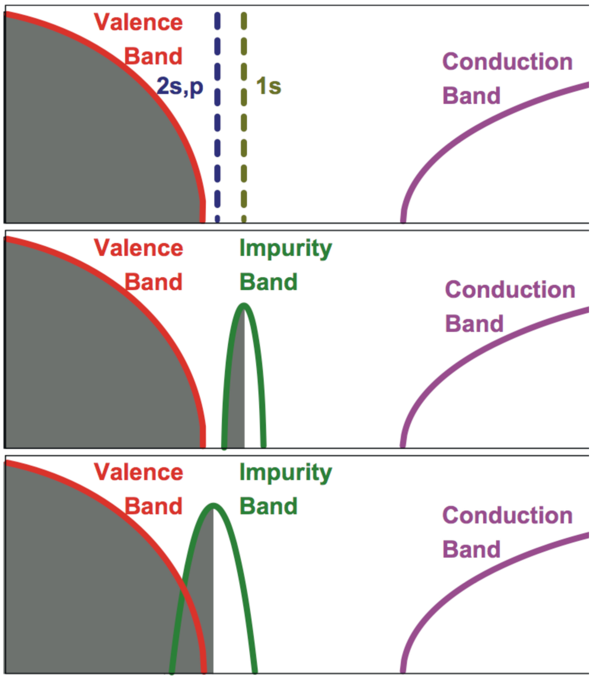

Figure 2.10: *Sketch of the Mn-related impurity band in (Ga,Mn)As; top panel: hydrogenic states of an acceptor state in the band gap of $Ga_{1-x}Mn_xAs$. Middle panel: with increasing doping the acceptor states broaden to an impurity band which overlaps with the valence band upon further doping (lower panel). The two lower pictures resemble a degenerated semiconductor. Adopted from Ref. 76.*

Nevertheless, all the aforementioned discrepancies gave doubt on the RKKY picture. Therefore, another model for the magnetic coupling was taken up again. This earlier model explicitly requires an impurity band.[85] For (In,Mn)As, a close cousin of (Ga,Mn)As, the ferromagnetic interaction can be described by a hopping mechanism,[86,87] known as *double exchange* (DE). The manganese $3d$-electrons hop to the anion and further to the next Mn cation. In special configuration with two different Mn valences present (d^4–d^5 or d^5–d^6), this indirect exchange gives rise to ferromagnetic coupling. A similar mechanism is known for manganites. There, the DE causes the colossal magnetoresistance behavior in this material class. Unfortunately, the initial assumption that Mn is only in the d^5-configuration (Mn^{2+}) would prohibit the hopping. However, it turns out that this simple ionic picture is hardly applicable to (Ga,Mn)As. Not only has it been shown by Raman scattering[16] and resonant x-ray emission spectroscopy (ResXES)[88] that valence fluctuations are indeed present, but that Mn is more likely in the d^4-configuration (Mn^{3+}) for higher Mn concentrations. The similarity between (Ga,Mn)As and manganites in the case of the aforementioned T_c-dependence of m^* further favors the DE picture in (Ga,Mn)As.

But this model has also a major drawback. The hopping requires a large amount of Mn-As bonds, which are not present for Mn concentrations in the percentage range. A doping of 5 % Mn means that only one out of 20 Ga atoms is substituted. Therefore, a simultaneously bonding of one As to two Mn is very rare. The Mn doping illustrated in Fig. 2.5 (a) is already exaggerative. In consequence, the mean distance between the ferromagnetic ions is too large to lead to long-range ferromagnetic ordering. Conversely, larger concentrations give rise to hopping when the mean distance between Mn ions decreases.[89]

It should be noted that even a combination of both models was proposed.[90] This so-called *double resonance mechanism* includes the RKKY- and the DE-model in the limit of low and high doping levels, respectively. Note, that this model is not to be confused with the merge picture described above.

Summing up all facts it becomes clear that the origin of ferromagnetic ordering in (Ga,Mn)As is still hotly debated in the literature. From the theoretical side none of the models is capable to explain all experimental details without breaking others. From the experimental side the simultaneous presence of complex composition, compensation effects, and anomalous behavior makes a correct interpretation of the data challenging. However, a decent understanding of the ferromagnetism in (Ga,Mn)As is urgently required both to further raise the Curie temperature and to transfer the findings to other FS systems.

2.2.4 Post-growth annealing of (Ga,Mn)As

Despite intense efforts in sample growth over the years the physical properties of (Ga,Mn)As remained unsatisfactory. It was possible to improve the structural properties by optimization of growth parameters, however, it was not possible to raise the Curie temperature from the initial 60 K[6] to more than 110 K. Also the transport properties stayed far behind standards for applications.

As described in Sec. 2.2.1 the huge amount of defects, in particular interstitial Mn, leads to a worsening of the transport and magnetic properties. Not only does the Mn self-compensation lead to a reduction of the carrier concentration, but there is also a direct coupling between Mn_{sub} and Mn_{int}. Theoretical calculations indicate that a formation of a Mn_{sub}-Mn_{int}-dimer is favorable with an energy gain of at least 0.3 eV. Furthermore, as x-ray absorption spectroscopy in magnetic circular dichroism (XAS-MCD) showed, the magnetic moment is reduced from approximately $4\,\mu_B$ for pure substitutional Mn to $0.8\,\mu_B$ for a Mn_{sub}+Mn_{int}-dimer.[91] This means that interstitial Mn couples antiferromagnetically via a "direct superexchange" to a neighboring substitutional Mn.[92] Hence, this partially frustrated antiferromagnetic alignment of the Mn ions further deteriorates the magnetic properties.[93] Interestingly, theoretical calculations based on Monte-Carlo simulations and density functional theory[14,74] indicate that a partial compensation of the carriers might even strengthen the ferromagnetism. Estimations show that half a hole per substitutional Mn atom is optimal for the magnetic properties ($4\mathrm{Mn}_{sub} + 1\mathrm{Mn}_{int}$).

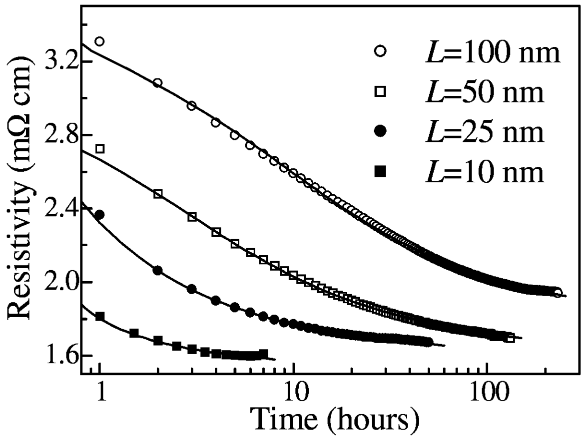

Figure 2.11: *Dependence of ρ on the annealing times of as-grown (Ga,Mn)As samples with various film thicknesses; prior to the annealing the resistivity of (Ga,Mn)As shows a clear dependence on the film thickness. The annealing leads to a less pronounced behavior. From Ref. 94.*

In 2002, Edmonds *et al.*[95] showed that annealing of (Ga,Mn)As subsequently to the growth results in a tremendous improvement of both the transport and magnetic properties. The recipe consists of annealing the samples at moderate temperatures (typically 190°C), close to the growth temperature for comparable long durations (typically 100 h) in air. Especially the temperature is a crucial parameter, since it was shown already in Fig. 2.6 that higher temperatures can lead to a phase separation (MnAs clusters). Note, that the term of annealing is from now on used for the thermal preparation of (Ga,Mn)As *ex situ* in order to improve the physical properties. The term "tempering" refers to thermal treatment *in situ* in order to improve the surface quality.

Samples with various doping concentrations showed metallic behavior after this annealing procedure.[94,95] Additionally, an initially pronounced film thickness dependence of the conductivity was eliminated (*cf.* Fig. 2.11).[94] Simultaneously, the magnetic properties, such as T_c and remanence, increased dramatically.[96,97]

It was clear that the sub-optimal quantities are a direct consequence of the non-equilibrium growth conditions and the resulting defects. However, the annealing temperatures are definitively too low to heal out structural defects. The temperatures required for a heal out would have an opposite effect.[98]

Thermal activation of interstitial Mn was made responsible for the optimization process very soon.[51] Mn_{int} is neither covalently nor ionically bound in the lattice. Hence, the activation energy is expected to be smaller than for Mn_{sub}. Though the thermal energy scale in the annealing process is rather small ($190°\mathrm{C} \approx 460\,\mathrm{K} \approx 40\,\mathrm{meV}$), the comparable long time compensates the low thermal energy. Since the thermal segregation process is proportional to an exponential factor, long annealing times are sufficient to allow for a large scale segregation.

The absolute value of the activation energy is an issue of intense research. Latest calculations indicated a dependence on the charge state of the interstitial Mn (i.e., Mn^{+} or Mn^{2+}). The literature gives an energy of $0.55 - 0.95\,\mathrm{eV}$,[50] in good agreement with the experimental value of $0.7\,\mathrm{eV}$.[94] However, recently a barrier of $1.4\,\mathrm{eV}$ was proposed.[98]

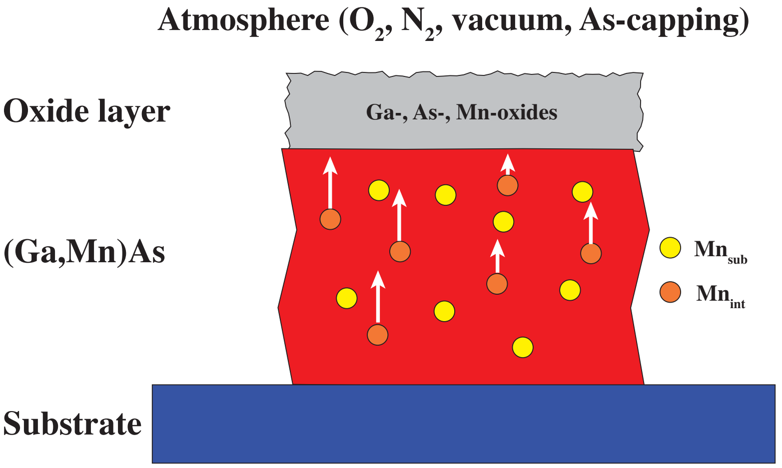

Figure 2.12: *Sketch of the thermal activated surface segregation of interstitial Mn in (Ga,Mn)As; the weakly bound interstitial Mn segregates and is passivated at the surface. Either longer annealing times* ($\geq 200\,h$ *at* $T = 190°C$) *or higher temperatures lead to a significant segregation of substitutional Mn or a phase separation by formation of MnAs.*[97]

Additional evidence for the claim, that segregation of interstitial Mn is responsible for the increase in T_c and decrease of ρ, comes from the fact, that the removal of As_{Ga} would only result in an decrease of ρ whereas the net magnetic moment per Mn atom is only limited by the antiferromagnetical alignment of Mn_{sub}-Mn_{int} dimers. Moreover, a fourfold increase in the overall Mn concentration at the surface was observed (see Sec. 5.1).[97]

Even though both electronic and magnetic properties are increased in the aftermath, the respective time scale differs. Annealing times of 10 h are sufficient to improve the transport characteristics, as can be seen in Fig. 2.11. The magnetic properties require considerable longer times, i.e., T_c reaches its maximum value not before 50 h.[96,97]

The annealing process is schematically shown in Fig. 2.12. The loosely bound interstitial Mn segregates to the surface and is subsequently oxidized.[99] The oxidation leads to a passivation of the Mn, which, in turn, cannot act as an double-donor anymore. For the optimization of (Ga,Mn)As annealing under oxygenic atmosphere has proven to be the most effective.[99] Annealing under vacuum leads to various Mn valences.[100] Nitrogen atmosphere seems to be less efficient than oxygen,[101] whereas As-capping leads to the formation of MnAs at the surface.[102]

However, annealing times beyond 200 h can also lead to a negative effect. The activation energy for substitutional Mn is larger in comparison to interstitial Mn, but for very long annealing times Mn_{sub} can also start to segregate. For times shorter than 200 h, no segregation of substitutional Mn has been observed.[58]

The annealing process has further been optimized leading to a maximal Curie temperature of 185 K at present.[103] This method requires an elaborate process of sequential annealing, wet-chemical etching, and re-oxidation steps.[4] Despite this, all annealing processes performed in this thesis are according to the static annealing proposed by Edmonds *et al.*[94]

It is doubtful if further improvements in the growth and post-growth annealing can ultimately lead to ferromagnetic order in (Ga,Mn)As at room-temperature (RT). Nevertheless, a detailed understanding of the ferromagnetism in (Ga,Mn)As can be the guide for other FS systems and by doing so, finally lead to a semiconductor being both ferromagnetic and applicational relevant.

3 Aspects of photoemission spectroscopy

3.1 Photoelectric effect

3.1.1 Basic theory of PES

The basic principle on which photoemission spectroscopy (PES) is footed, is the photoelectric effect, discovered in 1887 by H. Hertz[104] and explained in 1905 by A. Einstein.[105] A photon with energy $h\nu$ hits a solid and excites an electron from an occupied shell. If the energy of the photon is large enough, the photoelectron can leave the solid. Large enough in this context means that both the binding energy of the electron E_{bin} as well as the work function Φ have to be paid. Hence, the remaining kinetic energy of the photoelectron E_{kin} is given by:

$$E_{kin} = h\nu - E_{bin} - \Phi \tag{3.1}$$

The binding energy is determined by the atom, whereas the work function is material dependent. In particular the chemical sensitivity provided by the binding energy is one reason why PES is nowadays one of the most important and most widely used analysis techniques, not only in physics, but also in chemistry and material science.

A rough sketch of the geometric realization is given in Fig. 3.1. Photons with energy $E_{ph} = h\nu$ from a light source (see below) hit the sample under an angle ϑ with respect to the sample plane. After the excitation, electrons with kinetic energy E_{kin} [given by Eq. (3.1)] and momentum $\vec{k}$ leave the sample with an angle α with respect to the surface normal.

The energy diagram of a PES experiment is illustrated in Fig. 3.2. The left hand side represents the situation in the solid. Electronic states up to the Fermi energy E_F are occupied, which itself is separated from the vacuum level by the work function Φ. The valence band (VB) is simplifyingly displayed by a parabolic DOS. The deeper bound core levels are δ-function like. In a PES spectrum, the core lines are broadened due to the finite life time of the core hole. The DOS near the Fermi energy has to be convoluted with the Fermi-Dirac statistic. Figure 3.2 is over-simplified, however, it can help to illustrate how an actual PES spectrum is formed.

Since the work function is the minimal energy required to excite an electron from the Fermi surface, light sources with a photon energy in the ultra-violet regime or higher are

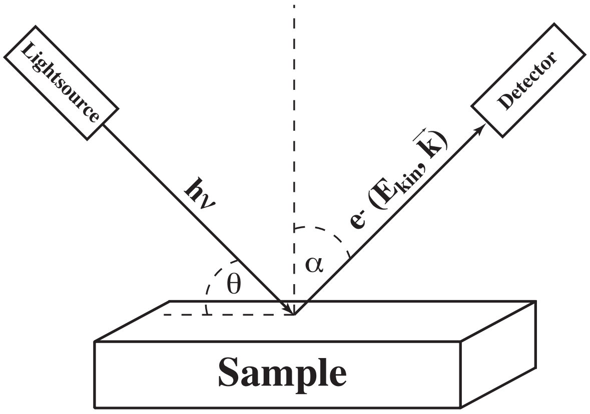

Figure 3.1: *Sketch of the geometry of a PES experiment. Light with energy $h\nu$ from a light source impinges under an angle ϑ relative to the surface plane on to a sample. Electrons with energy E_{kin} and momentum $\vec{k}$ leave the surface with an angle α relative to the surface normal. The escape angle can be characterized further by the azimuth angle φ around the sample normal.*

required. Typical light sources are gas discharge lamps (HeI=21.2 eV or HeII=40.8 eV), x-ray tubes (Al K_α = 1486.6 eV or Mg K_α = 1253.6 eV), or synchrotron storage rings, which provide tunable photon energies.

Quantum-mechanically speaking, the photoeffect can be described as a perturbation of the initial state, and can thus be calculated in the dipole approximation with the aid of time-dependent perturbation theory. The probability follows Fermi's "golden rule":[107]

$$P_{i\to f} \propto \sum_i |\langle \Psi_f | \hat{A}\cdot\hat{P} + \hat{P}\cdot\hat{A} | \Psi_i \rangle|^2 \delta(E_f - E_i - h\nu) \tag{3.2}$$

The electron is perturbated by the vector potential $\hat{A}$ of the electro-magnetic field from the initial many-body wave function Ψ_i into a final state Ψ_f. The delta-function ensures energy conservation. The equation already accounts for the fact that not a single particle wave function has to be considered but the wave function of the entire system. Often, these wave functions may be assumed to be independent particle states. However, there is a decisive difference between the initial and final state.

Following the Franck-Condon principle, the excited photoelectron is instantly removed from the system (sudden approximation). The remaining $(N-1)$-electron system of the final state is, however, still an eigenstate of the N-electron system of the initial state, and not of a $(N-1)$-electron initial state. So, the final state has to be expanded into the eigenstates of the $(N-1)$ particle system. This leads, in general, to a manifold of spectral distributions, since many of the $(N-1)$-electron system final states will have a considerable overlap with the $(N-1)$-electron system initial states in the matrix element in Eq. (3.2).[108]

This so-called *one-step model*, in which the excitation and detection is treated in a single coherent process, is mathematically correct, yet rather complex. A more plain

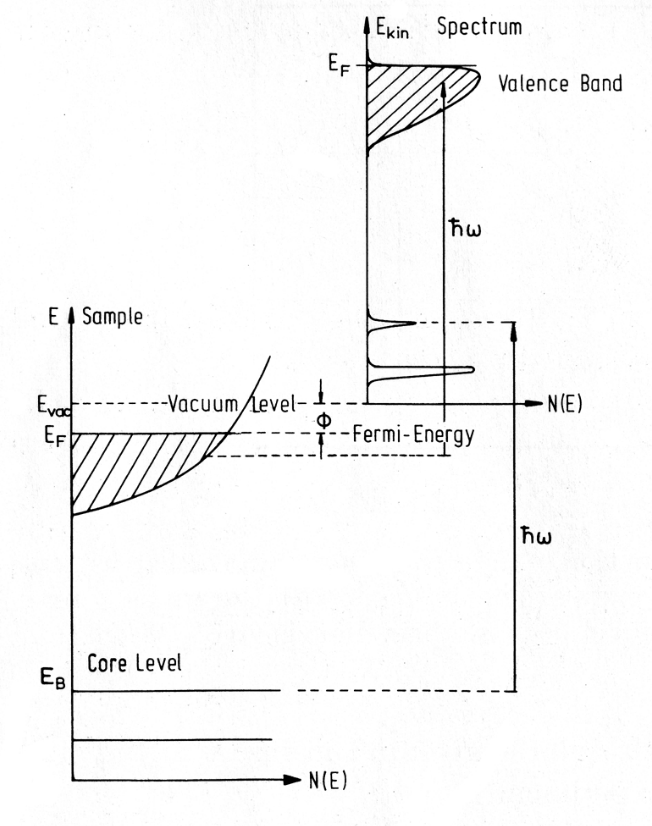

Figure 3.2: *Sketch of the energy diagram of a PES experiment. δ-peak like core levels with comparably high binding energies are broadened to Lorentzians in the spectrum due to the finite life time of the core hole. The valence band near the Fermi edge is convoluted by a Fermi-Dirac statistic in the final spectrum. The work function is given by the difference between the vacuum level and the position of the Fermi energy in the solid. Adopted from Ref. 106.*

approach to the matter is the so-called *three-step model*, which even though it is at best a crude simplification has proven to be quite successful.[106] Here, the entire process is artificially split into three strictly *independent* steps:

(i) optical excitation of the photoelectron

(ii) ballistic transport to the surface

(iii) escape to the vacuum

The energy loss structures resulting from a quantum mechanically correct solution of Eq. (3.2) are therein ascribed to several intra- and interatomic processes. Some of these excitations are described and quantified later on within this model. Intra-atomic processes, such as intrinsic plasmons or shake-up satellites are caused in step one. Step two is responsible for most of the energy loss of the photoelectron, as will be described in more detail in Sec. 3.2, and for the surface sensitivity of PES. The third point is responsible for surface excitations, backscattering, and diffraction.

It has to be stated, that the *three-step model* is an entirely phenomenological approach and does not reflect the correct situation. However, it is a much more intuitive approach to understand the origin of loss structures in the spectra. Moreover, a correct solution of Eq. (3.2) is particularly required for high-resolution valence band spectroscopy, whereas for core level spectroscopy, which makes up the main body of the upcoming results, a detailed mathematical description is unnecessary.

Finally, it should be noted, that in many cases, a severe drawback of PES is its surface sensitivity, which will be dealt with in more detail in Sec. 3.3. This is not due to the limiting penetration depth of the photons. Their attenuation length is several orders of magnitude larger than the escape depth of the photoelectrons, which is in the nm- or sub-nm range. This surface sensitivity is one of the reasons why PES has to be performed in ultra-high vacuum apparatus with base pressures $\leq 10^{-10}$ mbar. Only under these conditions it is possible to measure highly reactive samples without major effects of surface contamination. The finite range of VUV or soft x-ray light as well as of the photoelectrons in air is another reason for the demand of suitable vacuum technology.

3.1.2 Resonant photoemission spectroscopy

Since measurements with resonant PES (ResPES) have been conducted in the course of this thesis, this special case of PES shall also be outlined here. A detailed description can be found in the literature.[109]

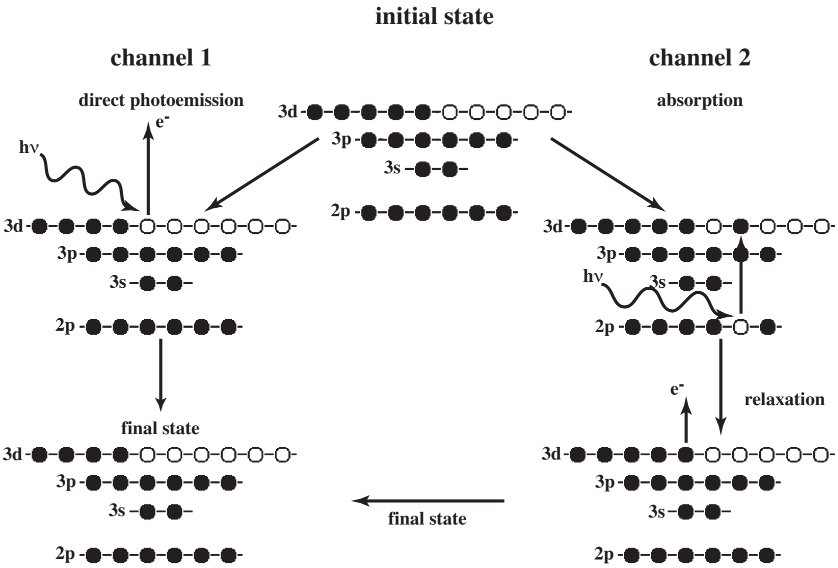

Figure 3.3: *Sketch of resonant PES. Both channels, the direct photoemission and the Auger-like radiation-free decay, interfere coherently, thereby producing a resonant increase of the 3d-signal.*

Figure 3.3 shows the principle idea of ResPES. On the left hand side, the ordinary photoemission process is shown. A photon excites a $3d$-electron. This can be written as:

$$2p^6 3d^n + h\nu \rightarrow 2p^6 3d^{n-1} + \epsilon_k \tag{3.3}$$

Additionally, the interaction of light with matter can also lead to another effect. If the incident photon energy resonates with a core-electron excitation threshold, the intensity of the photoemission is resonantly enhanced. This means, that an electron from a deeper core level can be excited directly into the free $3d$-states. In this case, it has to be a $2p$-electron, since the dipole selection rule $\Delta l = \pm 1$ has to be fulfilled. This state reads then:

$$2p^6 3d^n + h\nu \rightarrow 2p^5 3d^{n+1} \tag{3.4}$$

Then, this excited state has two different channels to relax. Firstly, by a radiative decay where the electron falls back to its original core level and emits a photon with an energy corresponding to the energetic difference between the $3d$ and $2p$ core levels.

The other possibility is an Auger-like process, where an electron falls back as before, but the energy is not emitted via a photon but transferred to another $3d$-electron, which can leave the atom. Again, the energy is the difference between the two core levels. The final state of Eq (3.4) reads then:

$$2p^5 3d^{n+1} \rightarrow 2p^6 3d^{n-1} + \epsilon_k \tag{3.5}$$

As can readily be seen, the latter process and the direct PES channel have the same final state [Eq. (3.3) and Eq. (3.5)]. Therefore, these two final states can interfere coherently if the energy is chosen properly. If the photon energy is too large, only an incoherent superposition of the two channels is observed.

The coherent interference has one important consequence. It leads to a drastic increase of the $3d$-contribution to the spectrum. By subtracting an *off-resonance* spectrum (below the absorption threshold) from an *on-resonance* spectrum, the pure $3d$-contribution to the spectrum near the Fermi edge can be determined. This is of particular interest, since in matter with highly correlated electrons the main physics is derived by the unfilled d- or f-shells. However, these states in the valence band near the Fermi edge have, in general, a small cross section and the hybridization with the other—let's say—p-states complicates a determination of the pure d-states, both in position and shape. Therefore, ResPES is meanwhile the method of choice if detailed insight into the open d- or f-states is to be gained.

3.2 Many-body effects and energy loss structures

Going back to the theoretical considerations in Sec. 3.1.1, several spectroscopical consequences of the differences between the N- and $(N-1)$-electron systems shall be described in more detail. The argumentation is based on the *three-step model*, since it provides a much more intuitive approach. Furthermore, since final state effects are only discussed qualitatively omitting the extraction of quantitative information, a mathematically correct solution is not required.

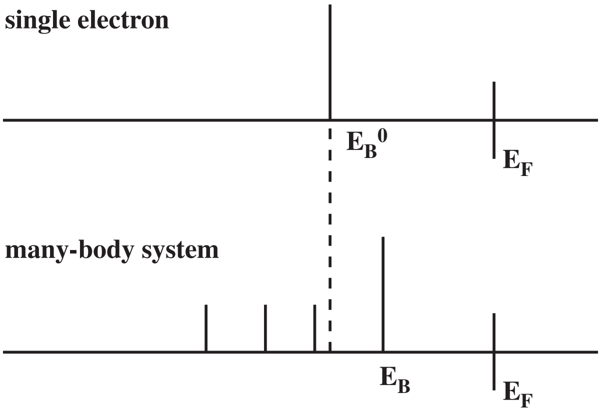

Figure 3.4: *Sketch of a PES spectrum of a single electron and a many-body system. In a single electron system (upper case), the spectra shows only a single peak at the binding energy E_B^0. In a many-body system (lower case), electron correlations will cause several satellite structures. Every overlap between $(N-1)$-initial and $(N-1)$-final state will cause a satellite. The main line will also significantly differ from the previous case. The center of gravity of the entire spectrum, however, will still coincide with the single electron case. According to Ref. 106.*

The situation is schematically illustrated in Fig. 3.4. The upper case represents the hypothetical situation of a single particle state, neglecting correlations. A photon excites an electron and via Eq. (3.1) a certain binding energy E_B^0 can be determined. This binding energy is also sometimes referred to as Koopman's binding energy.

The lower case represents the situation in a solid. The many-body system will cause several satellite structures in the spectrum. While the center of gravity further coincides with the Koopman's binding energy, the overall spectrum becomes a complicated manyfold of several structures.[106]

A great variety of possible mechanisms have been observed. Which process leads to significant contributions depends on many different parameters, above all, the electronic properties of the material under investigation. It is beyond the scope of this thesis to describe all possible mechanisms proposed in the literature. The attention is rather focussed on processes which have been observed in the course of this study, and are particularly pronounced in DMS. Several of them lead only to an unwanted background, however, others allow for important conclusions on the fundamental physics of (Ga,Mn)As.

3.2.1 Plasmon excitations

Plasmons, collective longitudinal oscillations of the electron gas (see Fig. 3.5), are a prominent feature within XPS spectra.[110,111] They are also responsible for a large part of the energy loss of photoelectrons and the surface sensitivity of PES in general. Therefore, they are explicitly accounted for in the inelastic mean free path (IMFP) equations [*cf.* Eq. (3.9)].

Their creation can well be understood in the framework of the three-step model introduced in Sec. 3.1.1. On the way through the crystal (step 2) the photoelectron can interact with the electron gas and thereby induce oscillations. These oscillations are quantized by the bulk plasmon frequency $\omega_B = \sqrt{\frac{n \cdot e^2}{\epsilon_0 m^*}}$, with the carrier concentration n, the elementary charge e, the dielectric constant ϵ_0, and the effective mass m^*. They appear in the spectrum as wide peaks at positions equal to integer multiples of the bulk plasmon energy $E_B = \hbar\omega_B$, with decreasing intensity for higher integers. As the plasmon energy is proportional to the square root of the carrier concentration, ω_B is influenced by doping. Since the room-temperature (RT) conductivity of GaAs is largely determined by the intrinsic conductivity, effects of doping are not seen at RT. Bulk plasmons in GaAs have an energy of 15.8 eV.[112,113]

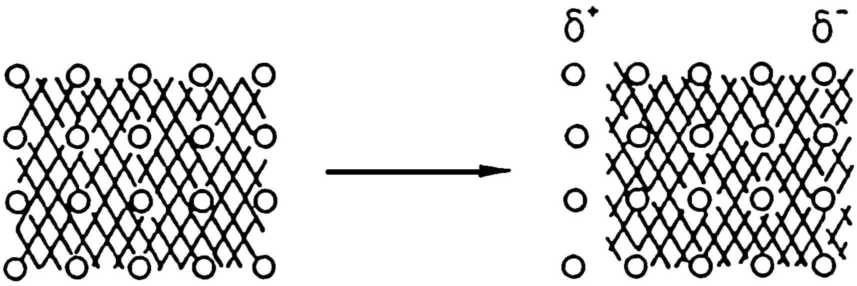

Figure 3.5: *Sketch of a plasmon excitation in the long-wavelength limit; circles indicate the positively charged fixed ions, the hatched area indicate the electron gas. After the excitation, partial charges δ^+ and δ^- are induced. Taken from Ref. 114.*

Bulk plasmons are a consequence of step 2 in the three-step model. Besides them, surface plasmon can be excited during step 3. They are lower in energy (as a rule of thumb from metals:[115] $E_S = E_B/\sqrt{2} \approx 10\,\mathrm{eV}$) and naturally utmost sensitive to surface effects, for instance oxidation. They do not show a multiplicity since only one surface plasmon can be excited by an electron leaving the surface. However, electrons undergoing both bulk and surface loss processes can sometimes be identified in the spectra as separate peaks.

Those two processes in step 2 and step 3 are referred to as "extrinsic plasmons" since they occur on the path of the electron through the crystal. Nevertheless, also in step 1 the electron gas can simultaneously be excited. These plasmons are intrinsic properties of the solid and therefore dubbed ”intrinsic plasmons.” They are also a singular event and coincide energetically with bulk plasmons. Whether they make up a significant contribution to the spectra or not is still under discussion.[110,111]

Plasmon peaks show up in XPS spectra forming a so-called ”plasmon sideband,” however, PES is not in particular well suited to determine their exact positions. A determination of the electron loss-function via optical conductivity measurements[112] or characteristic energy loss experiments[113] provides more reliable data on plasmon peaks. Figure 3.6 shows the data of Philipp *et al.*[112] and von Festenberg[113] on GaAs. In optical measurements the loss-function is determined indirectly via the relations $\Im\left(\frac{-1}{\epsilon}\right)$, where the dielectric function ϵ is obtained from reflectance/transmission experiments.

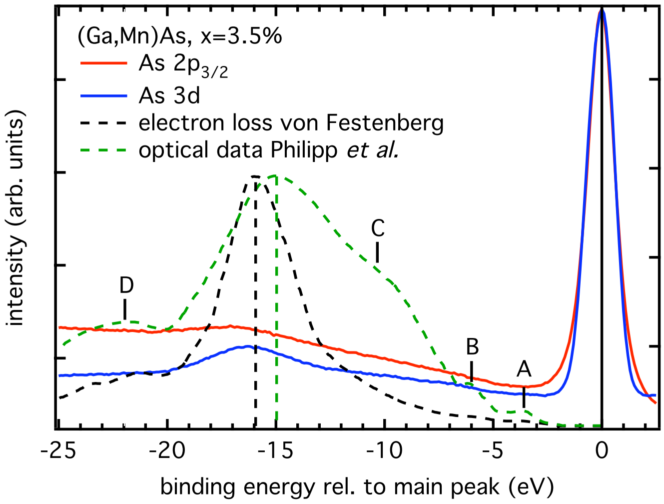

Figure 3.6: *Energy loss spectra of GaAs as reported in the literature compared to the As $2p_{3/2}$ (red) and As 3d-doublet (blue) core level region. The green dashed line shows the optical data[112] and the black dashed line the electron energy loss measurements.[113] Fine structures, in particular present in the optical data, are labeled A to D.*

The data in Fig. 3.6 show that the main centroid of both methods do not fall upon each other. Philipp and co-workers[112] attributed the smaller value for the optical data to an insufficient surface preparation. Furthermore, optical data are, in general, much more surface sensitive than energy loss measurements and determine the loss-function not directly but indirectly via a Kramers-Kronig analysis. Therefore, the value of 15.8 eV by von Festenberg is taken as the bulk plasmon frequency of GaAs. Besides the drawback of a higher surface sensitivity, the optical measurements provide a considerably higher energy resolution. This allows for the observation of several fine structures, labeled A to D in Fig. 3.6. All four peaks are basically excitations of bound valence electrons into unoccupied states above the Fermi energy. Valence band spectra and band structure calculation can help to identify the corresponding excitation paths. Table 3.1 gives the responsible excitations.

Table 3.1: *Electron transfer seen in optical conductivity measurements on GaAs. The letters reflect the peaks in Figs. 3.6. The second column gives the responsible element, and the corresponding transitions are given in the last two columns.*

peak	element responsible	initial state		final state
A	Ga	$4p^1V^n + h\nu$	$\rightarrow$	$4p^0V^{n+1}$
B	As	$4p^3V^n + h\nu$	$\rightarrow$	$4p^2V^{n+1}$
C	As	$4s^2V^n + h\nu$	$\rightarrow$	$4s^1V^{n+1}$
D	Ga	$3d^{10}V^n + h\nu$	$\rightarrow$	$3d^9V^{n+1}$

The question arises if contributions from intrinsic and extrinsic plasmons can be separated, which is a non-trivial task.[116] It turns out that they can be distinguished by a careful analysis of a series of plasmons of the same core level, because they have very different intensity decay rates with increasing order n. Intrinsic plasmons are Poisson distributed and thus, the scattering probability P is given by $P(n) = \frac{b^n}{n!}e^{-b}$, with the intrinsic plasmon creation rate b. In contrast to this, extrinsic plasmons follow a power law, reading $P(n) = a^n$, with the extrinsic plasmon creation rate a. This can help to separate intrinsic (carrying fruitful information on the composition etc.) and extrinsic contributions.

Plasmon effects are not necessarily strongly present in all materials. Simple metals (alkaline and earth alkaline metals) and *sp*-metals (Ag, Au) tend to show the strongest plasmon sidebands, whereas TM exhibit negligible plasmon contributions. This can easily be seen when comparing electron loss spectra or optical measurements. Aluminium, for instance, shows a peaked plasmon resonance in the energy loss spectra in contrast to copper, which has a more or less featureless hump.[117] The energy loss-function of GaAs is in a medium regime. Thus, plasmon contributions have to be considered in GaAs.

The relative intensity of bulk plasmon contributions to core level spectra show a stronger energy dependence than surface plasmon contribution, since the higher kinetic energy of the photoelectron (lower binding energy) implies a longer path of the electron through the crystal. This can be seen in Fig. 3.6. The intensity of the plasmon compared to the main centroid is larger for the As $3d$ core level than for the $2p$ (note that *no* background has been subtracted). Surface plasmons on the other hand are (at least for kinetic energies larger than—let's say—300 eV) independent of the probed depth, since they occur only in step 3 of the three-step model.

Finally, it shall be pointed out, that the strict distinction between extrinsic and intrinsic, bulk and surface plasmons is a artifact of the framework of the *three-step model*, not present in the *one-step model*. However, in the light of a qualitative description of the spectra the more imaginable approach is seen to be superior to the mathematically correct treatment.

3.2.2 Charge-transfer satellites

Further important final state contributions are so-called charge transfer (CT) satellites. This feature is in particular pronounced in TM with an open *d*-shell, e.g., Mn. Therefore it shall briefly be described here.

After the ejection of the photoelectron, the atom is left with one hole in the core shell. The less screened core potential can now cause the unfilled *d*-shell to slip energetically into the valence band, below the level of the ligand. Thus, it is energetically favorable to transfer one electron from the ligand to the *d*-shell. The final state then changes from d^nL to $d^{n+1}L^{-1}$, where n is the electron count in the *d*-shell and L^{-1} indicates an additional hole in the ligand shell. The energetic difference shows up as the separation between the two lines associated with both final states.

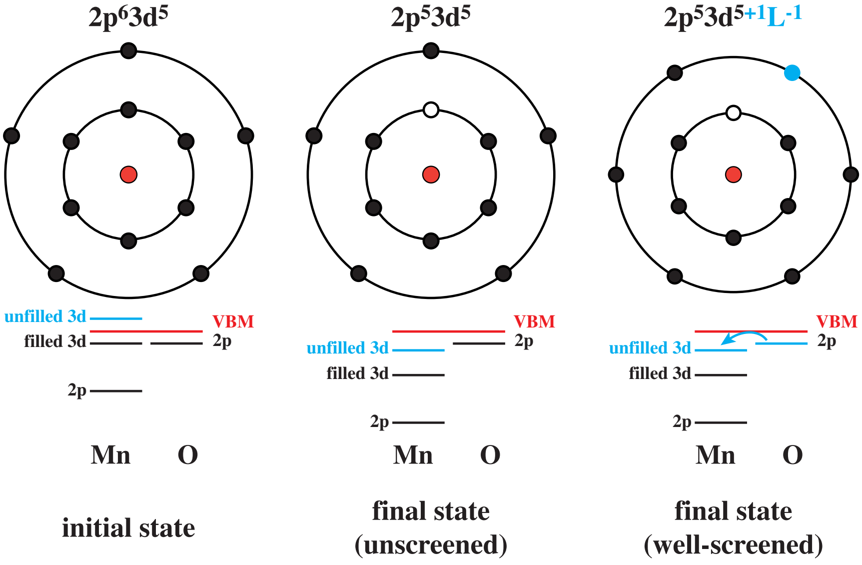

Figure 3.7: *Sketch of initial state, unscreened final state and well-screened final state of Mn in MnO. In the left picture, the initial state (before photoelectron excitation) is shown. The unfilled d-states are above the valence band maximum (VBM, red line). After the excitation, a core hole is left back in the 2p-shell. The energy levels are rearranged and the unfilled d-states slip below the VBM. However, no charge transfer from the oxygen states occurs. In the right panel, an electron has been transferred from the O states into the Mn 3d-states.*

However, this is not the only channel. The unscreened final state, where transfer does not occur, also exists and the overall spectrum is a superposition of both. The classification which peak corresponds to which final state is not trivial. The screening depends sensitively on the nature of the ligand, since the energetic positions of its core levels determine the energy gain due to the screening. A possibility to discriminate between the two final states is a comparison of various isoelectronic compounds, where the ligand is varied within one group (pnictides, chalcogenides, halogenides). The unscreened peak preserves its position (besides a chemical shift) upon substitution, whereas the well-screened peak shifts significantly.[106]

In the view of the upcoming results, it should be noted that for MnO, the lower binding energy side represents the *unscreened* final state, in contrast to the higher binding energy satellite, which is of *well-screened* nature.[106] The separation is approximately 6 eV.[118]

Table 3.2: *Initial state of Mn in MnO and the two possible final states after the excitation of a Mn 2p electron. First row: unscreened, second row: well-screened.*

initial state	final state
$2p^6d^5L$	$2p^5d^5L$
$2p^6d^5L$	$2p^5d^6L^{-1}$

The charge-transfer from a ligand is sometimes called *well-screened*, which has to be distinguished from *non-local screening*, where the screening is caused by conduction electrons. This last channel can be neglected here, since MnO, showing a CT satellite, is an insulator. The situation is schematically depicted in Fig. 3.7. The electron configuration for the specific case of MnO of the initial and the various final states is given in Tab. 3.2.

3.2.3 Multiplet splitting

A further final state effect which is particularly pronounced in transition metals and rare earths is the exchange splitting (also sometimes called multiplet splitting). If an ion has an unfilled outer shell, e.g., d- or f-orbitals, the hole created through photoionization can couple to the spin and orbital angular momentum of the unfilled shell and thereby produce satellites not present in the initial state.[111]

In view of the upcoming results, the simplest case of an s-orbital in a TM compound shall be discussed. Similar considerations can be made for p-states in TM and the s-, p-, and d-states in rare earths, however, the structures are much more complex and would further complicate the matter. In principle, an s core level should by a single, broad (owing to the lifetime of the photohole) line. However, the coupling of the spin of the remaining electron to the unfilled d-shell produces two lines. One (at lower binding energy) represents the state with parallel alignment of s- and d-spin, and the other (at higher binding energy), is the anti-parallel alignment. In line of this reasoning, the splitting between those two lines, which is in the eV-range, follows the Aufbau principle and should be a strong function of d-occupancy and be largest for a half-filled d-shell.

However, the situation is not as straight forward as it might seem. This model assumes the bonding to be entirely ionic. A covalent portion of the bonding would alter the d-count. The ionicity might hold for free atoms, halogenides, or oxides, but hardly for pnictides or even inter-metallic compounds.[119–121] Fortunately, this can be used in turn to give an estimation of the *effective* d-electron count.

A further drawback is the interference with other effects, which makes a precise determination of the exchange splitting challenging. The multiplet splitting is an *intra*-atomic effect. Only the overlap between the atomic s- and d-waves plays a vital role. The interaction is larger when the radial probability distributions have a larger overlap. Therefore, the multiplet splitting is also a function of principle quantum number, being larger for equal numbers and smaller for unequal ones (for $3d$-metals: $\Delta E_{3s} > \Delta E_{2s}$).[120] This effect can now interfere in the spectra with *inter*-atomic effects, which are of comparable magnitude and separation, namely charge transfer satellites (see previous section). Only a thorough analysis of the spectra can help to distinguish these two effects simultaneously present in the same spectrum.

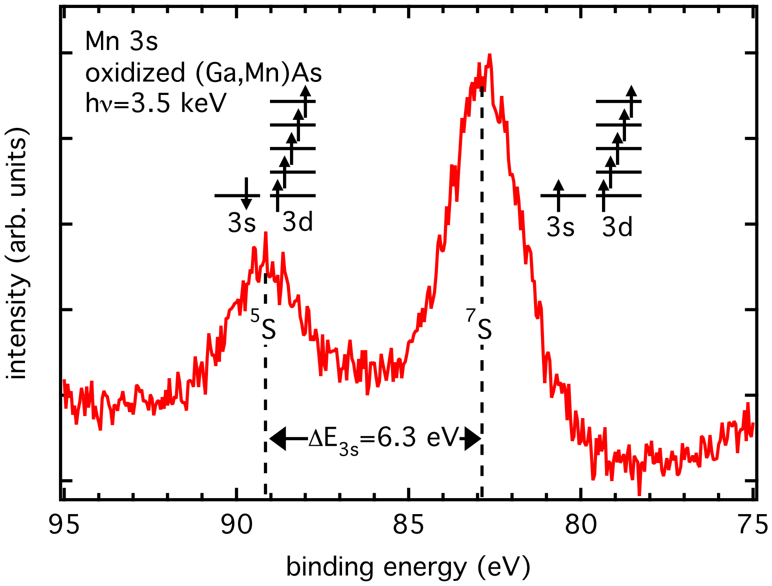

Figure 3.8: *Multiplet splitting of the Mn 3s core level in heavily oxidized (Ga,Mn)As. MnO can safely be expected to be the dominant species. The ^7S- and ^5S-states are clearly visible and are separated by 6.3 eV. For MnO it has been shown[118] that charge transfer is not observed in the 3s core level. Therefore, the splitting is exclusively due to multiplet splitting of the high-spin Mn $3d^5$ ($S = \frac{5}{2}$) configuration and the Mn $3s^1$-state. The splitting is in agreement with the value for the even more ionic MnF_2[120] and atomic Mn, which is naturally in $3d^5$ configuration.[119]*

Figure 3.8 shows a spectrum of the Mn $3s$ core level of a heavily oxidized (Ga,Mn)As sample recorded with 3.5 keV photons. Two peaks are observed with a splitting of 6.3 eV. This splitting can in principle be caused by charge-transfer or exchange splitting. The former case can, even though expected, be excluded for MnO. It has been shown that the core-hole–d-electron Coulomb attraction Q is too small for the Mn $3s$ in MnO to produce a sizeable charge-transfer satellite, in sharp contrast to the Mn $2p$ core level, where a pronounced satellite due to charge transfer is observed.[118] Hence, the splitting has to be exclusively due to multiplet splitting. In the case of MnO, if sufficient ionicity of the bonding is assumed, Mn is in $3d^5$-configuration and thus, the coupling of the Mn $3s$ core level is maximal. The two peaks can be assigned to a ^7S- and ^5S-state for parallel and antiparallel alignment of the remaining $3s$-spin to the $3d^5$-shell, respectively. The value is in agreement with the values for MnF_2[120] and atomic Mn.[119] The value of 6.3 eV is also one of the largest values for the splitting observed in $3d$-TM.[106]

3.2.4 Background corrections

Besides the features outlined in the previous sections, PES spectra have also a more or less structureless background (besides the individual peaks), the intensity of which increases to higher binding energies. This is mainly a consequence of secondary electrons, i.e., electrons losing kinetic energy by one or several loss mechanisms. In order to analyze core level peaks as accurate as possible this background has to be removed. The most simple approach would be to subtract a linear background. However, the error by such a simple analysis is too large, as shown, for instance, in Ref. 122. A much more sophisticated and widely used procedure is the so-called Shirley-correction.[123] Here it is assumed that the loss probability is constant, i.e., independent of energy. An example is shown in Fig. 3.9.

The red line gives the Ga $3d$ core level of a $Ga_{0.97}Mn_{0.03}As$ sample. The background at lower and higher binding energies of the main peak is clearly different. The black line gives the numerically calculated background according to Shirley.[123] After subtraction of the background from the initial spectrum, the blue curve is obtained. This corrected spectrum can now be used for further quantitative analysis. The inset of Fig. 3.9 gives enlarge the basis of the main centroid and shows the detailed shape of the Shriley-background. This step-like background eliminates the background at the higher binding energy side of the peak and line shapes become quite symmetric. This procedure is used in all spectra shown in this thesis unless stated otherwise.

However, also other procedures have been proposed. One remarkable approach is the procedure of Tougaard.[117] Here, not a constant energy loss-function is used as in the case of Shirley, but a model loss-function showing a plasmon peak. Therefore, at least one fine structures in the spectra is taken into account. This procedure is in particular powerful for substances where one plasmon dominates the spectrum. Therefore, it works quite well for simple metals,[117] however, especially semiconductors are not reproduced well.[124] A detailed knowledge of the true loss-function is desired, which also accounts for other fine structrues. In the case of GaAs, the data from Philipp and co-workers[112] or von Festenberg[113] can be used.

For the purpose of this study, such a detailed analysis of the background is not attempted. As a detailed investigation of satellite structures is not an issue in this work, a correction by means of a Shirley-background is assumed to be sufficient.

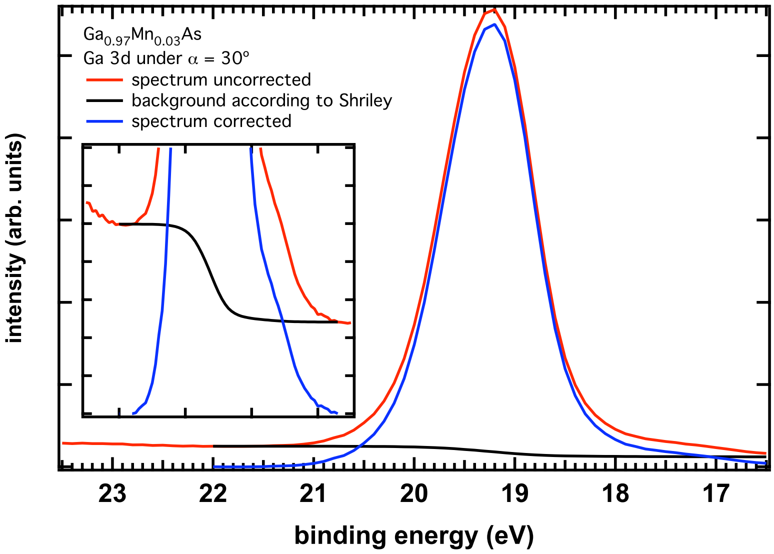

Figure 3.9: *Example of a Shirley-background correction; the red line shows the Ga 3d core level of a* $Ga_{0.97}Mn_{0.03}As$ *sample as measured. The black gives a numerical calculated background according to Shirley.*[123] *The blue line gives the corrected spectrum, which can then be used for further quantitative analysis.*

3.2.5 Qualitative and quantitative analysis of spectra

Regarding the problems and contributions to spectra described previously, the question arises if spectra can be analyzed qualitatively and quantitatively at all. As has been shown in previous sections, all characteristic loss features are present in GaAs. However, none of these effects are dominant. The error caused by disregarding even the features near the main centroid is small. This may not be valid for other materials or would need at least closer inspection, but it is surely acceptable for GaAs. In order to analyze spectra qualitatively, e.g., to determine the covering oxide layer or to identify different valences, the core level spectra have to be fitted. The intrinsic peak form of a core level is in general given by a Lorentz profile:

$$L(E) = \frac{I_0}{\pi} \frac{\Gamma/2}{(E_0 - E)^2 + (\Gamma/2)^2} \tag{3.6}$$

with I_0 the intensity, E_0 the location of the peak, and Γ the full width at half maximum (FWHM). The line width is given by the life time of the core hole. When writing the FWHM as $\Gamma = \hbar / \left(t_{1/2} \ln 2\right)$ the dependence on the life time of the photohole becomes obvious. This means that short-lived levels are broader than long-lived levels. The life time is largely determined by the orbital moment. In general, the life time gets longer in the order $s \rightarrow p \rightarrow d \rightarrow f$.[125] Thus, s-orbitals are relatively broad, whereas f-orbitals are comparably narrow. Determining absolute values for Γ is a delicate issue.[126] Care has to be taken to minimize all other possible sources of broadening (see below), which is in particular difficult in the x-ray regime due to the natural line width of the source. However, in the analysis of the data shown here, it was made sure to follow at least the trend of the orbital momenta.

In a realistic case, the intrinsic line width is not the only factor leading to broadening of the (in principal) δ-function-like core levels. Thus, core levels are fitted by a Voigt-function [Eq. (3.7)], which is a convolution of a Lorentzian and a Gaussian. Several other factors which lead to additional broadening from thermal, instrumental and phonon-interactional processes are included by the Gaussian (σ).[127]

$$V(E) = I_0 \frac{2\ln 2}{\pi^{3/2}} \frac{\Gamma}{\sigma^2} \int_{-\infty}^{\infty} \frac{e^{-t^2}}{\left(\sqrt{\ln 2}\Gamma/\sigma\right)^2 + \left(\sqrt{4\ln 2}(E-E_0)/\sigma - t\right)^2} dt \tag{3.7}$$

Especially transition metal $2p$ spectra show in general a quite complex peak form caused by the interaction of electrons from $2p$ and $3d$ core levels. The exchange splitting (*cf.* Sec. 3.2.3) is not entirely resolved but the envelope shows an asymmetric peak skewed to higher binding energies.

Furthermore, simple metals are known to show an asymmetric line shape with a long tail to higher binding energies. After the creation of electron-hole pairs by the photoeffect, the screening by valence electrons leads to this phenomenon.[107] In order to deal with these peak shapes, Doniach and Šunjić[128] gave an equation for a modified Lorentz-profile, taking a certain asymmetry into account. The equation for the peak reads:

$$DS(E) = I_0 \frac{\cos\left(\pi\frac{\alpha}{2} + (1-\alpha)\arctan\left(\frac{E-E_0}{\beta}\right)\right)}{[(E-E_0)^2 + \beta^2]^{(1-\alpha)/2}} \tag{3.8}$$

with the intensity I_0, the asymmetry α, the position of the maximum E_0, and the peak width β. As can be seen, the Doniach-Šunjić peak shape reduces to a Lorentz profile (3.6) for $\alpha \to 0$. β is to be identified with $\Gamma/2$. Interestingly, the asymmetry parameter α turns out to be equal for all core levels of one and the same element.

Equation (3.8) is a comparably simple equation but has the disadvantage that its integral diverges, which is of course unphysical. The more sophisticated equation by Mahan[129] does not diverge but is by far more complicated to handle. It turns out that Eq. (3.8) works just as fine as Mahan's equation and only slight differences are observed at the tails of the line.[116] Hence, when dealing with asymmetric peaks Eq. (3.8) is used. If required, additional broadening by a Gaussian as in Eq. (3.7) can also be included in Eq. (3.8).

Transferring the issue to the current problem, there is no need to apply Eq. (3.8) to the core levels of As and Ga, as the lines can be fitted by Eq. (3.7) equally well. Due to the fact that the gap in semiconductors suppresses electron-hole excitations in the valence band[111] and it is not free-electron-like around the Fermi energy, screening by such electrons is negligible in GaAs. In the case of the Mn $2p$ core level in (Ga,Mn)As, a fitting by a Doniach-Šunjić line shape would, in principle, be required. However, due to the low statistics for nearly all Mn spectra and other uncertainties, such as analyzer response function, a fit of the Mn $2p$-spectrum is not attempted. Fortunately, the shift between Mn species is either large enough (in the case of the oxide) to be seen at first glance or too small (in the case of Mn_{sub} and Mn_{int}) to be resolved at all. However, if XPS studies with higher resolution ($\Delta E \leq 0.3\,\text{eV}$) become available, a fit by Doniach-Šunjić profiles will be necessary to distinguish between the different Mn components embedded in the matrix.

If one is interested in the overall composition of the sample, a reliable quantitative analysis of the core levels is necessary. As will be shown later in more detail [Eq. (3.15)], the intensity of a core level is directly proportional to the amount of atoms of a specific element. Thus, in principle, the total amount of atoms should be determinable by the core level intensity. However, several other factors hamper such a naive interpretation. In order to calculate the amount of an element, knowledge of the photonflux, the photoionization cross section, the analyzer transmission function, and the detector efficiency is required. Most of these factors are unknown or can only be approximated. When taking the ratio of two core levels recorded with identical pass energy and under a constant photonflux, the problem is reduced to the knowledge of the cross section and the transmission function. Those two factors can not be neglected when analyzing different core levels, which are widely separated in energy. The analyzer transmission function depends on the analyzer used and can in most cases be approximated by a square root dependence on the kinetic energy: $T(E) \propto \sqrt{E}$. Even though this seems to be quite a crude approximation it is not the largest source of error. The photoionization cross sections are only known from calculations for free atoms and can thus lead to large deviations. It has been shown that the error by considering the free atom cross sections and neglecting the situation in a real solid can be up to 30 % in the ratio of two elements.[115] This is an unacceptable shortcoming, especially when dealing with contents in the diluted limit.

Therefore, another approach has been chosen. The ratios for core levels in (Ga,Mn)As have been calibrated to reference samples with defined stoichiometry. In the case of (Ga,Mn)As this is relatively easy since GaAs wafers are commercially available. The Mn content has been calibrated by a MnAs bulk sample.[130] Both samples were filed *in situ* in order to obtain a surface with correct stoichiometry. Sputtering, etching, or other microscopic surface preparation methods would again have biased the results in an unpredictable direction. Only large scale, chemically insensitive, removal of material provides a stoichiometric surface. In this way, the error bar was greatly reduced. For instance, an analysis of the Mn-to-As ratio of a MnAs sample by means of tabulated photoionization cross section gave a ratio of 0.56. The error bar was almost 100 %. By the calibration of the ratios only the uncertainty in the determination of the integrated intensity (background, integration limits, etc.) remained. Thus, an ample overall error bar of 10 % is assumed. Measurements of the reference samples have been conducted for all experimental setups (excitation energy, analyzer) and measurement specifications (pass energy, lens mode, etc.) in order to obtain experimentally determined sensitivity factors for all upcoming results.

Such a precise analysis of the stoichiometry within the probed depth was only possible due to the reference samples. If samples of known stoichiometry are not available, or their crystal structures are not comparable (GaAs and MnAs are quite alike), one cannot perform a quantitative analysis with such a precision. Ratios of the elements can then be seen only as ballpark numbers.

3.3 Inelastic mean free path, information depth and effective attenuation length

As already stated, PES is a surface sensitive measurement. Depending on the kinetic energy of the excited photoelectrons the probed depth is somewhere between a few Å and a few nm. The uncertainty of the probed depth has been the subject of intense studies ever since PES became a major technique of use. Several parameters can be given as a measure for the surface sensitivity of PES, whose definitions and theoretical calculations are given in this section.

3.3.1 Inelastic mean free path

Several important terms used throughout this thesis and in the literature on PES in general, require a precise definition. First of all, there is the so-called *inelastic mean free path* (IMFP). According to the ASTM Committee E-42 on Surface Analysis it is defined as *"the average distances, measured along the trajectories, that particles with a given energy travel between inelastic collisions in a substance."*[131] Inelastically scattered electrons contribute to spectra in several ways. First of all, they lead to a featureless background which increases with higher binding energy. Quantized excitations, especially plasmon excitations, have a defined energy and can also be identified in the spectrum. Their energy will be given later since it also occurs in most of the calculations of IMFPs. Further information on structures caused by inelastic scattering has been given in the previous section (Sec. 3.2).

According to its definition, the IMFP is a theoretical quantity. Calculations require the knowledge or approximation of the dielectric function. However, since the dielectric function is not known for all materials or simple approximations are too crude, several semiempirical expressions have been proposed over the last years in order to give quantitative values for the IMFP.[132] They have two major points in common. Firstly, they are easy to use and include only basic arithmetic functions. Secondly, they yield the IMFP on the basis of macroscopic quantities of the material under investigation. However, this is also their weakness. The equations are only semiempirical and lack a detailed theoretical foundation.

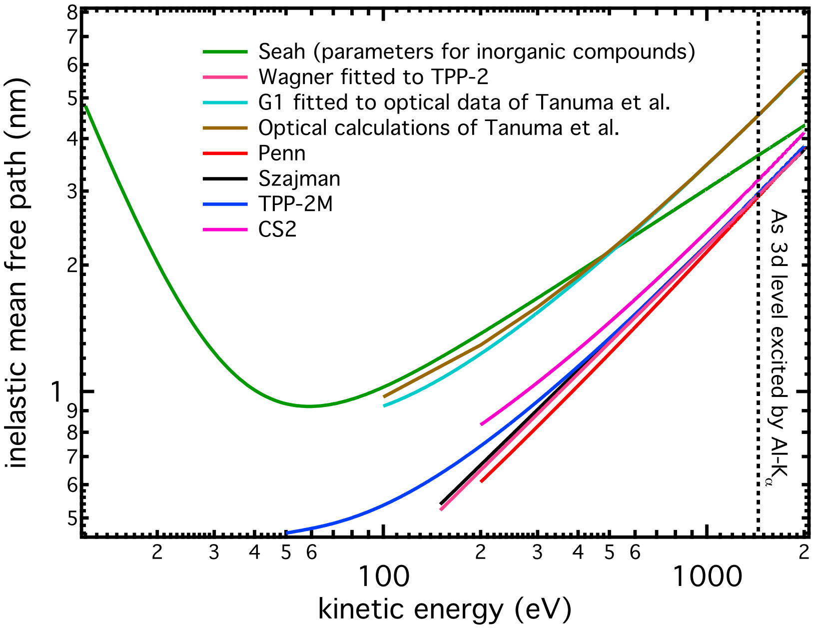

Figure 3.10: *Calculations of the IMFP in GaAs by various methods. The IMFP have been calculated according to Refs. 132 and Eq. (3.9).*

In the following, only the latest TPP-2M equation[133] and the CS2 equation[134] are described explicitly. IMFP values calculated by other formulae are only shown in Fig. 3.10 for comparison, whereas for the formalisms behind those values, the interested reader is referred to the literature.[132] The TPP-2M equation explicitly reads:[133]

$$\begin{aligned}
\lambda &= 0.1 \cdot \frac{E}{E_p^2[\beta \ln(\gamma E) - (C/E) + (D/E^2)]}\ [nm] \qquad (3.9)\\
E_p &= 28.8 \left(\frac{N_v \rho}{M}\right)^{1/2}\\
\beta &= -0.10 + 0.944(E_p^2 + E_g^2)^{-1/2} + 0.069\rho^{0.1}\\
\gamma &= 0.191\rho^{-1/2}\\
C &= 1.97 - 0.91U\\
D &= 53.4 - 20.8U\\
U &= N_v\rho/M
\end{aligned}$$

E is the kinetic energy of the photoelectrons, E_g the band gap energy for non-conductors, E_p the free-electron plasmon energy (see also Sec. 3.2.1), M is the atomic or molecular weight, N_v is the number of valence electrons per atom or molecule, and ρ is the density (in g/cm^3). The range of validity is between $50 - 2000\,$eV.

Table 3.3: *Parameters for the TPP-2M calculation using Eq. (3.9) and plotted in graph 3.10. Values from Refs. 9,135,136. (Despite intensive search no value for band gap of diarsenicpentoxide was found in the literature; since the amount of the pentoxide is comparable small and the trioxide is already insulating the value of the trioxide was also taken for the pentoxide.)*

	GaAs	As_2O_3	As_2O_5	Ga_2O_3
N_v	8	28	40	24
ρ (g/cm^3)	5.31	3.89	4.32	5.90
M (mu)	144.645	197.841	229.800	187.444
E_g (eV)	1.4	5.00	5.00	4.9
E_p (eV)	15.60	21.37	24.97	25.03
U	0.29	0.55	0.75	0.75
C	1.70	1.47	1.29	1.28
D	47.29	41.95	37.76	37.69
β	0.042	0.022	0.017	0.019
γ	0.083	0.097	0.092	0.079

This equation is based on the Bethe formula for the scattering of charged particles in matter.[137] Bethe's equation was set up for high energy particles (MeV range), but seems to hold for low kinetic energy particles as well.

Also related to the TPP-2M equation, and already anticipating Sec. 3.3.4, is the so-called CS2 equation of Cumpson and Seah.[134] It reads:

$$\lambda_{AL} = ka^r \left[\frac{E}{Z^{0.45} \left[\ln(E/27) + 3\right]} + d \right] \; [nm] \tag{3.10}$$

with the lattice parameter a, the atomic number Z, three adjustable parameters k, r, and d, and the kinetic energy of the photoelectrons E in eV. It gives the attenuation length (see Sec. 3.3.4) of photoelectrons in a certain matrix (characterized by the atomic number and the lattice parameter) with a given kinetic energy. The free variable allow an individual adjustment to optical data.

They proposed this formula as a convenient and easy-to-use equation for surface analysis by means of PES. In contrast to the TPP-2M equation, it is supposed to consider elastic scattering as well. Monte-Carlo simulations indeed showed greater accuracy and thus, it is being debated if the CS2 is to be used instead of the TPP-2M. With the fitting parameters $k = 0.316$, $r = 3/2$ and $d = 4$ in Eq. (3.10) the curve shows a standard deviation of 6 % to the calculated optical data in Ref. 133 for GaAs, which is a remarkable accuracy. For larger energies the CS2 shows the same dependence as the TPP-2M, asymptotic to the modified Bethe-equation.

The calculations in Fig. 3.10 are done for pure GaAs. The contribution of Mn is considered to be negligible owing to its low concentration. However, since oxides are always present on the surface and the analysis of the oxides is an essential part of this thesis, the dependence of the IMFP on the material composition is of high interest.

Figure 3.11 shows the TPP-2M calculations for all major oxides related to GaAs compared to pure GaAs. The parameters used in Eq. (3.9) are given in Tab. 3.3. Ga_2O_3 shows the shortest IMFP whereas the IMFPs of the arsenic oxides are comparable to the values of GaAs. This is important since the natural oxide layer of GaAs is Ga_2O_3-rich and the (average) IMFP of the overlayer will be used later in Eq. (3.19). The reason of the shorter IMFP for the gallium oxide is its high density and comparably large number of valence electrons. For simplicity, the average value of the IMFP in the oxide layer is the mean of the values for Ga_2O_3 and As_2O_3, weighted by their ratio in the oxide layer of 6 : 5 (see Sec. 3.3.5). This ratio was used in the forthcoming analysis.

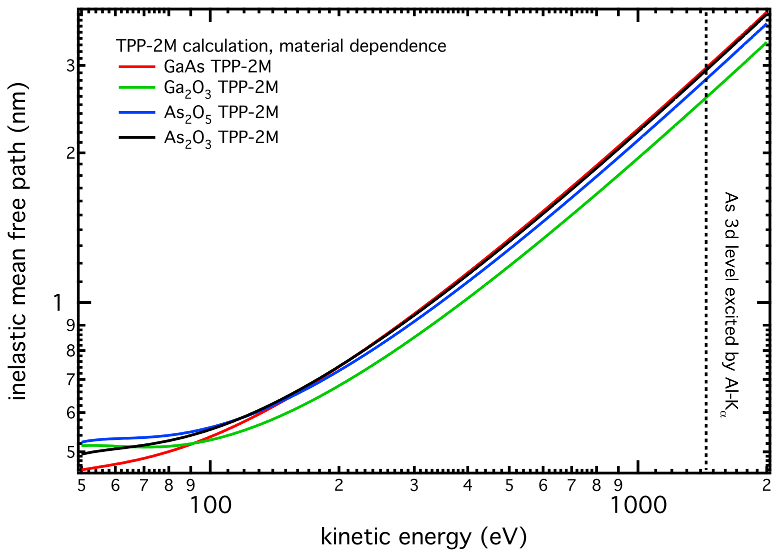

Figure 3.11: *Calculations of the IMFP using Eq. (3.9) for various compounds. The parameters used can be found in Tab. 3.3. In general, oxides show a smaller IMFP than pure GaAs. The differences for the arsenic oxides are minor but Ga_2O_3 shows a large discrepancy of* 0.35 nm *at a kinetic energy of* 1443 eV *(corresponding to electrons from the As 3d core level excited by Al K_α radiation). Exact values are given in Tab. 3.4.*

Nevertheless, both the TPP-2M and the CS2 equations have a great disadvantage. As stated above, they are only semiempirical approximations trying to determine the microscopic IMFP from macroscopic parameters. This gross simplification results in a large error bar when compared to calculated IMFPs considering the dielectric function. Especially for organic compounds,[133] and more importantly in the present case of GaAs, the discrepancies between TPP-2M results and optical data are huge. An error bar of ±30 % is exceeded in both cases. In the arguments of Tanuma *et al.* this is attributed to the uncertainty in the optical data. This may hold for more exotic and complex materials but not for one of the most studied materials in solid state physics, namely, GaAs. Thus, the IMFP values of the TPP-2M have to be handled with caution and are not to be seen to provide exact values. This is also valid for the CS2 equation. As will be shown later, values of the IMFP of (Ga,Mn)As obtained on the basis of the TPP-2M calculation give too small values for the oxide layer thickness compared to the literature. However, since it is the only equation being explicitly material specific, given IMFP values in this thesis are calculated by the TPP-2M equations unless stated otherwise.

Table 3.4: *Values for the IMFP (in nm) calculated by the TPP-2M equation [Eq. (3.9)] for photoelectrons from all core levels of interest at various excitation energies.*

		GaAs	As_2O_3	As_2O_5	Ga_2O_3
$h\nu = 640\,\text{eV}$	O $1s$ ($E_B = 543.1\,\text{eV}$)	0.53	0.55	0.56	0.50
	C $1s$ ($E_B = 284.2\,\text{eV}$)	1.07	1.05	1.02	0.90
	As $3d_{5/2}$ ($E_B = 41.7\,\text{eV}$)	1.53	1.51	1.46	1.27
	Ga $3d_{5/2}$ ($E_B = 18.7\,\text{eV}$)	1.57	1.55	1.50	1.30
	Valence band ($E_B \approx 1\,\text{eV}$)	1.61	1.58	1.53	1.33
$h\nu = 1486.6\,\text{eV}$	As $2p_{3/2}$ ($E_B = 1323.6\,\text{eV}$)	0.67	0.67	0.66	0.59
	Ga $2p_{3/2}$ ($E_B = 1116.4\,\text{eV}$)	1.10	1.08	1.05	0.92
	Mn $2p_{3/2}$ ($E_B = 638.7\,\text{eV}$)	1.98	1.95	1.88	1.63
	O $1s$ ($E_B = 543.1\,\text{eV}$)	2.15	2.11	2.04	1.76
	C $1s$ ($E_B = 284.2\,\text{eV}$)	2.59	2.54	2.45	2.12
	As $3d_{5/2}$ ($E_B = 41.7\,\text{eV}$)	2.98	2.94	2.83	2.44
	Ga $3d_{5/2}$ ($E_B = 18.7\,\text{eV}$)	3.02	2.97	2.87	2.47
$h\nu = 4500\,\text{eV}$	As $2p_{3/2}$ ($E_B = 1323.6\,\text{eV}$)	5.61	5.54	5.32	4.57
	Ga $2p_{3/2}$ ($E_B = 1116.4\,\text{eV}$)	5.91	5.83	5.61	4.81
	Mn $2p_{3/2}$ ($E_B = 638.7\,\text{eV}$)	6.59	6.50	6.25	5.36
	O $1s$ ($E_B = 543.1\,\text{eV}$)	6.72	6.64	6.38	5.47
	C $1s$ ($E_B = 284.2\,\text{eV}$)	7.08	6.99	6.72	5.76
	As $3d_{5/2}$ ($E_B = 41.7\,\text{eV}$)	7.42	7.33	7.04	6.03
	Ga $3d_{5/2}$ ($E_B = 18.7\,\text{eV}$)	7.45	7.36	7.07	6.06

3.3.2 Information depth

The limiting factor of the probed depth of PES is not the penetration depth of the x-rays (unless the effect of total external reflection is used).[138] The attenuation of x-rays in a solid is given by the simple law:

$$I(x) = I_0 \cdot e^{-\mu(E)x} \tag{3.11}$$

The intensity of the x-rays at a distance x in a material is exponentially damped by the linear absorption coefficient $\mu(E)$. Table 3.5 shows these coefficients for the materials under investigation and the used photon energies.[138,139]

Table 3.5: *Values for the linear absorption coefficient μ (μm^{-1}) of GaAs, As_2O_3, As_2O_5, and Ga_2O_3 at photon energies of 1486.6 eV and 4500 eV.*[139,140]

E_{ph} (eV)	GaAs	As_2O_3	As_2O_5	Ga_2O_3
1486.6	0.703	2.972	4.346	1.845
4500	11.494	34.024	50.024	23.539

As can be seen in the table, if the x-rays incident under a sufficiently large angle from the sample surface ($\vartheta \geq 5°$, fulfilled for all measurements presented herein) the x-ray penetration depth is much larger than the IMFP of the excited photoelectrons and thus, the IMFP is the limiting factor and a measure for the surface sensitivity of PES.

It can be assumed that the signal of photoelectrons is attenuated exponentially in the solid and the damping coefficient is the IMFP λ. The intensity from a depth z_0 is then:

$$I(z_0) = I_0 \cdot e^{-z_0/\lambda} \tag{3.12}$$

where I_0 denotes the intensity at $z = 0$, i.e., at the surface without damping. The mean escape depth (MED) is defined as the depth perpendicular to the surface at which the intensity decreases to a value of $\frac{1}{e} = 36.8\,\%$. Thus, with respect to Eq. (3.12) the mean escape depth is simply the IMFP multiplied by the cosine of the angle under which the electrons leave the solid (see Fig. 3.12):

$$MED = \lambda \cdot \cos\alpha \tag{3.13}$$

The information depth (or sometimes referred to as "probing depth") is the distance normal to the surface from which a specified percentage of not inelastically scattered electrons originates. A reasonable value would be 95 % of the overall intensity since a loss of 5 % of spectral information is assumed to be acceptable. Thus, the distance from

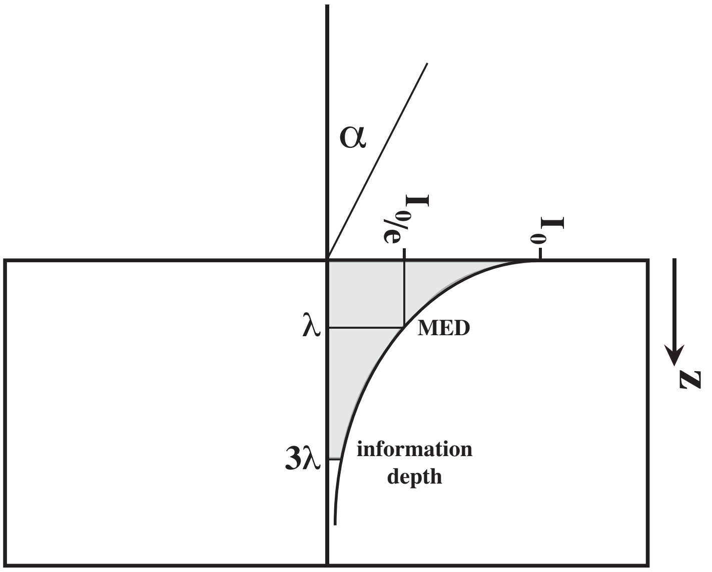

Figure 3.12: *Sketch of the mean escape depth and the information depth. If α is equal to 0 the MED is equal to the IMFP λ [see Eq. (3.13)]. The information depth is then equal to 3λ [Eq. (3.14)].*

the surface z_0 up to which 95 % of the overall intensity originates can easily be calculated by integrating Eq. (3.12):

$$\frac{\int_0^{z_0} I_0 e^{-z/\lambda} dz}{\int_0^{\infty} I_0 e^{-z/\lambda} dz} \overset{!}{=} 0.95 \;\Rightarrow\; z_0 \approx 3\lambda \tag{3.14}$$

In other words: only a layer of thickness $3\lambda \cos\alpha$ from the surface significantly contributes to the spectrum.

3.3.3 Overlayer thickness

The photoemission intensity I_0 depends on several parameters:

$$I_0 \propto F\sigma(E)\rho T(E) D(E) \tag{3.15}$$

namely, the photonflux F, the photoionization cross section $\sigma(E)$ of the core level of interest, the atomic density of the homogeneous material ρ (macroscopic density divided by atomic/molecular mass), the analyzer transmission function $T(E)$, and the detector efficiency $D(E)$. Most of these parameters are difficult to determine. However, when Eq. (3.12) is used to calculate an overlayer thickness most of these variables are canceled out.

If a homogeneous oxide layer of thickness d_{ox}, atomic density ρ_{ox}, and IMFP λ_{ox} covers a substrate of semi-infinite thickness, with atomic density ρ_{sub} and IMFP λ_{sub} (assuming a sharp interface) the spectral contributions from both layers can be calculated [α is the take-off angle as defined in Eq. (3.13) and Fig. 3.12]:[141]

$$\begin{aligned} I_{ox} &= \int_0^d F\sigma(E)\rho_{ox}T(E)D(E)e^{-z/(\lambda_{ox}\cos\alpha)}dz \qquad (3.16)\\ &= F\sigma(E)\rho_{ox}T(E)D(E)\lambda_{ox}\left(1-e^{-d/(\lambda_{ox}\cos\alpha)}\right)\\ I_{sub} &= \int_d^\infty F\sigma(E)\rho_{sub}T(E)D(E)e^{-(z-d)/(\lambda_{sub}\cos\alpha)}e^{-d/(\lambda_{ox}\cos\alpha)}dz \qquad (3.17)\\ &= F\sigma(E)\rho_{sub}T(E)D(E)\lambda_{sub}e^{-d/(\lambda_{ox}\cos\alpha)} \end{aligned}$$

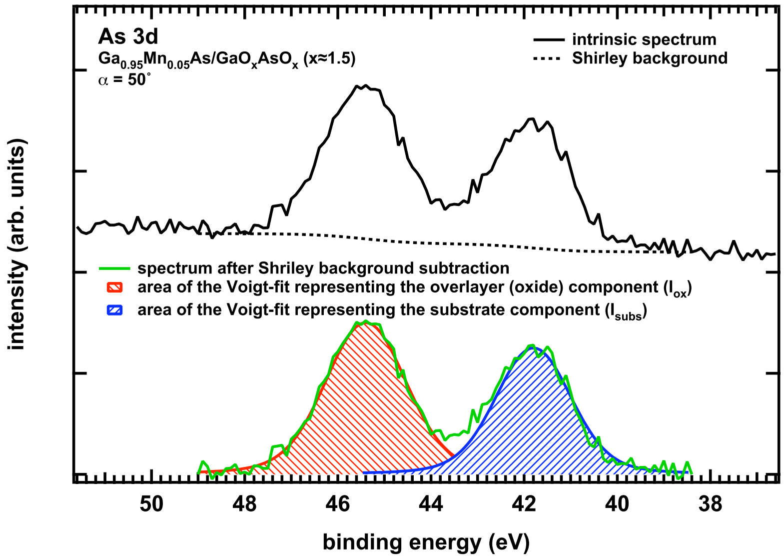

Figure 3.13: *Example of how information on the overlayer and substrate are determined from one and the same spectrum. The black line is the intrinsic spectrum as measured. The black dashed line is the Shirley background which was subtracted in order to eliminate the intensity from inelastically scattered photoelectrons. The resulting spectrum was fitted by two Voigt profiles and the area under each peak was taken as relative intensity of the corresponding component.*

The spectrum of an oxide usually shows a shift of the a core level to larger binding energies with respect to the element due to the different chemical environment.[142] The charge distribution of the valence shell is spatially rearranged. Due to the high electronegativity of oxygen, this effect is quite prominent for oxides and depends crucially on the oxidation state.[143] This chemical shift can be taken to obtain the intensities of both the overlayer and the substrate from one and the same spectrum of one core level (see Fig. 3.13). The energy dependent variables cross section, analyzer transmission, and detector efficiency can be assumed to equal for both species, since the energy shift is prominent (typical chemical shifts of oxides are in the eV-range), however, small in comparison to the absolute energy scale (hundreds of eV or even keV). Their variation with energy is therefore negligible and they are thus canceled out. In case of synchrotron experiments the variation of the photon flux as a function of time has to be taken into account. For laboratory light sources such as a x-ray tube the flux variations are negligible.

Dividing Eq. (3.17) by (3.16) gives:

$$\frac{I_{sub}}{I_{ox}} = \frac{\rho_{sub}\lambda_{sub}}{\rho_{ox}\lambda_{ox}} \frac{e^{-d/(\lambda_{ox}\cos\alpha)}}{1 - e^{-d/(\lambda_{ox}\cos\alpha)}} \tag{3.18}$$

Equation (3.18) can now be solved for the oxide layer thickness d_{ox}:[12]

$$d_{ox} = \lambda_{ox} \ln\left(\frac{\rho_{sub}\lambda_{sub}}{\rho_{ox}\lambda_{ox}} \frac{I_{ox}}{I_{sub}} + 1\right) \cos\alpha \tag{3.19}$$

The thickness of an oxide layer on a substrate can easily be calculated by Eq. (3.19). The intensities of the two species are obtained by fitting the core level spectrum, the take-off angle is known, and the densities are macroscopic parameters. Finally, the IMFP has to be known, i.e., calculated by one of the equations mentioned in Sec. 3.3.1. The energy dependence of the IMFP is very small in the energy window of interest, however, the material dependence is significant as can be seen in Fig. 3.11. Despite the objections mentioned in the previous section, the TPP-2M is used to calculate the IMFP if absolute values for the oxide layer thickness (in nm) are given.

Often Eq. (3.19) is further simplified by setting both the atomic density and the IMFP equal for oxide and substrate.[12] This practise is not used here. Instead, accurate values for the density and the IMFP are considered.

3.3.4 Attenuation length

The IMFP as defined in Sec. 3.3.1 and used in Sec. 3.3.2 is a theoretical quantity. In experiments, the attenuation of a substrate signal by an overlayer was mostly determined by so-called overgrowth experiments.[143] However, most of the early results were probably affected by a comparably large error, since the overlayer morphology was not confirmed by microscopic methods. Thus, island-growth and incomplete coverage of the substrate are likely to have altered the results in a dramatic way.

In order to obtain an experimental quantity, a new parameter was introduced, the so-called attenuation length AL [or better: effective attenuation length (EAL)]. The literature gives controversial definitions on the EAL. According to Powell,[144] the EAL is: *"the average distance (in nanometers) that an electron with a given energy travels between successive inelastic collisions as derived from a particular model in which elastic electron scattering is assumed to be insignificant."* By this definition, the EAL is not different from the IMFP, except that it is a quantity to be determined by experiments. Later, the ASTM E-42 Committee stated the opposite, explicitly including elastic scattering.[131] For obvious reasons, the latter definition is assumed to be valid.

Elastic scattering is actually the reason why the EAL deviates significantly (±30 %) from the IMFP.[145] However, besides the empirical CS2 equation [Eq.(3.10)] the effective attenuation length, if not reliably measured, has to be determined taking elastic scattering explicitly into account. This requires thorough calculations of the transport properties of the solid.[146] Easy-to-use equations are not available, which makes the inclusion of elastic scattering effects into routine analysis procedures cumbersome. They are thus excluded in the upcoming analysis. One has to be well aware of this simplification. However, since overlayer thicknesses are mainly only discussed relatively (increase or decrease upon various surface treatments) and all measurements are conducted under geometrical conditions in which elastic scattering can safely be ignored, this simplified approach satisfies the desired accuracy.

Nevertheless, as a detailed knowledge of the probed depth [λ in Eq. (3.14) is to be replaced by the EAL] is essential for qualitative and quantitative studies by means of PES, the various simplifications done earlier have to be tested, which is done in the rest of this paragraph. Hitherto, the model of photoemission and signal dependence tacitly assumed [see Fig. 3.14 (a)]:

- an ideal (atomically) flat surface
- an overlayer with defined stoichiometry and sharp interface to the substrate
- an infinitely small solid angle of acceptance of the photoelectron analyzer
- the detection of electrons only along straight trajectory, i.e., neglecting elastic scattering events which change the direction of the photoelectron (straight line approximation, SLA)

Hence, these simplifications are disregarding several important processes. In order to estimate their effects, they will be addressed in the following. The major neglected points in Secs. 3.3.2 and 3.3.3 are [see Fig. 3.14 (b)]:

- surface roughness and electron backscattering at the surface
- photoelectron refraction and diffraction
- inhomogeneous overlayer composition
- finite solid angle of analyzer acceptance
- elastic scattering

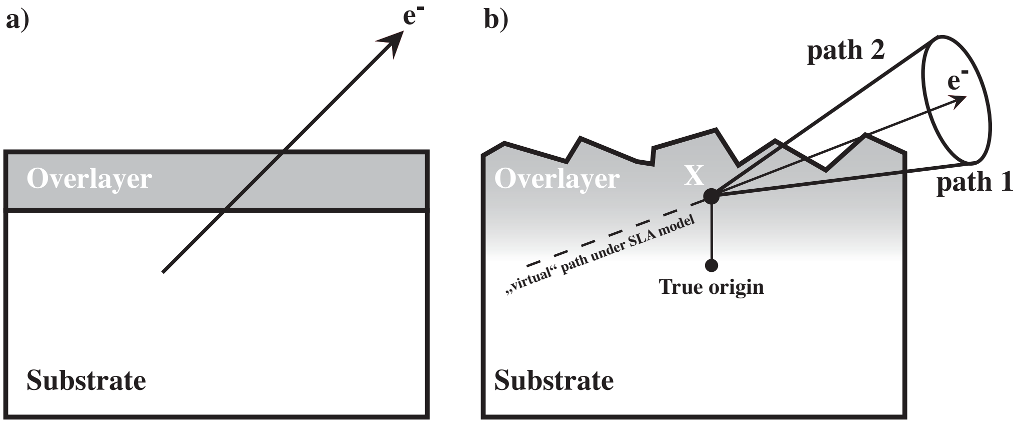

Figure 3.14: *Sketch (a) shows the simplified case: an ideal flat surface, a homogeneous overlayer with a sharp separation to the substrate, an infinitely small acceptance angle. The electrons travel only along rectilinear lines [straight line approximation (SLA)]. Figure (b) gives a more realistic pictures: the surface has a certain roughness, the overlayer has no defined composition but changes with distance from the surface and gradually fades into the substrate, the analyzer has a solid acceptance angle depending on the lens mode settings, and elastic scattering processes (indicated by the point X) take place.*

Not surprisingly, some of these points have crucial effects on the quantitative information derived from the spectra. The surface roughness, for instance, becomes particularly important for larger emission angles. In this case, so-called shading may occur. Parts of the surface are hidden in one direction by surface structures. Pronounced effects have been reported in the literature.[147] Since all samples measured in the course of this thesis were grown by MBE, and even intentionally oxidized and etched samples (as described later) showed a reasonably small surface roughness, this effect is assumed to be negligible. It should be noted, that under certain circumstances a periodic (or pseudo-periodic) surface texture can even lead to a cancellation of this effect.[148] A rough surface can also lead to enhanced backscattering of photoelectrons into the bulk. But even for flat surfaces refraction can play a vital role.

Table 3.6 shows the inner potential of the systems under investigation as well as their optical refraction index at a photon energy of 1486.6 eV. As the refraction index is essential unity and the light spot is usually larger than the analyzed spot (at least in a laboratory experiment), refraction of the light is irrelevant.

Conversely, the photoelectron is also refracted at the inner potential Φ_0 between the solid and the vacuum. This is nothing else than the well-known single step problem in quantum mechanics. The step leads to scattering and a loss of directional information. The refraction follows the simple equation:[153]

$$\alpha = \arctan\left\{\frac{\sqrt{\cos^2\alpha' - \Phi_0/E_{kin}}}{\sin\alpha'}\right\} \tag{3.20}$$

Table 3.6: *Refraction properties of GaAs, Si, and Ge; the value for oxidized GaAs is taken from Ref. 149 since Gajdardziska-Josifovska* et al. *assume this value to be affected by surface contaminations, but other values were not found in the literature despite intensive search.*

	Inner potential Φ_0 (V)	optical refraction index n (at 1486.6 eV)[e]
GaAs	14.53 ± 0.17^a	0.99998
GaAs_{ox}	13.2 ± 0.6^b	0.99983
Si	12.1 ± 1.3^c	0.99996
Si_{ox}	10.1 ± 0.6^c	0.99981
Ge	15.50 ± 0.44^d	0.99993
Ge_{ox}	9.10 ± 0.42^d	0.99989

[a]: from Ref. 150; [b]: from Ref. 149; [c]: from Ref. 151; [d]: from Ref. 152

[e]: calculated from Refs. 139,140

with the detection angle relative to the sample surface normal α, the real angle of motion in the solid α', the inner potential Φ_0, and the kinetic energy E_{kin}. A plot of the difference between detected angle α and the "real" angle of motion α' is shown in Fig. 3.15.

The refraction leads to a seemingly larger angle of detection, thus affecting the information depth. However, since the kinetic energy of the interesting core levels is rather large, the effect is not dominant. For core levels with high binding energy, i.e., low kinetic energy, this effect determined by the fraction Φ_0/E_{kin} in Eq. (3.20) becomes critical and refraction can lead to a severe change in the information depth.

In a single crystal, some trajectories of the photoelectrons are more favorable than others. The attenuation of the photoelectrons by scattering is lower for certain crystallographical directions and the detected signal thereby larger or the probing depth deeper. Since the natural oxide grown on a semiconductor is amorphous, this effect is henceforth not accounted for. Possible effects from the DMS layer below are likely to be smeared out by the overlayer. In the case of clean surfaces, spectra taken under various detection angles did not show any significant variation in relative intensities and thus, the effect of photodiffraction is also neglected.

Taking a naturally grown oxide layer on a semiconductor the assumption of a defined overlayer with a sharp interface to the un-oxidized substrate is not fulfilled. The natural oxide grows irregularly into the substrate and even the stoichiometry is inhomogeneous (*cf.* Sec. 2.1.2). The major oxides are the sesquioxides, As_2O_3 and Ga_2O_3, but also other oxides can be present, such as As_2O_5, $GaAsO_4$, or Ga_2O. Fortunately, the chemical shifts for any oxide, especially in the case of arsenic, are large enough to separate the entire

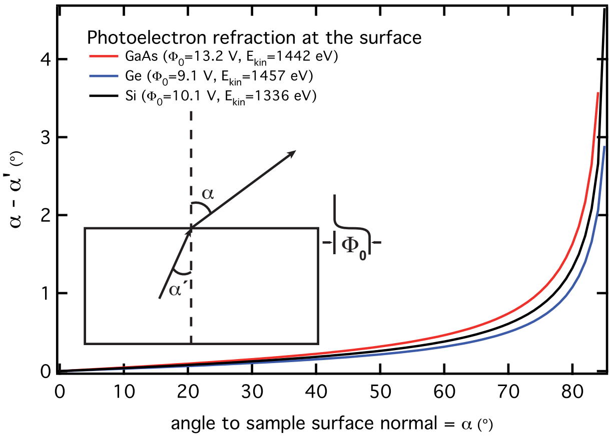

Figure 3.15: *Refraction of the photoelectron at the inner potential of a solid at the interface to the vacuum; the effect becomes apparent under grazing emission. However, owing to the large kinetic energy of the photoelectrons under investigation in comparison to the inner potential (refraction* $\propto \Phi_0/E_{kin}$*), the shift in detection angle* $\alpha - \alpha'$ *is not dominant even for* $\alpha = 80^\circ$ *(in particular not for germanium).*

oxide contribution from the intrinsic (substrate) contribution, and Eq. (3.19) is still applicable.

Moreover, a photoelectron analyzer does not have an infinite small acceptance angle but an angle acceptance of a few degrees (depending on the lens mode chosen), typically $\Delta\alpha = \pm 6^\circ$. Therefore, photoelectrons traveling along path 1 in Fig. 3.14 (b) have a longer way until they leave the surface than electrons following path 2. The prolonged trajectory in the solid depends on the angle of acceptance α and increases by increasing α. However, this dependence is not linear and can have a significant effect on the spectra by reducing the spectral contribution from the surface layer due to increased inelastic scattering (path 1 in Fig. 3.14).

Beside photoelectron diffraction, which is also an effect of elastic scattering, the argumentation above assumed the trajectory of the photoelectrons to be a straight line [straight line approximation (SLA)]. Only inelastic scattering was considered. Besides that electrons can also be scattered elastically. Therein, a scattering event does not lead to a loss in energy, but to a change in direction. According to the literature, elastic scattering is assumed to be the major effect on the EAL by influencing the angular distribution of photoelectrons and the information depth.

3.3.5 Experimental case study of inhomogeneous depth distribution and elastic scattering

In order to test and quantify the effects described above and extending the issue on elastic scattering, a detailed angle dependent case study of (Ga,Mn)As and other materials has been conducted.

(Ga,Mn)As

Panels (a) and (b) of Fig. 3.16 show a set of As and Ga 3d core level spectra recorded by a laboratory Al K_α light source. The increase of each oxide component on the high binding energy side by increasing the polar angle α is obvious and in agreement with the increasing surface sensitivity according to Eq. (3.13). A more detailed analysis of the data by means of Eq. (3.19), however, reveals a different behavior. In panel (c) the reduced oxide layer thickness d_{ox}/λ_{ox}, separately for As and Ga, is given. This conversion from the absolute oxide layer thickness in Eq. (3.19) to the reduced oxide layer has the advantage, that some uncertainty in d is cancelled out (λ_{ox} cancels). The reduced oxide layer thicknesses show an increase from 0° to approximately 60°, followed by a sharp decrease to larger angles. Furthermore, the values for Ga are throughout higher than for As.

This behavior is in sharp contrast to Eq. (3.19), which would predict constant values. Furthermore, the values for As and Ga should be equal. The latter effect is accredited to the aforementioned Ga-rich oxide layer. As described in Sec. 2.1.2 the natural oxide layer of GaAs is Ga-rich due to the preferential oxidation of Ga and a resulting segregation of Ga into the near-surface region. The remaining As forms an As^0 (elemental As) rich layer at the interface to the bulk GaAs. Not only the results in Fig. 3.16 (c) but also the results on etched samples presented later support this model. The Ga-related oxide layer is approximately 20 % thicker than the As-related. This point is important since the calculation of an IMFP of the oxide layer requires a value for the composition and thus this value will be used later ($\rho_{eff} = 4.99\,\mathrm{g/cm^3}$, $\lambda_{As\,3d,eff} = 2.711\,\mathrm{nm}$ and $\lambda_{Ga\,3d,eff} = 2.747\,\mathrm{nm}$).

The increase of the reduced oxide layer thickness from 0° to 60° is attributed to a significant concentration gradient of the oxides, especially at the interface.[154] This is not surprising, since the natural oxide layer is not expected to be homogeneous or to show a sharp interface to the substrate. It can be safely excluded that the effects of elastic scattering are dominant in this region, since it has been shown theoretically that although the EAL differs from the IMFP for smaller emission angles, the ratio of EAL to IMFP is constant for $\alpha \leq 60°$.[146]

The location of the maximum (in the present case at $\alpha = 60°$) depends on several factors. First of all, a rough surface leads to a shift to smaller angles.[154] Secondly, a larger angle between light source and analyzer results in an earlier decrease of the curve.[145] In the present case, the analyzer and the laboratory light source have an angle of 80°, which leads to the maximum at 60°. The absolute thickness of the overlayer also influences the drop of the curve, since the probability of elastic scattering is enhanced for thicker oxide layers.

For the decrease of d_{ox}/λ_{ox} beyond 60° several mechanisms can be made responsible for. First of all, the solid angle of acceptance of the photoelectron analyzer. The results presented here were taken with an angle acceptance of $\Delta\alpha = \pm 6°$. However, according to the literature such a value is not supposed to be the major cause leading to an un-

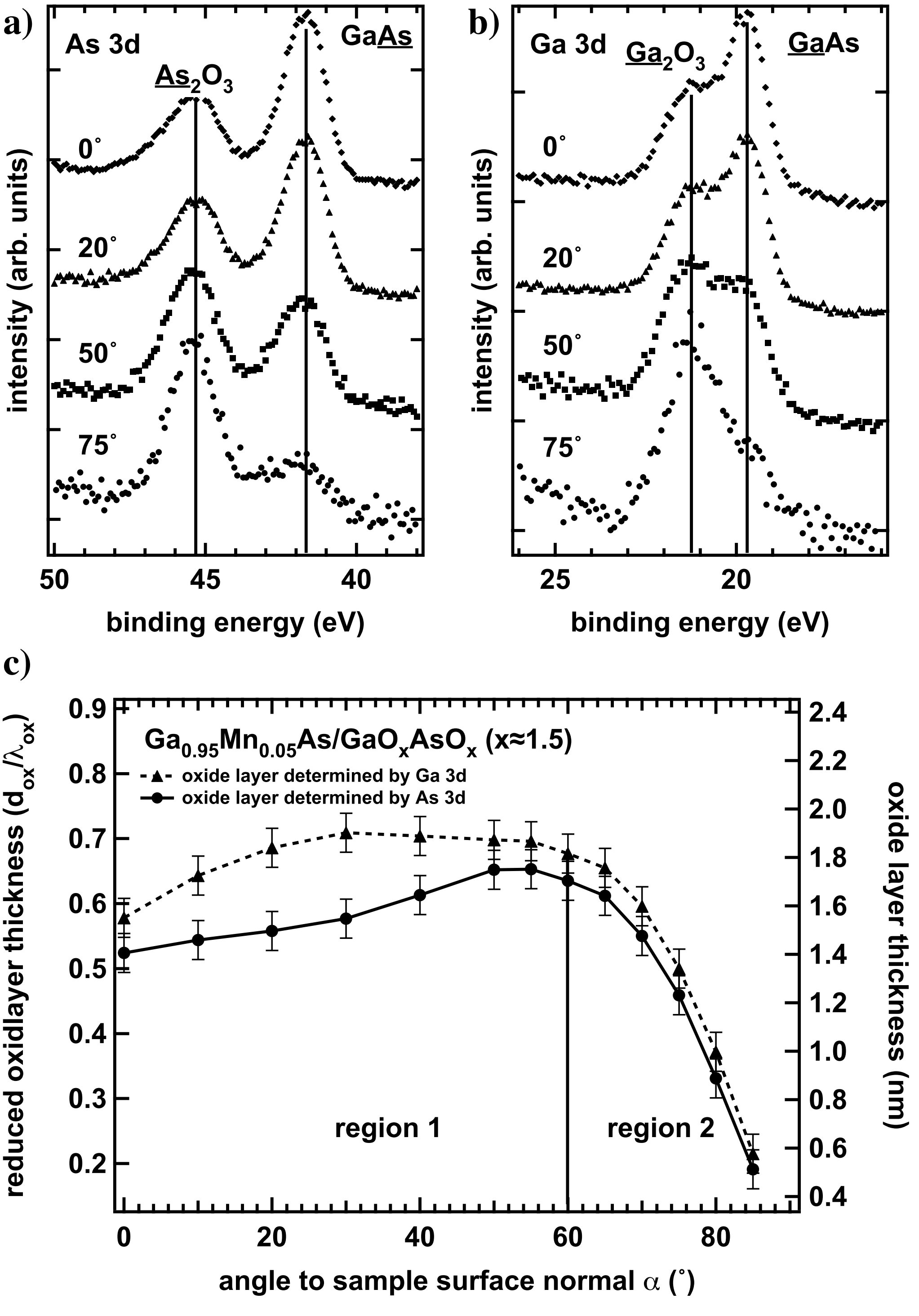

Figure 3.16: *Panels (a) and (b) show a set of As and Ga 3d core level spectra detected under various emission angles α. The increase of the corresponding oxide component on the high binding energy side is obvious. Panel (c) shows the reduced oxide layer thickness d_{ox}/λ_{ox} depending on the emission angle α as determined by Eq. (3.19) for As and Ga separately.*

derestimation of the oxide layer thickness.[155,156] Therefore, elastic scattering is thought to be the most pronounced effect leading to a decrease of d_{ox}/λ_{ox}.[157] While traveling through the solid after the excitation, photoelectrons can be scattered elastically at the Coulomb-potential of the matrix atoms leading to a change of the propagation direction. This effect is always present in any spectrum, but under grazing emission conditions it becomes significant. Unfortunately, the literature lacks an explanation, why grazing emission conditions lead to a pronounced occurrence of this effect.

Nevertheless, the consequences of elastic scattering are obvious. According to the cosine in Eq. (3.13) the path of the photoelectrons is prolonged such that most of the electrons traveling in a straight line can be assumed to be inelastically scattered. However, electrons undergoing elastic scattering can originate from a deeper layer of the solid without traveling the distance the straight line approximation (SLA) would suggest [see Fig. 3.14 (b)]. Thus, the SLA, and the assumption that the photoelectron signal decays exponentially fail.

In order to quantify the contributions of elastically scattered electrons to the spectra extensive Monte-Carlo simulations or transport calculations are required,[145,157,158] which are beyond the scope of the current investigation. However, one should be aware of the effects elastic scattering has on spectra because results can largely be affected by these effects. Especially under grazing emission conditions, systems with thick overlayers, and for samples containing elements with large atomic numbers, e.g., gold, platinum or $4f$-elements, elastic scattering is considered to be non-negligible.

Further consequences were reported on the angular distribution of the photoelectrons. The angular distribution of photoelectrons from a certain core level is given by the energy- and subshell-dependent asymmetry parameter β.[159] The deflection of the photoelectrons by elastic scattering requires the definition of a effective effective β in order to account for such effects.[160,161]

In general, equations (3.13), (3.14) and (3.19) are no longer valid in the cases, where elastic scattering becomes significant, since an exponential intensity decay cannot be assumed anymore. The calculated overlayer thicknesses may no longer be true and one should consider other values such as those given in Ref. 134.

Si/SiO$_2$ and Ge/GeO$_2$

To further concretize and verify the above conclusions, a complementary study was conducted on Si/SiO$_2$ and Ge/GeO$_2$. The issues are to compare the effects of naturally and deliberately grown oxide layers,[163] the effects of nuclear charge (and by that the deflecting Coulomb potential of the core electrons), and influences of the orbital quantum number (determining the asymmetry factor β). The results are given in Fig. 3.17. A comparison between Ge and Si addresses the atomic weight and β-dependence. Results on room-temperature-oxidized (RTO) and deliberately oxidized Ge deal with the oxide layer thickness dependence, and spectra recorded under different lens modes account for

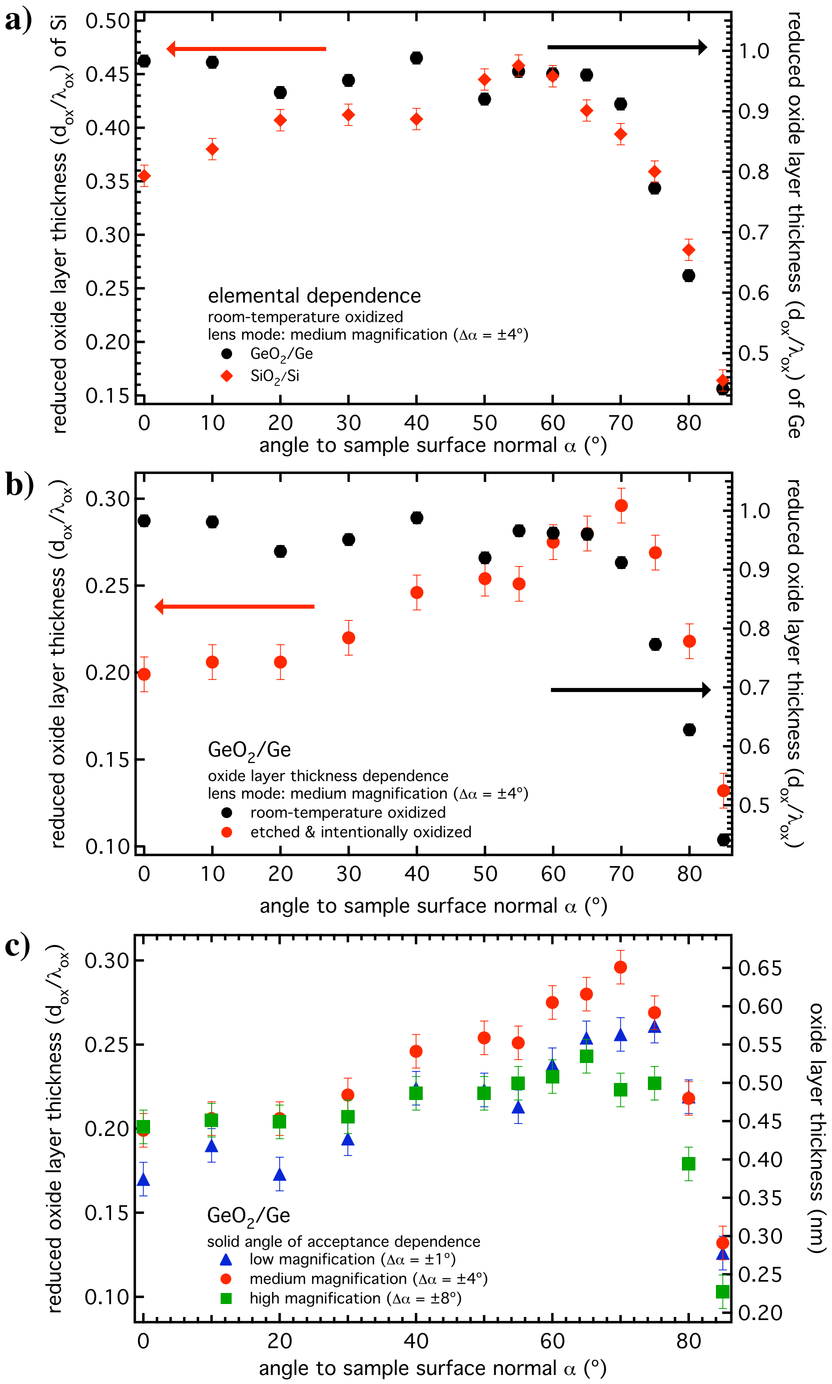

Figure 3.17: *Comparison of the reduced oxide layer thickness d_{ox}/λ_{ox} for different conditions:*
Panel (a): RTO silicon and germanium; the left ordinate gives values for silicon, whereas the right ordinate is for germanium;
Panel (b): RTO and intentionally oxidized germanium; the left ordinate gives values for intentionally oxidized Ge, the right ordinate is for RTO germanium;
Panel (c): intentionally oxidized germanium recorded with various lens modes (solid angle of acceptance); low ($\Delta\alpha = \pm 1°$), medium ($\Delta\alpha = \pm 4°$), and high ($\Delta\alpha = \pm 8°$).

Table 3.7: *Macroscopic physical parameters and IMFP for Si and Ge determined by Eq. (3.9). Values from Refs. 9,162.*

	N_v	ρ (macro. density) (g/cm^3)	M (u)	E_g (eV)	E_{kin} (eV)	λ (nm)
Si	4	2.33	28.086	1.12	1335	3.00
SiO_2	16	2.27^a	60.084	9.00	1335	3.76
Ge	4	5.32	72.610	0.66	1457	2.99
GeO_2	16	4.23	104.608	5.56	1457	2.89

[a]: value for amorphous quartz

the solid angle of acceptance effects (see Tab. 3.8). The latter two were performed only on Ge since it is in-between Ga and As in the periodic table (atomic weight) and its $3d$-orbitals have a comparable β-factor (Ga: 1.002, Ge: 1.031, and As: 1.055).[159]

The conducted experiments shown in Fig. 3.17 lead to the following picture: First of all, the atomic number and the asymmetry factor β seem to play no crucial role at all. Even though the differences between Si and Ge are huge ($\beta_{Si\,2s} = 2$ and $\beta_{Ge\,3d} = 1.031$;[159] $m_{Si} = 28.086\,u$ and $m_{Ge} = 72.61\,u$) the variations in Fig. 3.17 (a) are mainly due to the fact that RTO Ge exhibits a thicker natural oxide layer than Si. Thus, in case of Si, the slope of the reduced oxide layer thickness is attributed to the inhomogeneous interface, contributing more to the spectra than in the case of germanium. This is further supported by the comparison of the two different oxide layers for Ge in Fig. 3.17 (b) and is in accordance to Ref. 154. In particular, a renormalization of β as proposed by Ebel and co-workers[160] seems obsolete for the present study. The authors of Ref. 160 give an equation for the effective asymmetric factor depending on the nuclear charge reading:

$$\beta^* = (1.0688 - 0.0235Z + 0.000188Z^2)\beta.$$

This would give values of $\beta^*_{Si2s} = 1.55$ and $\beta^*_{Ge3d} = 0.525$. Neither this nor an increase of elastic scattering with increasing β can be seen in the data presented in Fig. 3.17 (a) and (b). However, a general absence cannot be excluded. It might be that an even more detailed study may show deviations.

A dependence on the solid angle of acceptance is only observed for the largest angle within this study ($\Delta\alpha \pm 8°$). The spectrum recorded with magnification "high" shows almost no slope since the effects of the inhomogeneous interface are obviously smeared out in the wider probing cone of the analyzer. An earlier drop of the curve for high magnification in Fig. 3.17 (c) as stated by Jablonski *et al.*[156] and Ebel and co-workers[155] is not observed. Spectra recorded with a narrower acceptance cone, however, show a higher sensitivity to the interface, and layer thicknesses recorded under various α differ significantly by up to 50 % in the present study.

Table 3.8: *Lens mode characteristics for the Omicron EA125 analyzer used to investigate the solid angle dependence of the calculated oxide layer thickness. The measurements shown below have been performed with a pass energy of $E_{pass} = 50\,eV$ (energy resolution: $\Delta E = 0.6\,eV$), an entrance slit of 90° (1 mm ⌀ aperture) and exit slit 2 (3 mm × 10 mm aperture).*

	magnification	analyzed area ⌀ (mm)	angle acceptance °
high	×5	0.2	±8
medium	×2	0.5	±4
low	×1	1.0	±1

One thing is apparent in all spectra, though: the reduced oxide layer thickness d_{ox} drops dramatically for values of $\alpha \geq 70°$. This drop is independent from the material under investigation, degree of oxidation of the surface, and solid angle of acceptance. Elastic scattering of photoelectrons from the un-oxidized substrate obviously contributes to the spectra in a dramatic way. Even for RTO germanium and under largest α, an intrinsic line is still detectable. The SLA would suggest a mean escape depth of 11.5λ at $\alpha = 85°$, which should lead to a damping of the intrinsic signal below the detection limit. Nevertheless, as Fig. 3.16 already implies, a weak but discernible signal from the bulk survives.

For reasons of completeness it has to be stated that the dependence of d_{ox} on the angle between light source and analyzer[164] was not tested in the present study. This would be rather troublesome to accomplish since movable light source and/or analyzers are seldomly available. Furthermore, an exemplary study of oxide layers with various experimental settings did not show significant alternations of the results as a function of the setup.[122] Therefore, this issue is considered to be of minor importance in common settings (i.e., analyzer and light source facing the same sample plane).

According to the results presented above, the following guide lines can be given in order to minimize errors occurring in angular resolved x-ray photoemission spectroscopy (ARXPES): Firstly, ARXPES should be performed in a narrow range of angles not exceeding—let's say—60° relative to the sample normal. Spectra taken under normal emission ($\alpha = 0$) are assumed to be most reliable according to the literature. This is simply due to the fact that under normal emission the probing depth is largest. One therefore averages over the largest depth possible and the mean oxide layer determined from Eq. (3.19) is sufficiently valid. The necessity for equal orbital quantum numbers of the elements under analysis and a not to wide range of atomic masses could not be confirmed in the present study. In contrast to that, the overlayer morphology and composition play a crucial role and therefore, should be known as precisely as possible. Additionally, the results presented above suggest to measure with an $\Delta\alpha$ as large as possible to smear out both the effects of photodiffraction and inhomogeneous composition. A slight angular dependence was observed, but not as large as suggested by the literature. Medium angle acceptances ($\Delta\alpha \approx \pm 5°$) seem to be a reasonable lower limit. Finally, calculated IMFP and information depth values are not to be seen as the ultimate truth and to be valid under all circumstances. Relative values are far less affected by errors than absolute ones. Especially, when microscopic investigations such as transmission electron microscopy (TEM) are not available, reference measurements on standards under identical conditions help to normalize the data and enhance the credibility of the results.[122]

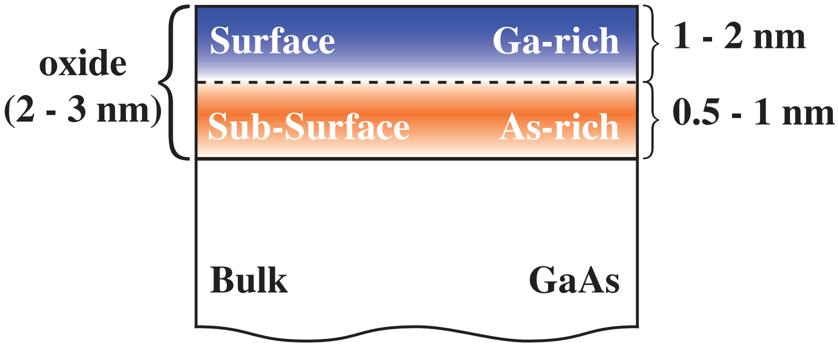

Figure 3.18: *Chemical composition of the $Ga_{1-x}Mn_xAs$ surface; the outermost layers are Ga enriched due to the preferential oxidation of Ga. The subsurface layer is left As-rich. By going deeper into the bulk the composition reaches the nominal stoichiometry of* $1:1$.

Turning back to the issues of characterizing the surfaces of GaAs and (Ga,Mn)As, a Ga-rich oxide layer was observed. Ga shows a larger reduced oxide layer thickness for any detection angle. The higher Ga content is also detected in the $As_{overall}/Ga_{overall}$ ratio, which was determined over the entire angle range from the overall (oxide + intrinsic signal) content, calibrated by the experimentally determined As/Ga intensity of a pure (*in situ* filed) GaAs sample. It is worth noting that the effects of elastic scattering are also present in the overall As/Ga ratio. A Ga-rich oxide layer would suggest that As/Ga decreases with increasing α, being close to zero for $\alpha = 85°$. However, the ratio shows, within statistics, an almost constant value. This proofs again the breakdown of the SLA, since it can only be explained by elastic scattering of the As-signal from deeper layers. Figure 3.18 visualizes the complex composition of the surface, sub-surface, and bulk regions. It is safe to say that the same model holds for pure LT-GaAs since the effects of Mn are, as already stated, negligible.

4 Surface preparation of (Ga,Mn)As

4.1 Effects of tempering on (Ga,Mn)As

This section addresses the effects of tempering on the oxide layer, contaminations, and the stoichiometry of (Ga,Mn)As. In the context of this thesis, the phrase tempering has strictly to be separated from the routine of annealing. The former deals with the effect of thermal treatment *in situ* to either clean the sample or to recover the surface from sputtering. The latter refers to the improvement of the physical properties of (Ga,Mn)As such as conductivity and magnetism after growth by *ex situ* thermal treatment (*cf.* Sec. 2.2.4). Both phenomena are surely interlinked since they occur in a similar temperature range, however, the missing oxidation environment in the first case plays a crucial role.

As stated in the introductional part, (Ga,Mn)As thin films can not be tempered at temperature exceeding the growth temperature ($\leq$ 200°C). Tempering at higher temperatures would eventually lead to an out-diffusion, not only of the interstitial but also of the substitutional Mn. However, thermal treatment is useful, for instance, in order to heal out surface damage. Thus, the effects of this low-temperature tempering ($\leq$ 200°C) on the stoichiometry have been investigated by a long-term measurement series. Oxide layer thickness, contaminations, and stoichiometry of a sample, not otherwise treated, were investigated as a function of tempering time. The sample was kept in UHV during the entire series in order to avoid re-oxidation of the surface or the deposition of additional contaminations from air.

Oxide layer thickness and contaminations

Figure 4.1 shows the two main indicators for contaminations: panel (a) illustrates the overall oxide layer thickness, separately determined for As and Ga (*cf.* Sec. 3.3.3), whereas the ratio of O and C $1s$ to As $2p_{3/2}$ in panel (b) represents other contaminations. The error bars for this and all similar upcoming graphs is basically given by the uncertainty in the Shirley-background subtraction and the resulting inaccuracies in the determined integral intensities. The issue of the IMFP has not been taken into account, since only relative changes are discussed and accurate values are not required. Therefore, all values for the total oxide layer thickness have been obtained by the TPP-2M equation [Eq. (3.9)]. More surface and bulk sensitive information is determined from the $2p_{3/2}$ (open triangles) and $3d$ core levels (open circles), respectively (*cf.* Tab. 3.4).

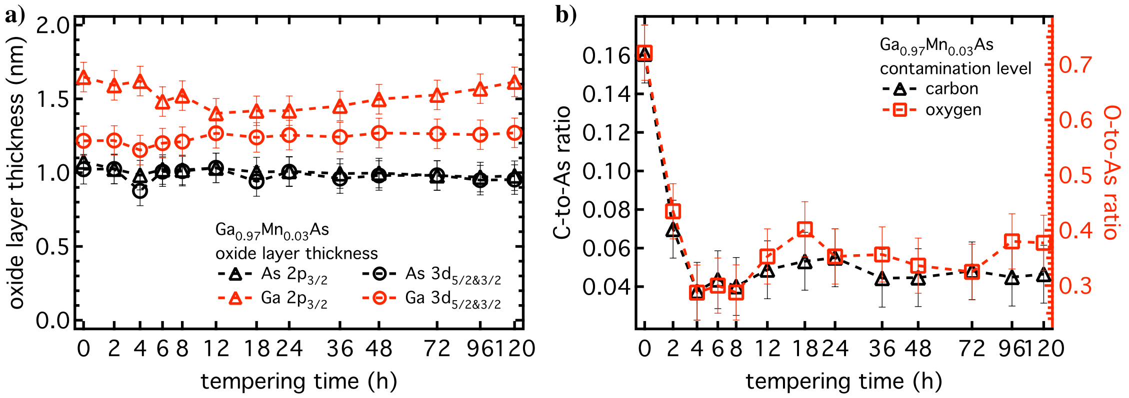

Figure 4.1: *Evolution of the oxide layer thickness [panel (a)] and the contaminations [panel (b)] of* $Ga_{0.97}Mn_{0.03}As$ *during long-term tempering at* 200° *C; all data were obtained under a detection angle of* $\alpha = 40°$ *with a photon energy of* 1486.6 eV*.*

While As [black in Fig. 4.1 (a)] shows more or less no change in the oxide layer thickness, neither for the surface nor for the bulk data, Ga [red in Fig. 4.1 (a)] shows some notable features. In particular the surface data decline within the first 12 h. Following that, there is a slow increase from 12 h to 120 h. Furthermore, the calculated thickness in the case of As is equal for surface and bulk, whereas the surface data of Ga are larger than the bulk values. In addition, the values are through out higher for Ga compared to As.

The carbon and oxygen contaminations in panel (b) behave similar. After a drastic decrease of the ratio within the first four hours, they level off and scatter around a mean value over the entire preparation time.

The different behavior of As and Ga is readily understood in the framework of the pile-up structure of the oxide layer described and quantified in Secs. 2.1.2 and 3.3.5. The oxide layer is Ga-rich and hence, the Ga-related values are larger than the As-related thicknesses. The initial decline is particularly pronounced in the surface data indicating that the responsible process is active in the first few monolayers. The decrease is attributed to the loss of the most volatile Ga species present at the topmost layer, e.g., Ga_2O. The increase for very long tempering times might indicate the beginning of the reactions labeled I-IV in Tab. 2.2. The temperature used is far below the given values in Tab. 2.2. However, it appears that the very long tempering times lead to measurable effects even though the temperature is nominally too low. The thermally activated reduction of As compounds leads to a further oxidation of Ga, which is again most pronounced at the surface. This reduction is not in contradiction to the constant As-related oxide layer thickness in Fig. 4.1. Firstly, the As-oxides are not further discriminated according to their oxidation state. Secondly, a reduction of a As_2O_5 molecule to the sesquioxide leads to an oxidation of four Ga atoms. Thus, the effect—even of minor importance for As—has a tremendous impact on Ga. But the total increase of approximately 15 % in oxide layer thickness for the Ga $2p_{3/2}$ core level and the long time scale already indicate that this process is negligible for the upcoming discussion.

The primary decrease in contamination concentration in the first few hours indicates the evaporation of very volatile, only physisorbed, contaminations such as water or various hydrocarbon compounds. They originate mainly from the standard cleaning procedure by acetone and isopropanol and the humidity in the laboratory air, prior to the sample transfer into the UHV apparatus. Within the error bars, no dramatic change in the ratio can be seen upon longer tempering times. The ratios stay fairly constant. This suggests that the remaining oxygen and carbon contaminations are the As and Ga-related oxides and low-volatile carbon compounds, respectively.

Stoichiometry

The stoichiometry within the probed volume in dependence of the tempering duration is given in Fig. 4.2. The As-to-Ga ratio was obtained by integrating the $2p_{3/2}$ and $3d$ core levels of both As and Ga. This provisional ratio was then normalized to the ratio of an *in situ* filed GaAs sample with a defined $1:1$ stoichiometry in order to obtain absolute values.

The bulk data (filled black circles) do not show any significant change upon tempering, however, they are slightly below the nominal ratio given by the chemical formula $Ga_{0.97}Mn_{0.03}As$ (indicated by the dashed parallel to the abscissa). In contrast to this, the surface data (filled red triangles) exhibit an increase within the first four hours. Furthermore, they are constantly smaller than their bulk counterparts.

The behavior of the stoichiometry supports the findings from the oxide layer thickness. The Ga-rich surface is the reason for the, in general, lower ratio in the surface data. For the initial increase of the ratio (increasing As content), two explanations are imaginable. On the one hand, it might be due to evaporation of the most volatile Ga-oxides from the surface as mentioned before. On the other hand, also another explanation is conceivable. The As $2p_{3/2}$ core level is the most surface sensitive measure as the photoelectrons have the lowest kinetic energy ($E_{kin} \approx 145\,\mathrm{eV}$). The difference to the Ga $2p_{3/2}$ photoelectrons ($E_{kin} \approx 370\,\mathrm{eV}$) is much larger than for the corresponding $3d$-shells. Thus, the IMFP is 64 % larger for the photoelectrons originating from the Ga $2p_{3/2}$, in comparison to their As counterparts. The relative difference is only 1.3 % for the $3d$-photoelectrons (*cf.* Tab. 3.4). Remembering that the evaporation of volatile contamination also occurs within the first 4 h of tempering, the increase of the composition at the surface might be a simple consequence of the larger damping of the As $2p_{3/2}$ signal by the capping contamination layer of O and C. After the removal of the contamination layer, the signal reflects the true stoichiometry of the surface. If this effect is dominate cannot be clarified within the current data set, however, it surely biases the results.

Conclusively it can be stated that tempering (Ga,Mn)As at 200°C does not have any major effects neither on the oxide layer thickness nor on the contaminations nor

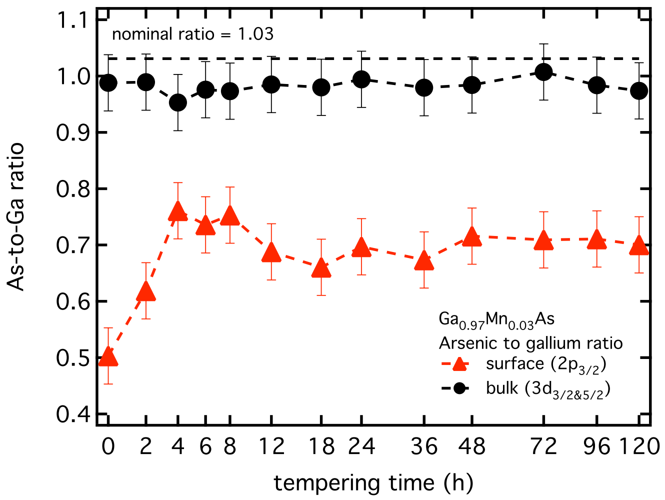

Figure 4.2: *Long time changes of the stoichiometry in the course of tempering of (Ga,Mn)As at* 200° *C; the stoichiometric composition was determined by the integrated intensities of the As and Ga* $2p_{3/2}$*- (red triangles) and* 3*d core level (black circles), respectively. All data have been normalized to an* in situ *filed GaAs sample. The topmost dashed line parallel to the abscissa indicates the nominal ratio according to the chemical formula* $Ga_{0.97}Mn_{0.03}As$*.*

on the stoichiometry. The first point disqualifies tempering at this temperature as a cleaning procedure, further supported by the second point. The oxygen and carbon contaminations are reduced, but not to a sufficient degree. However, the preservation of the stoichiometry indicates that preferential evaporation of As is not taking place at this temperature. Therefore, this procedure shows potential for the structural recovery of the surface, i.e., healing out. The effects of Mn segregation are postponed for the moment and will be dealt with in Sec. 4.4. In brief, also the Mn is unaffected by *in situ* tempering in harsh contrast to annealing *ex situ*, i.e., under oxidizing atmosphere.

4.2 Sputtering of (Ga,Mn)As

With the details and the nature of the sputtering effects as described in Sec. 2.1.5 in mind, it is clear that the parameters of the cleaning procedure, i.e., energy and flux density, are to be chosen as soft as possible. Higher energies and/or higher fluxes would lead to a faster cleaning but the probability of damages increases. The aim of this section is to find a compromise between ion energy and sputter duration. A clean surface is defined as oxide free (no shoulder at both the As and Ga core levels) and oxygen and carbon 1*s* core levels below the detection limit. All upcoming results have been performed with Ar^+-ions under an impinging angle of 45° to the sample plane. The technical settings of the sputter gun can be found in Tab. 4.1. Both sputtering and XPS measurements were conducted at room temperature.

As sputtering is a common surface preparation method the preparation of (Ga,Mn)As by ion etching has been under investigation in the literature. However, a detailed study of the effects of sputtering is omitted by all authors. Nonetheless, as was discussed in the introduction to dry-etching in Sec. 2.1.5, the effects of ion bombardment on the host GaAs itself are non-trivial. The presence of manganese in the ternary alloy is not expected to simplify things. Reports range from 750 eV Ar^+ at 1 μA for 5 min,[165] to 1 keV Ar^+ (no exact duration given)[166] or a trivial note that Ar^+ has been used (neither energy nor duration or current density given).[167] Even though the surface was studied by means of LEED, the authors fail to show results.[166] Stoichiometric aspects have not been dealt with in any case. Therefore, a dire need for a heuristic analysis of the processes taking place during sputtering and the effects resulting from them becomes obvious.

Table 4.1: *Sputtering settings of the Omicron ISE10 Sputter Ion Source used in the course of this thesis at an Ar base pressure of* 3×10^{-6} *mbar in the UHV system.*

energy (eV)	ion current (μA)	ion density ($\mu A/cm^2$)
500	21.7	2.13
600	23.4	2.30
1000	22.4	2.20

Beam energy: 500 eV

Figure 4.3 shows the $3d$ core levels of As [panel (a)] and Ga [panel (b)] in the course of sputtering. The RTO spectra show large oxide peaks, thus indicating that the surface is heavily oxidized. The spectra have been recorded under normal emission further indicating that the sample is covered by a thick oxide layer. Upon sputtering the oxide peak of As is gradually decreased. Ga behaves somewhat different. The decrease is much less pronounced but between 30 min and 60 min total sputtering time the oxide component vanishes completely.

Figure 4.4 shows a more sophisticated analysis of the data in Fig. 4.3. Panel (a) gives the oxide layer thickness determined from the spectra shown in Fig. 4.3 and with Eq. (3.19). The stoichiometry in panel (b) was determined by the integral intensity of both core levels. The data have again been normalized to an *in situ* filed GaAs sample in order to obtain absolute values.

For As the thickness drops drastically and after 60 min no oxide peak is observed. Ga exhibits a different behavior. The drop occurs not before 30 min total sputtering time. A slight, though significant, asymmetry on the higher binding energy tail of the Ga $3d$

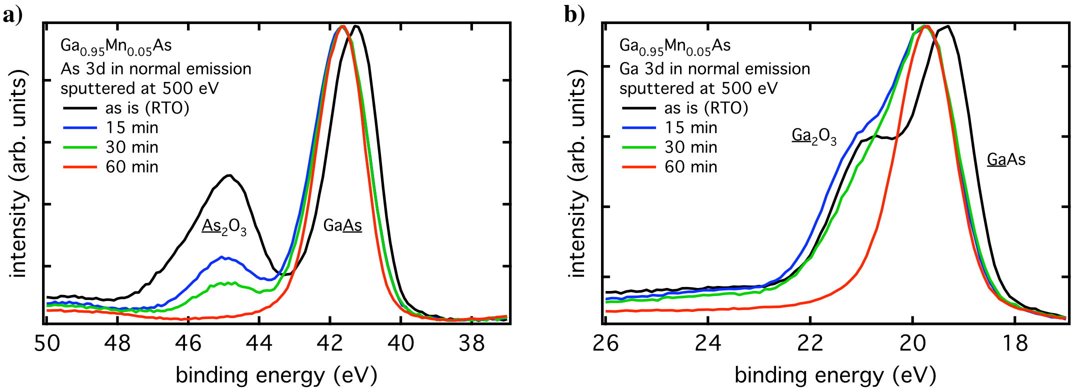

Figure 4.3: *As [panel (a)] and Ga [panel (b)] 3d core levels in the course of sputtering at 500 eV; all data were obtained at normal emission ($\alpha = 0°$, i.e., highest bulk sensitivity). For the as-grown sample the oxide related peaks at high binding (BE) energies are clearly visible, which are reduced upon sputtering, however, to a different extent for the two core levels.*

core level peak is responsible for the fact that even after 60 min of sputtering an oxide layer thickness can be calculated. Thus, the procedure was not able to remove all oxides. Concerning the stoichiometry, the sample starts with a slightly As-rich probed volume (within the margin of error). This changes dramatically after the first sputtering step which results in a Ga-enrichment. The surface related data [red curve in Fig. 4.4 (b)] show an even lower As to Ga ratio. This trend is enforced by the second sputtering step. After 60 min of sputtering the stoichiometry seems to be restored slowly. The C 1*s* and O 1*s* integrated intensities also show the expected decrease being below the detection limit after 60 min of sputtering.

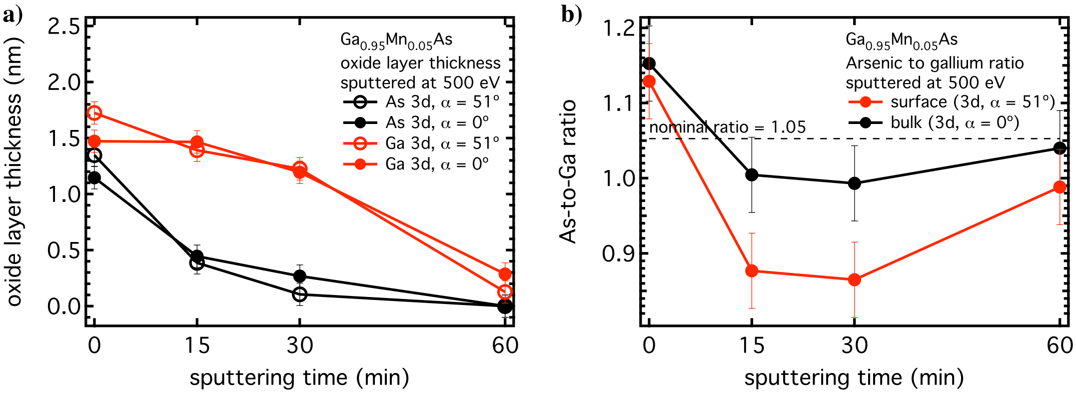

Figure 4.4: *Oxide layer thickness [panel (a)] and stoichiometry [panel (b)] determined on the basis of the As and Ga 3d in the course of sputtering at 500 eV; data have been obtained at $\alpha = 0°$ (bulk sensitive) and $\alpha = 51°$ (more surface sensitive). The stoichiometric data have been normalized to an* in situ *filed GaAs sample. The dashed line parallel to the abscissa indicates the nominal stoichiometry.*

All observations are again readily understood within the framework of the composition of the oxide layer described in Sec. 3.3.5. As is far less oxidized beneath the Ga-rich oxide layer. Therefore, it takes longer to remove all Ga oxides by the ion bombardment. This seems to be in contradiction to the location of the Ga-oxides near the surface. However, the higher absolute amount of Ga-oxides appears to be the dominant factor. The oxide layer thickness data in Fig. 4.4 (a) support the idea of a more time-consumptive removal of the Ga-oxide. The data on the overall composition in panel (b) are also in agreement with this picture. The sample starts with an As-rich probed volume. This indicates that the information depth with 1486.6 eV photons lies within the off-stoichiometry region. Upon sputtering, the topmost more or less stoichiometric oxide layer (product of the very first oxidation step) is removed and the Ga content increases. The increase is more pronounced for the surface [red line in panel (b)]. After the removal of the entire off-stoichiometry oxide layer (after 30 min of sputtering), the composition seems to be recovered slowly. In order to clarify, if steady-state conditions—i.e., the composition does not change with sputtering time—are reached after 60 min, a long-term sputter study has been conducted.

Beam energy: 600 eV

For technical reasons the beam energy was raised to 600 eV. It is assumed that changes in the sputter yield within this 100 eV are below the resolution of the stoichiometric analysis limited by the background subtraction and peak area determination. The sample had a little lower Mn content (i.e., higher Ga content) but did not have further differences to the sample shown before. The ion current was 23.4 μA under an incident angle of 45° to the sample plane. The literature reports[168] that the sputter yield of GaAs, in harsh contrast to other compounds, does not change significantly with the angle of incidence of sputter ions or crystal facet, as long as the impinging angle is larger than the glancing angle of around 5° to the sample plane. To accurately determine the point of steady-state conditions the measurement was made even more surface sensitive by including also the $2p_{3/2}$ of As and Ga in the analysis. The detection angle was however chosen to be $\alpha = 0°$. A comparison of the IMFP in Tab. 3.4 shows that the As and Ga $2p_{3/2}$ have a MED under normal emission of 0.7 nm and 1.0 nm, respectively, whereas the $3d$ orbitals under 51° have a MED of 1.8 nm. The data have also been normalized to an *in situ* filed GaAs reference.

The analysis in Fig. 4.5 shows, that within one hour of sputtering the As to Ga ratio changes from a Ga-rich surface to a nearly stoichiometric composition (from the chemical formula $Ga_{0.97}Mn_{0.03}As$ the ratio should be 1.03). After that, only slight changes are present. The ratio remains unchanged even after 5 h of dry-etching. A further astonishing point is the fact that the surface and the bulk do not show any significantly different behavior. Despite a constant offset they are superimposable. Concerning the O and C contaminations, no indications for oxide components at the As and Ga core levels were found after the first sputtering step. In addition, the 1s core levels of O and C, reflecting other contaminations such as water, hydrocarbons, and so on, were below the detection limit. So, the first sputtering was sufficient to remove all contaminations.

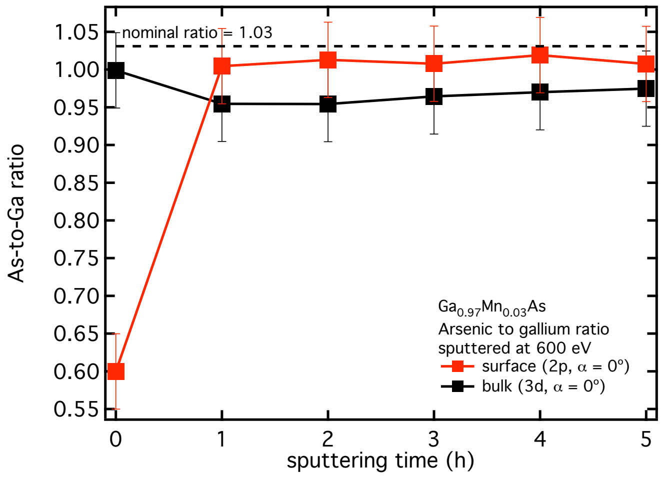

Figure 4.5: *Long time changes in stoichiometry in the course of sputtering of (Ga,Mn)As at* 600 eV*; the stoichiometry was determined by the integrated intensities of the As and Ga* $2p_{3/2}$ *and* 3d *core level, respectively. All data have been normalized to the As to Ga ratio of the same sample after* in situ *filing consecutively to the sputtering series. The dashed line parallel to the abscissa indicates the nominal ratio according to the chemical formula* $Ga_{0.97}Mn_{0.03}As$*.*

The starting point of a Ga-rich surface and a nearly stoichiometric bulk has been outlined in the previous section. The first sputtering step of 1 h is obviously enough to remove the entire off-stoichiometric surface. This is supported by the fact that no contaminations were detectable. The higher values for the surface ratio might be attributed to the background. Especially for the As $2p_{3/2}$ core level the background of inelastically scattered photoelectrons is extremely high leading to an overestimation of the signal.

The results are in qualitative agreement with the data of Malherbe *et al.*[169] on pure GaAs. Their Auger electron spectroscopy (AES) investigation gives evidence for a preferential sputtering of As, i.e., an As to Ga ratio smaller than one. They used Ar^+ ions with a little higher energy (650 eV) and a four times higher flux density of 10 $\mu A/cm^{-2}$. They concluded that the preferential sputtering of As increases with beam energy (and flux density) independently from incidence angle or crystal orientation. Nevertheless, the tendency to a slightly As-depleted probed volume (their AES data correspond to the "bulk" labeled data in Fig. 4.5) is the same. It has to be stated that the authors of Ref. 169 failed to give a total sputter time or at least a dose density, thus making a direct comparison vague.

In any case, the data lead to the conclusion that preferential sputtering is not a major effect for GaAs, at least at the present energy and ion current. The settings used seem to be gentle enough to ensure no major influences on the overall composition even though the difference in sputter yield and the depletion are expected to increase with energy and/or current. From an intuitive point of view, variances would have been expected for two elements in a bi-compound target. The two main factors for preferential sputtering are the mass difference and the difference in surface binding energy. However, since As has only a 7.5 % larger mass than Ga, this is ruled out to be the main reason. Besides, this would favor the preferential sputtering of Ga instead of As. Therefore, the surface binding energy seems to play the dominant role. Usually, the sublimation energy is taken as an indicator for the surface binding energy. In the light of the relatively large difference between $H_s(As) = 29\,\mathrm{kcal/mol}$ and $H_s(Ga) = 64.9\,\mathrm{kcal/mol}$[169] the As depletion becomes reasonable.

The condition of ion-assisted diffusion as described at the end of Sec. 2.1.5 seems to be met in the data presented in Fig. 4.5, as the "surface" data lie above the "bulk" data. However, the uncertainty in the data is too high to draw a final conclusion. Therefore, a combination of both effects has to be made responsible for the small, but detectable lack of As.

Most importantly, the results of the long-term 600 eV series in Fig. 4.5 suggest that the last data point of the 500 eV series in Fig. 4.4 (b) is already close to a steady-state condition. The initial complex stage affected by the interplay of sputter yield and concentration gradient seems to be bypassed and the absence of any other contaminations of O or C suggest sputtering at 600 eV for a total time of 1 h is sufficient to obtain a clean surface. However, since no LEED pattern could be observed after this procedure the call for other techniques arises. Tempering after the sputtering seems to be necessary and removal of the oxides by wet-chemical etching prior to sputtering may be a promising way to further optimize the cleaning procedure.

Beam energy: 1000 eV

Nonetheless, a firmer but short sputtering might also pave the way for a clean and ordered surface. For this reason, also a sputtering series at 1000 eV was conducted. The major results are shown in Figs. 4.6, 4.7, and 4.8.

Figure 4.6 shows the O 1s [panel (a)] and C 1s [panel (b)] in the course of the sputtering. The *as is* sample shows heavy contaminations by both oxygen and carbon. A drastic decrease in both is already observed after 10 min sputtering. Oxygen shows a slower decrease with no signal after 30 min total sputtering time. The drop for carbon is larger with almost no signal after 10 min. The residual carbon is hard to determine since the plasmon of the As LMM Auger peak series located at approximately 277.5 eV dominates the spectra for low carbon signals. However, it is obvious that the carbon signal does not vanish completely even after 30 min but persists. The ion bombardment seems to provide enough energy to remove all oxygen related contaminations (oxide components and water) but fails to remove the entire carbon. It is likely that the weak, remaining signal originates from the most strongly bound carbides.[25]

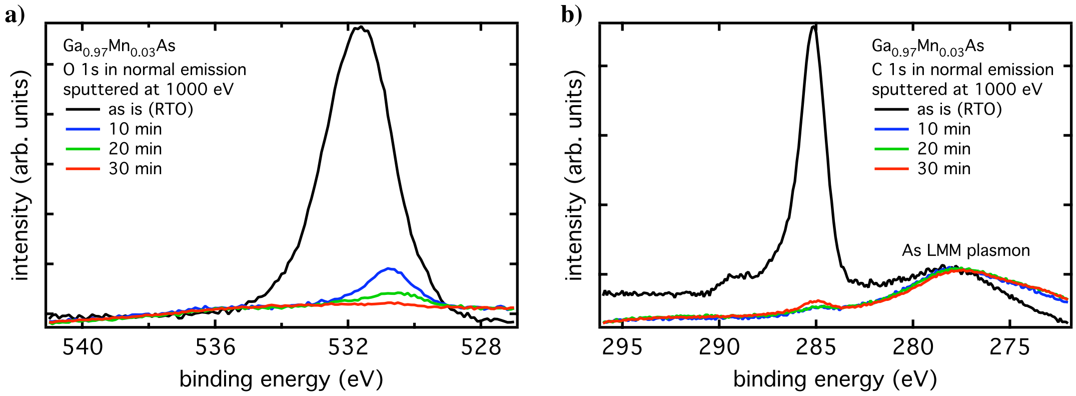

Figure 4.6: *O [panel (a)] and C [panel (b)] 1s core levels in the course of sputtering at 1000 eV; all data were obtained at normal emission ($\alpha = 0°$, i.e., highest bulk sensitivity). Also visible in panel (b), the plasmon of the As LMM-Auger peak at 277.5 eV interferes with the carbon peak making a clear identification challenging.*

The evolution of the As and Ga 3*d* core levels is shown in Fig. 4.7. After 10 min of sputtering no oxide shoulder is observed for any of the elements. In contrast to Fig. 4.3 the oxide component is removed by the first sputtering step.

The results of the stoichiometric analysis in Fig. 4.8 are comparable to the data of the 500 eV and 600 eV sputtered samples. The probed volume starts with an As-rich condition which gradual decreases with sputtering time. The composition after 30 min of dry-etching is below the nominal content given by the chemical formula.

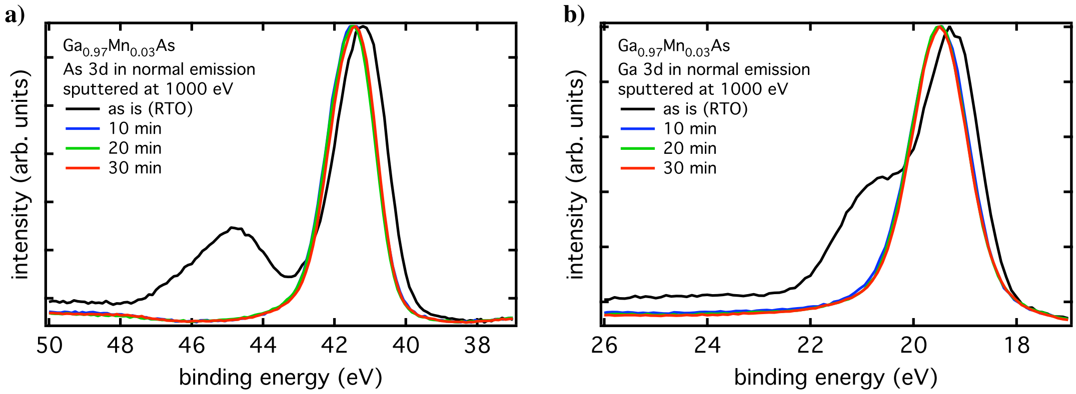

Figure 4.7: *As [panel (a)] and Ga [panel (b)] 3d core levels in the course of sputtering at 1000 eV; all data were obtained at normal emission ($\alpha = 0°$, i.e., highest bulk sensitivity).*

The drastic decrease of the oxygen signal after 10 min in Fig. 4.6 (b) is in agreement with the absence of an oxide shoulder in the As and Ga core levels in Fig. 4.7. The first sputtering step is obviously sufficient to remove most of the oxygen, both oxide components and water, and the residual O does not lead to a detectable oxide signal at the core levels. Even a more sophisticated analysis by means of fitting the spectra with two Voigt-profiles in order to calculate an oxide layer thickness shows, that the sputtered spectra can be easily fitted by one profile for the covalent As-Ga bond. Hence, an oxide layer thickness can only be calculated for the first spectra being approximately 0.8 nm (As) and 1.1 nm (Ga), respectively. These values seem to be in contradiction to the *as is* thicknesses given in Fig. 4.4 (a). But bearing in mind that all spectra shown here have been obtained within one year, it can safely be expected to be an aging effect. The larger oxide layer thickness for Ga, together with the As-rich probed volume, resemble the pile-up structure of the oxide again very well. The gradual decrease of the As/Ga ratio shows the same trend as for the 500 eV in Fig. 4.4. Upon sputtering, the initial As-rich composition in the probed volume reaches unity after 30 min. This is the same time scale as for 500 eV sputtering. Concerning steady-state conditions, it can, in the light of the results for the lower energy sputtering, safely be assumed that the composition will not change significantly after 30 min of sputtering. Hence, it is concluded that nearly steady-state conditions are met after half an hour of dry-etching.

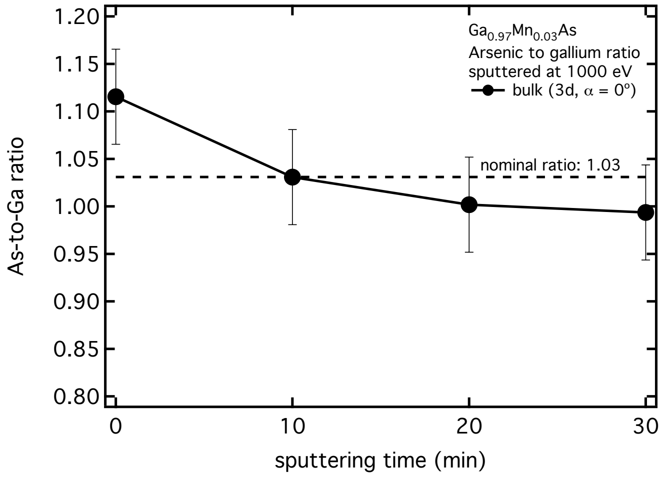

Figure 4.8: *Stoichiometry in the course of sputtering of (Ga,Mn)As at* 1000 eV*; values have been obtained as described in the previous stoichiometric analysis.*

In summary, the results of dry-etching at various beam energies provide the following findings. In agreement with the literature (*cf.* Sec. 2.1.5), the differences in the energy range of 500 − 1000 eV are rather marginal, particularly for the stoichiometry. Nearly steady-state conditions require at a minimum 30 min of sputtering at all energies. Concerning the contaminations, a higher beam energy results in a faster removal. Carbon contaminations appear to persist the longest, demanding a minimal total sputtering time of 30 min at all energies. Long-range surface ordering, determined by LEED, was not observed for any of the energies tested above, which outlines that other additional surface treatments are indispensable. Since sputtering at higher energies does not prove itself to be superior to lower energies, it is assumed that a more careful bombardment ensures the most reliable results. Henceforth, a sputtering treatment at 600 eV for a total time of 1 h is adopted to be a suitable cleaning procedure.

4.3 Wet-chemical etching of (Ga,Mn)As

After exploring the cleaning capabilities of *in situ* tempering and dry-etching, the effect of wet-chemical etching on oxide layer thickness, stoichiometry, and level of contamination of (Ga,Mn)As shall be addressed. Several etching agents (hydrochloric, sulphuric, and hydrofluoric acid) were tested for their ability to remove both the oxide layer and other contaminations from the surface.

The etching procedure by rinse with both concentrated acid (no oxidation agent) and deionized water was described in Sec. 2.1.4. In brief, the procedure consists of a 1 min rinse with the acid and an equally long rinse with deionized water. The experiments have been performed *ex situ* in a protective atmosphere of Ar (purity: 99.999 %) in a so-called glove bag. A sketch is shown in Fig. 4.9.

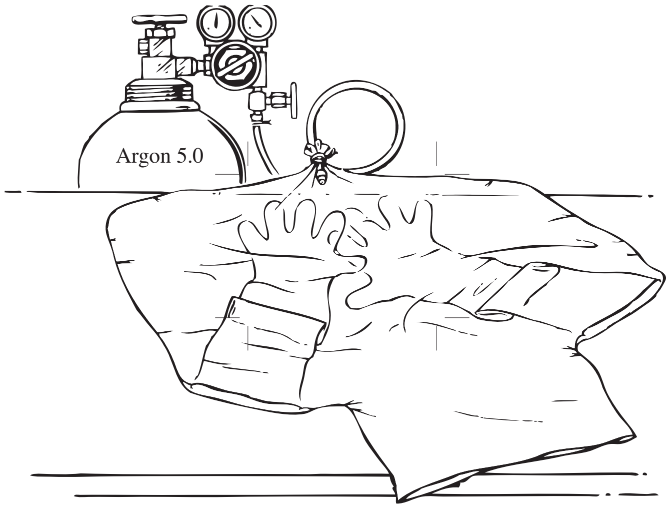

Figure 4.9: *Sketch of the glove bag used for etching under protective Ar atmosphere; the glove bag was evacuated and flushed once with Argon 5.0 (purity of 99.999 %) before the etching was performed.*[170]

The glove bag was evacuated with all instruments and chemicals necessary for the process and flushed once with Ar to minimize the residual air content. A glove bag was chosen instead of a glove box since it can more easily be evacuated and is much more handy, for instance, it can also be set up at other facilities such as synchrotron storage rings. After the etching process the sample was put into a transport box (still under Ar atmosphere) and brought to the nitrogen flooded load lock within less than 30 s. Exposure to air was thus shorter than 5 s.

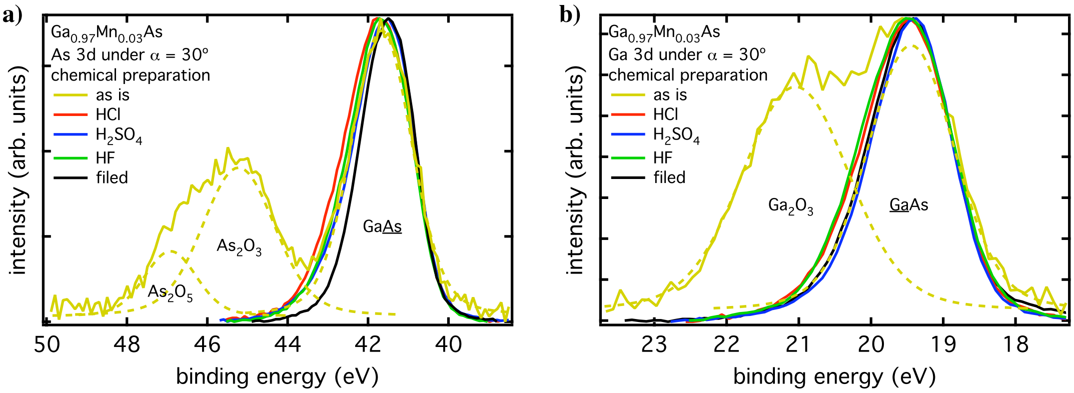

Figure 4.10: *As and Ga 3d core level treated with rocksalt acid (HCl, red), sulphuric acid (H_2SO_4, blue), and hydrofluoric acid (HF, green); reference spectra of an* in situ *filed (black) and the* as is *sample (gold) are also given.*

In Figs. 4.10, the As and Ga 3*d* core levels are shown prior and after treatment with various acids. Also shown is a reference GaAs sample, which has been filed *in situ*. Before the etching, both elements show a strong oxide peak on the high binding energy (BE) side. For As, the oxide peak exhibits a fine structure, which indicates that besides the sesquioxide (As_2O_3) also diarsenicpentoxide (As_2O_5) is present. In the case of Ga, the oxide peak consists of a single peak originating from the sesquioxide (Ga_2O_3). No evidences for higher oxidation states can be seen. By etching for 1 min, the oxide peaks are completely suppressed and the spectra are dominated by a single peak.

Considering further contaminations, the wet-chemical treatment shows a controversial picture. On the one hand, no residual anions could be detected (chemi- or physisorbed Cl^-, SO_4^{2-}, or F^-). On the other hand, significant amounts of carbon and oxygen were still measurable. In the case of carbon, sulphuric acid appears to work best with a decrease of the carbon signal in comparison to the arsenic signal from *as is* to etched samples by two orders of magnitude (only one order of magnitude in the case of hydrochloric and hydrofluoric acid). For oxygen the decrease is, almost equal for all acids, one order of magnitude. Obviously none of the acids is able to completely remove the carbon from the surface, which is in agreement with the literature.[12] The residual O signal originates most probably from the remaining water left on the sample by the neutralization rinse subsequent to the etching, since no oxide components are detected after the etching. However, this water is only physisorbed on the surface and could easily be removed by heating.

The line shapes of the Ga 3*d* core level of the etched samples in Fig. 4.10 (b) fall perfectly upon each other and are essentially identical to the *in situ* filed GaAs reference sample (black line in Fig. 4.10). This indicates that after the etching Ga is exclusively in the covalent state given by the Ga-As bond. The arsenic lines Fig. 4.10 (a) show a very different behavior. Although the oxide components are removed, an asymmetry at high binding energy (BE) appears. The etched spectra are considerably broader than the reference spectrum [FWHM: 1.00 eV (filed), 1.22 eV (HCl), 1.13 eV (H_2SO_4), 1.16 eV (HF)]. Fitting the spectra with two Voigt-profiles shows a second species shifted by approximately 1 eV. This shift is too small to be identified with any reported As-oxide component. However, the shift from elemental to covalent (bound to Ga) As is of this order.[171] Considering that arsenic is the more electronegative partner in GaAs, a shift to high BE for elemental As becomes reasonable due to the reduced screening of the core potential. This is similar to the HAXPES studies on etched MnAs thin films, which have shown that Mn is selectively removed in the films and mainly elemental As is left behind by etching.[171] The occurrence of elemental As becomes understandable when considering the layered nature of the oxide layer. The etching dissolves the dominating Ga-oxides at the surface and the As-oxides below. The surplus elemental As left behind after the initial oxidation remains widely unaffected. Such a selective behavior has not been observed up to this point since the cleaning procedures described in the previous sections do not discriminate between the different bonds of an element.

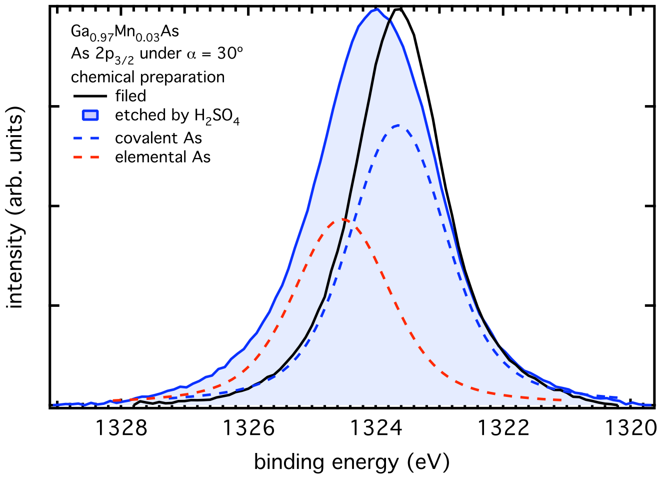

Figure 4.11: *As $2p_{3/2}$ core level treated with H_2SO_4; the presence of a second component at high BE (red dashed line) is much more pronounced in comparison to the 3d core level indicating that this species is mainly located at the surface.*

The claim that the additional species is elemental arsenic, which is built at the surface during etching, implies that this feature should be more prominent for more surface sensitive measurements. This is shown in Fig. 4.11 exemplarily for the As $2p_{3/2}$-line of the H_2SO_4 etched sample. Even though the sulphuric acid sample shows the lowest elemental arsenic content for the As $3d$ core level in Fig. 4.10 ($3d$ area ratios: $As_{covalent}$:$As_{elemental} \approx$ 4, HCl: 2.5, HF: 2) the second species becomes very strong at the surface. A comparison of the two fits (red and blue dashed lines) gives a ratio of 3 : 2 in favor of the covalently bound arsenic. Furthermore, the findings are backed by the stoichiometric analysis. The As/Ga ratio increases from approximately 0.95 for the *as is* samples to an average value of 1.4 for all etched samples. This shows that after the removal of the acid-soluble oxides, the insoluble elemental As is left behind.

Table 4.2: *Vapor pressures of HCl, H_2SO_4, and HF at 20°C in the available concentrations.*

chemical formula	HCl (37 %)	H_2SO_4 (95 %)	HF_{aq} (50 %)
vapor pressure (mbar)	21.3	0.4	16.5

At first glance, all three samples could be used, since none of them is significantly superior to the others. Even though sulphuric acid seems to be preferable in the light of the results presented above, particularly in regard to carbon contaminations, it has a tremendous technical drawback, as tabulated in Tab. 4.2. H_2SO_4 in the used concentration has a 40-fold lower vapor pressure at room temperature than the other two acids used. Thus, residual acid (on the sample holder, between sample and sample holder, etc.) leads to a massive virtual leak in the UHV system. The time required to bring the sample into the preparation chamber from the load lock was always at least three times longer than for the other acids. More severely, the sample then still led to a virtual leak, causing further waiting time. Despite the fact that all substances are very strong acids, hydrofluoric acid is utmost toxic. Hence, the effort required for the disposal and cleaning of the equipment is in no relation to the physical/chemical benefit on (Ga,Mn)As.

The above findings provide the following conclusion. Wet-chemical etching by concentrated acids is capable of removing the entire oxide layer at the surface. Although carbon and oxygen contaminations are reduced they are still present in the spectra in a sizeable amount. The former ones would probably be removed by adding an oxidation agent.[12] This is, however, prohibited by the thin layer character of the (Ga,Mn)As samples since the film would be completely dissolved in relatively short time (seconds scale). The remaining oxygen contaminations originate mainly from the neutralization process by deionized water. However, the deionized water does not lead to a re-oxidation and is essentially required for the removal of the highly reactive acid anions. Furthermore, performing the whole procedure under protective atmosphere and the quick mounting in the UHV system protects the surface sufficiently from re-oxidation. From the chemical and technical findings it is concluded that rocksalt acid is to be used for the etching.

4.4 Combination of wet-chemical etching, ion-milling, and thermal treatment

After investigating all relevant *ex situ* and *in situ* cleaning procedures with their unique advantages and drawbacks in Secs. 4.1 to 4.3 independently, the question arises if a combination of these methods would result in the desired bare, contamination free, and stoichiometric surface. In order to summarize the features of each procedure the main points are listed in Tab. 4.3.

Table 4.3: *Main features of the three different cleaning procedures; the table gives only the relevant advantages and drawbacks investigated and makes no claim to be complete.*

	tempering	sputtering	wet-etching
surface morphology	+	-	+
oxide layer	-	+	+
contaminations	-	+	-
stoichiometry	+	+	-

As can be seen, none of the techniques fulfills all requirements. Sputtering the sample with comparable low energy Ar^+ ions brings the most advantages, however, the ballistic damage to the surface has to be minimized by the other methods. The removal of the oxide layer by wet-chemical etching prior to the ion-milling reduces the required sputtering time whereas tempering the sample after the dry-etching heals out defects.

Contaminations and stoichiometry

Figure 4.12 shows the As and Ga $2p_{3/2}$ core levels of a sample which was consecutively treated by all three methods. The sample was first measured *as is*, i.e., without any treatment. The same sample was measured again after *ex situ* wet-chemical etching by rocksalt acids as described in Sec. 4.3. Thereafter, the sample was treated twice with a 30 min sputter/2 h temper cycle. In the third cycle, the sample was also sputtered for 30 min but tempered for 4 h. The series was concluded by two long-term tempering measurements after additional 25 h and 70 h of tempering. The corresponding $3d$ core levels have also been measured but are not shown here since the $2p_{3/2}$ core levels have a much higher surface sensitivity, which makes them more interesting for the current investigation.

Every preparation step can be tracked individually. The core levels show a large oxide peak, which is completely suppressed (As) or drastically reduced (Ga). After two sputter/temper cycles the line shape stays constant.

The contamination related $1s$ core levels of oxygen and carbon in Fig. 4.13 also show the same behavior known from the previous sections. The initially strong O and C signals are reduced by the wet-chemical etching. However, this reduction is much more pronounced for O. The dry-etching leads to a further gradual decrease of the oxygen signal and also the carbon is now significantly affected by the ion-bombardment. Comparable to the host core levels, two sputter/temper cycles yield a surface with contaminations

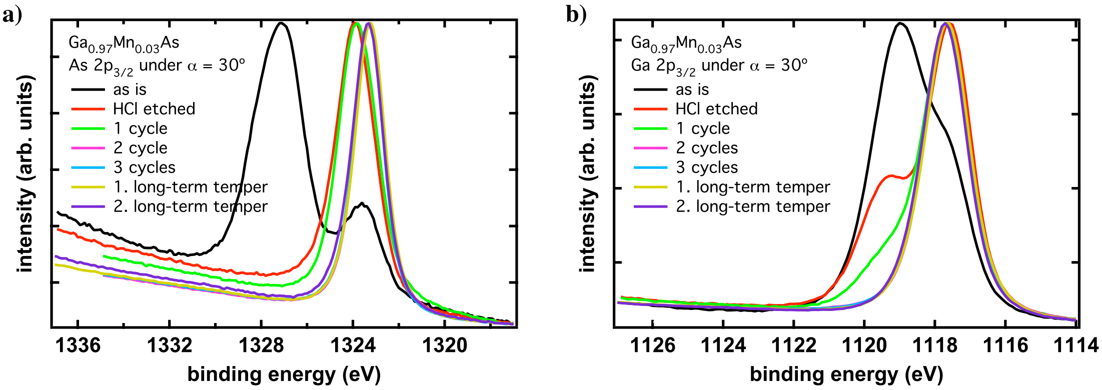

Figure 4.12: *As and Ga $2p_{3/2}$ core levels of (Ga,Mn)As in the course of a combination of wet-etching, ion-milling, and tempering cleaning procedure; all data were obtained under an emission angle of $\alpha = 30°$.*

close to the detection limit. However, both signal start to reappear during the long-term tempering, resulting in measurable signals after 95 h of tempering.

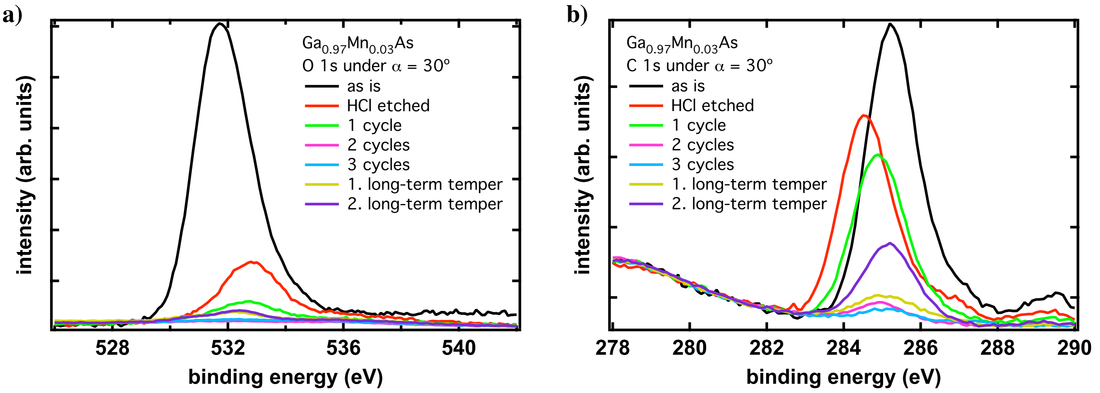

Figure 4.13: *O and C 1s core levels of (Ga,Mn)As in the course of combined wet-etching, ion-milling, and tempering clean procedure; all data were obtained under an emission angle of $\alpha = 30°$.*

The stoichiometry determined by the core levels shown in Fig. 4.12 is depicted in Fig. 4.14. The composition is obtained for the surface (red triangles) and volume (black circles) based on the $2p_{3/2}$ and $3d$ core levels, respectively. The sample starts with a Ga-rich probe volume. The wet-chemical etching (1 min rinse with rocksalt acid) results in an increase of the As content (point 1), which is leveled out by the first sputtering (point 2). Consecutive tempering results again in an As enrichment (point 3). The next sputter/temper cycle causes a drastic As depletion (point 4), which is only little affected by a further cycle. Only the long-term temper steps lead again to significant effects on the composition. The surfaces tends to become increasingly As-depleted, whereas the bulk composition stays nearly constant.

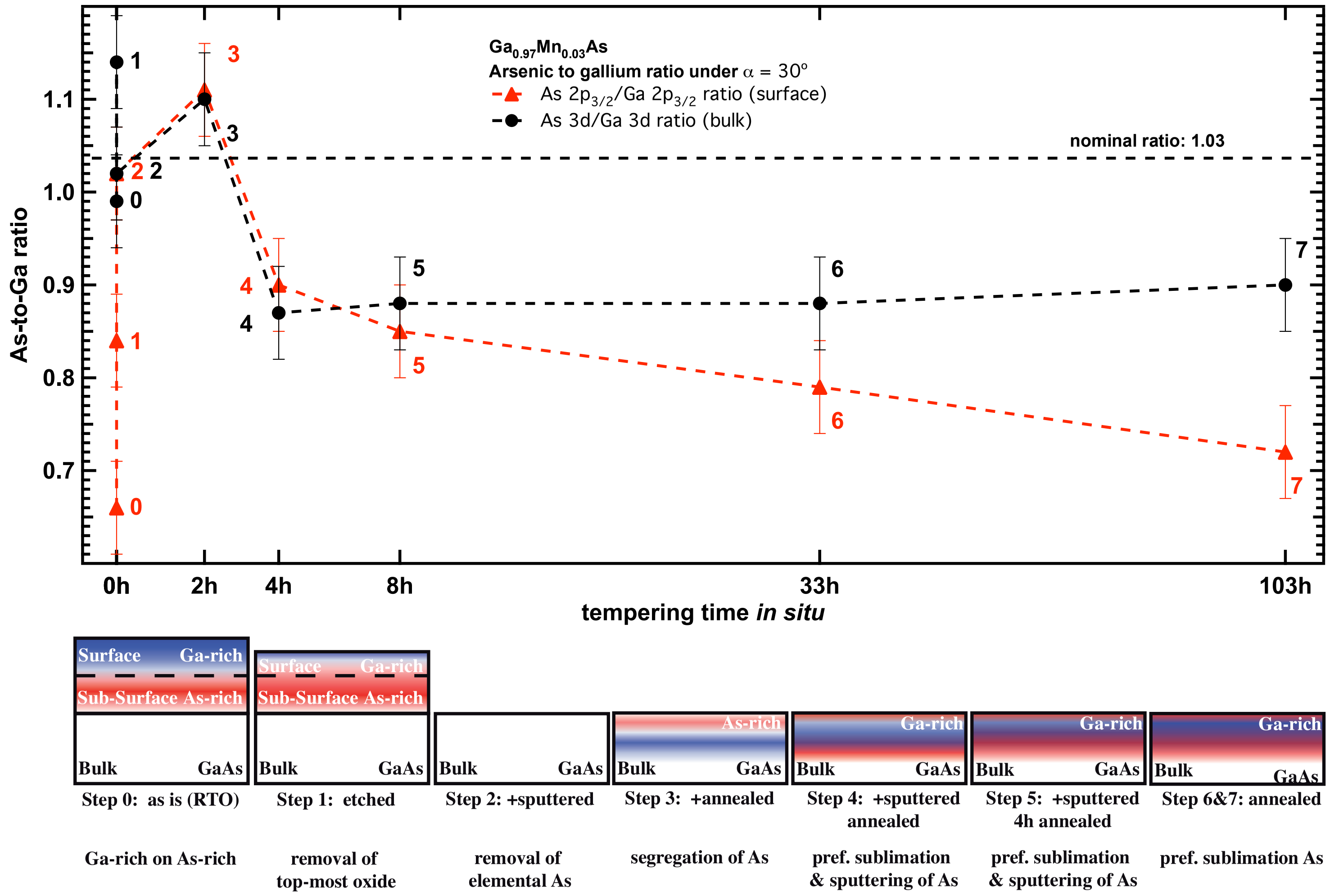

Figure 4.14: *Evolution of the stoichiometry during a combined wet-chemical, ion-milling, and tempering treatment of (Ga,Mn)As; all data were obtained under an emission angle of $\alpha = 30°$. The stoichiometric changes in each individual preparation step can be tracked independently for both the surface (red triangles) and the bulk (black circles). The pictograms below give a sketch of the composition in each preparation step $(0 - 7)$.*

The core level spectra in Fig. 4.12 together with their analysis in Fig. 4.14 suggest that a cleaning procedure of *ex situ* wet-chemical etching and two sputter/tempering processes is the adequate recipe. Both core levels are heavily oxidized indicated by the dominant oxide shoulder. The wet-chemical etching reduces this shoulder for As completely, however, the main peak is shifted to high BE proving that a certain amount of elemental As is left on the surface as described in the previous section. Two sputter/temper cycles are required to eliminate this spectral contribution from elemental As. The higher amount of Ga-oxides in the oxide layer seems to be the reason that even after one sputter/temper cycle a oxide shoulder is observed in the Ga core level. A second cleaning step is required to suppress this shoulder.

A similar behavior is observed for the contamination $1s$ core levels in Fig. 4.13. Two cycles are essential to push both oxygen and carbon below the detection limit. The reappearance of both signals during the long-term annealing seems to be counterintuitive. A possible explanation lies in the denuded surface. The clean surface of a LT-MBE GaAs is expected to be less reactive than GaAs grown at common MBE temperatures ($500-600$°C)[27] and the sample was kept in UHV during the whole series. Nonetheless, the surface is very reactive and residual gases cannot be avoided even in an UHV apparatus. The long-term storage of the sample in the UHV apparatus may have led to a re-condensation of oxygen and carbon from the residual gas, not compensated by the tempering. Note, that no indications for a chemical re-oxidation can be found at the As and Ga core levels. The shifts of the O and C $1s$ core levels between each step are probably due to the complex surface chemistry. An investigation of these effects is not part of the current study. Here, only a general reduction of the signal is important.

The complex evolution of the stoichiometry in Fig. 4.14 can readily be explained with aid of the previous sections. The starting point is a Ga-rich surface (point 0), which is a consequence of the preferential oxidation of Ga (*cf.* Sec. 2.1.2). The wet-chemical etching removes the oxides, but leaves the elemental As widely unaffected, which leads to an increasing ratio (point 1). This (elemental) As-rich layer is subsequently removed by the sputtering (point 2) which leads to a homogeneous (both curves coincide) and stoichiometric (ratio almost equal to the nominal ratio) surface. The following tempering step results in an As-enrichment within the probed depth (both curves rise, point 3) followed by an As-depletion by another sputter/temper step (point 4). At this point, the ion-assisted As-depletion and/or As sublimation seems to gain in importance. A further cycle (with four instead of two hours tempering) gives no major changes, indicating that steady-state conditions are met (point 5). Further long-term tempering leads to a loss of As at the surface, i.e., As sublimation (points 6 & 7). This is different from the results of Sec. 4.1. An explanation for this might be the oxide layer. In the previous tempering series the oxide layer remains quite unaffected by the thermal energy input. Hence, this capping layer of comparable stable compounds could have acted as a segregation barrier, prohibiting As sublimation. In the present case, the initial cleaning steps with both wet- and dry-chemical leave a denuded surface, which now permits the direct evaporation of As from the compound into the vacuum for long tempering times.

Mn 2p doublet

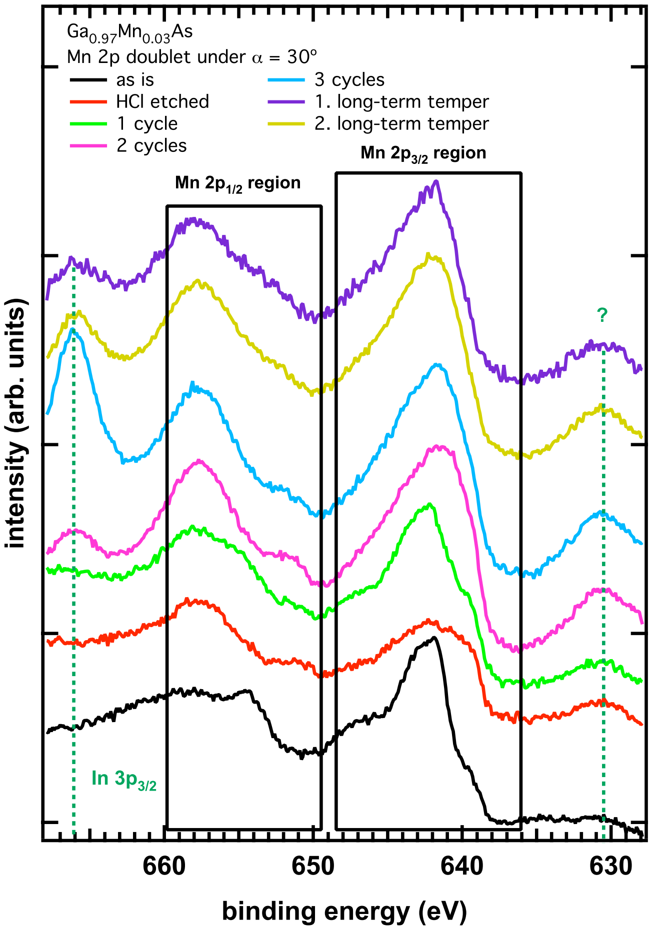

Figure 4.15: *Influence of the combined wet-chemical, ion-milling, and tempering preparation of (Ga,Mn)As on the Mn* 2p *doublet; spectra have been recorded under angle* $\alpha = 30°$ *after each preparation step.*

Figure 4.15 shows the effects, the sample treatment has on the Mn 2p doublet signal. The detailed shape of the spectra shall be disregarded for the moment and will have a decent discussion in the following chapter. Only the overall intensity is discussed here. The spectra have been normalized to the number of sweeps and a linear background has been subtracted (with identical slope for all spectra). The base lines have been shifted vertically for the sake of clarity.

It is obvious, that the peak shapes change significantly between each preparation step. The integral intensities, however, stay nearly constant through out the entire series. The two final long-term tempering steps in Fig. 4.15 also complete the study of long-term tempering of Sec. 4.1. The spectra in Fig. 4.15 give no indications for a sizeable decrease or increase of the Mn concentration in the probed volume. The absence of Mn segregation during *in situ* tempering at this temperature (200°) is in sharp contrast to annealing of (Ga,Mn)As at comparable temperatures (190°) under oxidative atmosphere, which will be addressed later. The missing oxidative atmosphere seems to prohibit Mn segregation, although the oxide layer, known to be a segregation barrier,[4] has been removed. This is a crucial finding, as in particular the transport and magnetic properties of (Ga,Mn)As are mainly determined by the carrier concentration/active Mn concentration which is influenced by segregation. It is thus concluded, that tempering can act as a method, which leads to reproducible results for samples with various Mn concentrations even in the low and high doping regime (high Mn_{int} concentration), since the physical properties of the sample seem not to be affected.

Besides the Mn related main structures at around 641.5 eV and 652 eV, Fig. 4.15 shows two additional structures. Despite intense research, the structure at around 630.5 eV could not be ascribed to any reasonable line. In contrast to this, the peak at around 666.1 eV is the In $3p_{3/2}$ core level. Interestingly, this peak occurs and vanishes again after the long-term tempering. Its appearance can be understood by the method of the crystal growth. The host GaAs wafers are fixed by In before (Ga,Mn)As is grown.[40] This In remains at the bottom of the sample when welded by tantalum wires on an UHV sample holder. In has obviously creeping abilities allowing it to escape between sample and sample holder when tempered in UHV. Thus, a part of the In seems to creep onto the surface leading to a sizeable contribution to the spectra. As a rule of thumb (the photoionization cross sections are nearly identical)[159] the In peak is as high as the Mn peak so the concentration should be equal (around 3 % in the given case). Upon further tempering the In seems to further spread on the sample and holder, leading to an overall loss in In spectral weight in the measured area. This emphasizes the fact that not only intrinsic features of the system under investigation have to be taken into account but also technical aspects can have tremendous effects.

Surface topology

Following the spectroscopic studies presented above, the sample topology was investigated by means of low energy electron diffraction (LEED) and atomic force microscopy (AFM) measurements. The observation of a LEED pattern required at least two cycles of sputtering and tempering. The resulting images for samples after wet-chemical etching and two sputter/temper cycles are shown in Figs. 4.16 and 4.17.

The LEED patterns in Fig. 4.16 have been obtained with beam energies around 35 eV, i.e., under very surface sensitive conditions. The 1×1 pattern along the high-symmetry directions $\langle 100 \rangle$ of the GaAs host [samples were grown on the (001) plane] are clearly observed. However, the expected (1×2) reconstruction known from *in situ* reflection high energy electron diffraction (RHEED) directly after the growth cannot be seen.[40] But even for *in situ* probed (Ga,Mn)As surfaces immediately after the growth, this

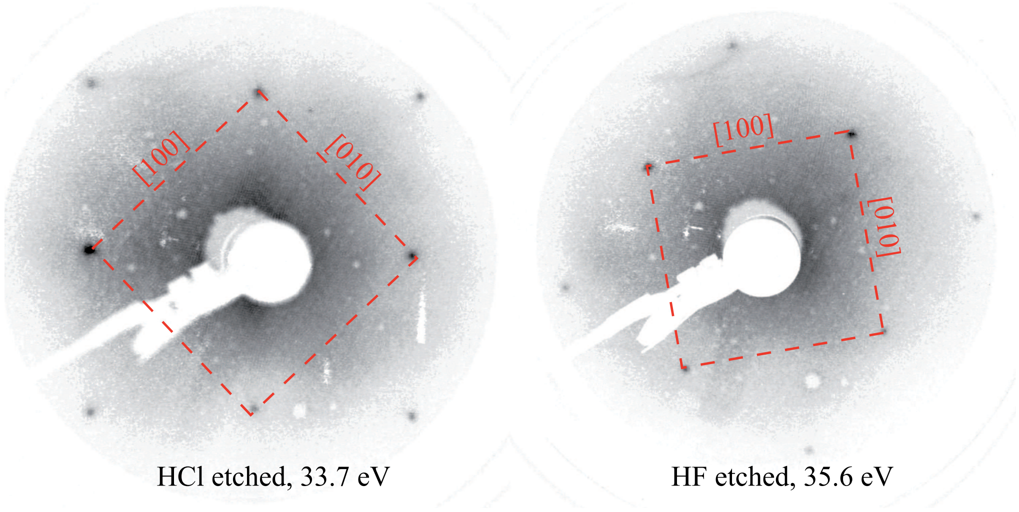

Figure 4.16: *LEED patterns of (Ga,Mn)As at 33.7 eV and 35.6 eV; both samples have been treated by wet-chemical etching (HCl and HF, respectively) and two sputter/temper cycles. Pictures have been converted into black and white and inverted.*

reconstruction is difficult to observe.[41] The patterns in Fig. 4.16 have been obtained for samples etched with hydrochloric acid [panel (a)] and hydrofluoric acid [panel (b)]. The two different acids did not show significant differences, although subjectively judged, the spots for the HF are a bit brighter and show more contrast. This backs the findings in Sec. 4.3. These patterns prove, that the samples exhibit atomic long range order at the surface comparable to the coherence length of the electron beam which is typical in the order of 100 nm.

The AFM measurements in Fig. 4.17 further support the success of the cleaning procedure. At first glance, the surface looks rather grainy, however, major structure cannot be identified. A topological profile along the white line in the picture is shown at the bottom of Fig. 4.17. Over the whole scan of 450 nm a maximal peak-to-valley difference of 1 nm is observed. Several scans at different points of the sample reveal similar results. This value is even smaller than the typical 5 nm modulations, being observed directly after the growth. It has to be noted, that this outstanding results have been obtained, even though the AFM experiments were not performed in the same UHV apparatus as the XPS and LEED experiments.

It shall be noted that all results presented above have been obtained on *as-grown* samples, i.e., the samples have not been annealed *ex situ* in order to optimize the transport and magnetic properties. Complementary measurements on post-growth annealed samples impressively demonstrated that the same procedure works equally well for optimized samples. All findings are identical to the results of *as-grown* samples.

In summary, an elaborated combination of cleaning procedures does not only lead to a clean and nearly stoichiometric surface, but results also in a very flat topology. The

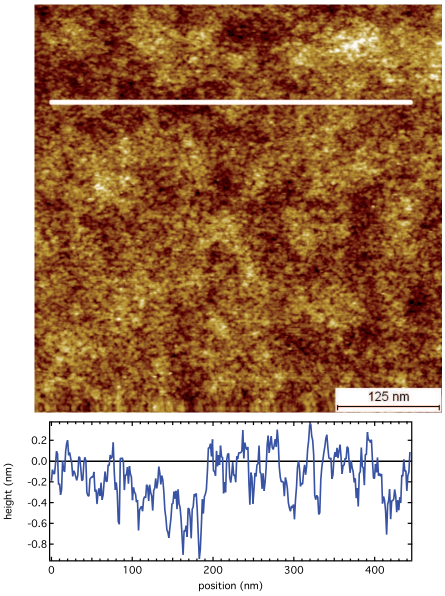

Figure 4.17: $500 \times 500\,nm$ *AFM picture of a (Ga,Mn)As surface after a preparation in the aforementioned manner; the top panel gives the real space image with a typical altitude profile along the white line in the bottom panel.*

optimal combination of short and soft sputtering with comparable long tempering yields clean and smooth surfaces. The initial wet-chemical treatment is utilized to remove the natural oxide layer and serves to reduce the required sputtering time. The spectroscopic data are in agreement with processes taking place in pure GaAs whereas the microscopic investigations are, at the current point, the first documented images of post-growth cleaned (Ga,Mn)As samples. Therefore, it is proven that, in contrast to claims in the literature, high-quality (Ga,Mn)As can reliably be restored by conventional post-growth surface treatments.[172,173] Thus, the way is paved for even more surface sensitive methods such as UPS or STM, which have up to now only be performed on *in situ* grown and measured samples or along the intrinsic $\{110\}$ cleavage planes.

5 Electronic structure of (Ga,Mn)As

5.1 Thermally activated surface segregation of manganese in (Ga,Mn)As

The key issue of this section is the investigation of the process leading to the improvement of the magnetic properties by *ex situ* thermal treatment. Annealing effects in $\mathrm{Ga}_{1-x}\mathrm{Mn}_x\mathrm{As}$ have been studied by various techniques in the literature. Channeling Rutherford backscattering (c-RBS) and channeling particle induced x-ray emission (c-PIXE),[51] X-ray absorption in magnetic circular dichroism,[93] and Auger electron spectroscopy[94] have been applied as well as theoretical studies using first-principle Monte Carlo simulations.[59,174] Those results gave evidence that the surface segregation of the loosely bound interstitial Mn causes the improvement of the magnetic and transport properties.

In order to quantify this effect, hard x-ray PES (HAXPES) has been conducted at beamline BW2 of HASYLAB, DESY in Hamburg, Germany, using a SCIENTA SES-200 electron spectrometer optimized for photoemission in the hard X-ray regime.[175] By choosing the excitation energy in the hard X-ray region ($> 2\,\mathrm{keV}$) the probed depth can be as large as 15 nm due to the high kinetic energy of the photoelectrons (*cf.* Sec. 3.3). The data presented here were taken with an excitation energy of $h\nu = 4.5\,\mathrm{keV}$ and an overall energy resolution of 0.7 eV. All spectra shown are calibrated to the position of the Au $4f_{7/2}$ (binding energy 83.9 eV) signal of an Au foil in electric contact to the sample.

(Ga,Mn)As thin films with a nominal Mn concentration of 5.5 % and a thickness of 60 nm were grown on a GaAs substrate by LT-MBE at 270 °C.[55] The films were thermally treated in air at 190 °C between 10 and 250 h in order to obtain snapshots of the chemical composition and chemical states during the segregation process. As performed in the previous chapter, reference data on a bulk MnAs[130] and a bulk GaAs sample were taken, whose surfaces were cleaned by *in situ* filing, thus providing an oxide-free and stoichiometric signal as reference.

Annealing induced changes in the overall oxide layer

First of all, the overall oxide layer shall be investigated. Figure 5.1 (a) shows the spectrum of the As $2p_{3/2}$ core level as function of annealing time. It consists of two

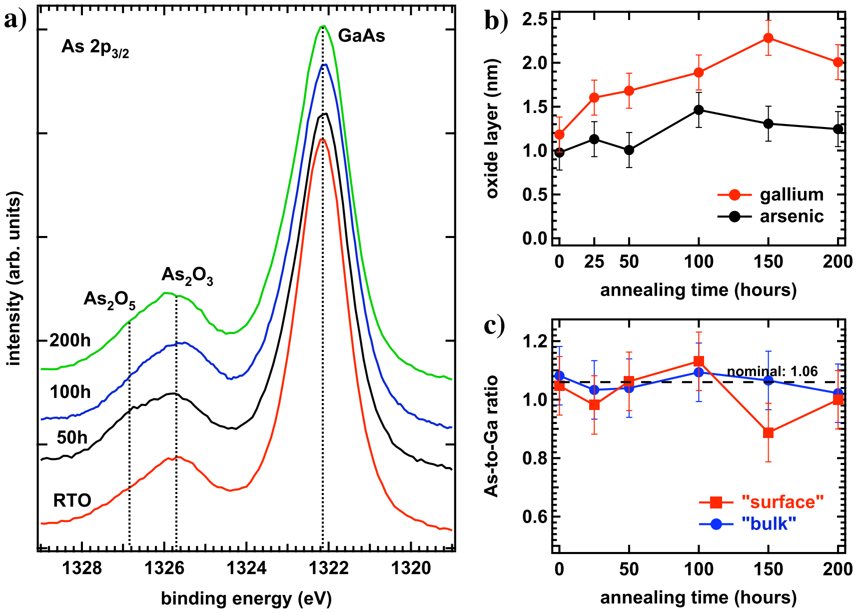

Figure 5.1: *Effects of the annealing on the As and Ga core levels in (Ga,Mn)As. (a) Evolution of the As $2p_{3/2}$ core level spectra of a room temperature oxidized sample (RTO) as function of annealing time at 190 °C recorded in normal emission geometry. The oxide related peaks gain intensity at the expense of the intrinsic peak. (b) Oxide layer thickness as obtained from the spectra and Eq. (3.19), selectively for As and Ga. (c) As-to-Ga ratio at the surface ($\alpha = 60°$) and in the bulk ($\alpha = 0°$).*

features, with an intense peak at 1322.2 eV corresponding to the intrinsic As species, while the broad side peak at high binding energy (BE) results from oxidized As at the surface. The term "intrinsic" refers here to As bound to Ga. The different energy of As bound to Ga and bound to Mn is too small to be resolved. Furthermore, since only one out of ten As is bound to Mn the As main peak is dominated by the signal from As bound to Ga. The main oxide component is again As_2O_3, as described in the previous chapter. The high BE tail of the oxide peak is attributed to higher oxidation states such as As_2O_5.

At first glance the relative oxide weight does not seem to depend strongly on annealing time. However, a closer inspection reveals that the integrated intensity of the oxide peak grows slightly at the expense of the intrinsic As signal. The same behavior is observed in the Ga $2p_{3/2}$ spectrum (not shown here). The oxide layer thickness has been determined by Eq. (3.19) with $\alpha = 0°$, the result of which is shown in Fig. 5.1 (b).

The graph reflects the evolution of the thickness as a function of annealing time for both the As $2p_{3/2}$ (black) and Ga $2p_{3/2}$ (red) core level. The as-grown, i.e., room temperature oxidized (RTO), sample gives an initial thickness of 0.98 nm for As and 1.18 nm for Ga. This is less than 50 % of the value reported by Allwood *et al.*[26] for RTO pure GaAs. Likewise, Malfait and co-workers[99] reported values of 2 nm and 5 nm for as-grown and annealed (Ga,Mn)As samples, respectively. This discrepancy may, on the one hand, originate from the uncertainty of the IMFP λ in Eq. (3.19). On the other hand, the samples in Ref. 99 were annealed under pure oxygen atmosphere and not in air. However, the overall trend of doubling the oxide layer by the annealing protocol is identical.

Figure 5.1 (b) further shows that the oxide layer thickness grows up to 1.46 nm for As after 100 h of annealing whereas Ga yields a maximum of 2.29 nm after 150 h. The thicker Ga-related oxide layer and the increasing discrepancy due to preferential oxidation of Ga have been exploited in Sec. 3.3.4 and, in detail, been examined in Chap. 4.

Concerning the stoichiometric composition, the data in Fig. 5.1 (c) show that the As-to-Ga ratio is rather constant for all annealing times (the nominal ratio of 1.06 determined from the chemical formula $Ga_{0.945}Mn_{0.055}As$ is indicated by the black dashed line). This is attributed to the large probing depth of HAXPES averaging over the entire off-stoichiometry region (oxide layer *plus* As-rich subsurface), even for a detection angle of $\alpha = 60°$. Accordingly, deviations of the stoichiometry can only be observed with more surface sensitive measurements, e.g., lower excitation energies, as presented in Chap. 4.

Annealing induced Mn surface agglomeration

Even more pronounced effects, induced by the thermal treatment, can be seen in the Mn spectra, as displayed in Fig. 5.2 (a). Like in Fig. 5.1 the data were recorded in normal emission geometry ($\alpha = 0°$), i.e., at highest volume sensitivity. The data are comparably noisy what is accredited to the low Mn concentration and the suppressed photoionization cross section for such a high $h\nu$. This is partially countervailed by the extremely high flux of storage rings in comparison to laboratory light sources, which allows for the acquisition of spectra in a reasonable time. However, due to the low signal-to-noise ratio the discussion will focus on the Mn $2p_{3/2}$ spectrum. Notwithstanding, everything stated here, also holds for Mn $2p_{1/2}$.

In case of the RTO sample the spectrum shows a broad structure with no distinct peaks visible. Upon annealing in air the feature on the high BE side strongly gains intensity while the low BE peak stays nearly constant. Also the statistics is improved which is not due to experimental changes, but the Mn content.

From the integrated Mn $2p$ signal the stoichiometry is determined and set into relation to the whole matrix by the reference samples. The as-grown sample [blue line in Fig. 5.3 (b)] shows no angle-dependence. A different behavior is observed for the annealed sample. Exemplarily for the annealed samples, the red line in Fig. 5.2 (b) shows the depth profile of the 100 h annealed sample. A clear increase of the Mn weight at the sample surface is apparent.

The Mn content as a function of annealing time is shown in panel (c) of Fig. 5.2. The Mn concentration of the RTO sample is 5.6 % (in the "bulk" data, i.e., measured in normal emission), which is in extremely good agreement with the 5.5 % obtained by XRD after the MBE growth,[55] underlining the success of using reference samples. The concentration then raises to 13.6 % (a factor of 2.3) in the bulk after 100 h and to even 19.9 % (a factor of 4.3) at the surface ($\alpha = 60°$) after 150 h. Furthermore, the difference between bulk and surface concentration increases with annealing time.

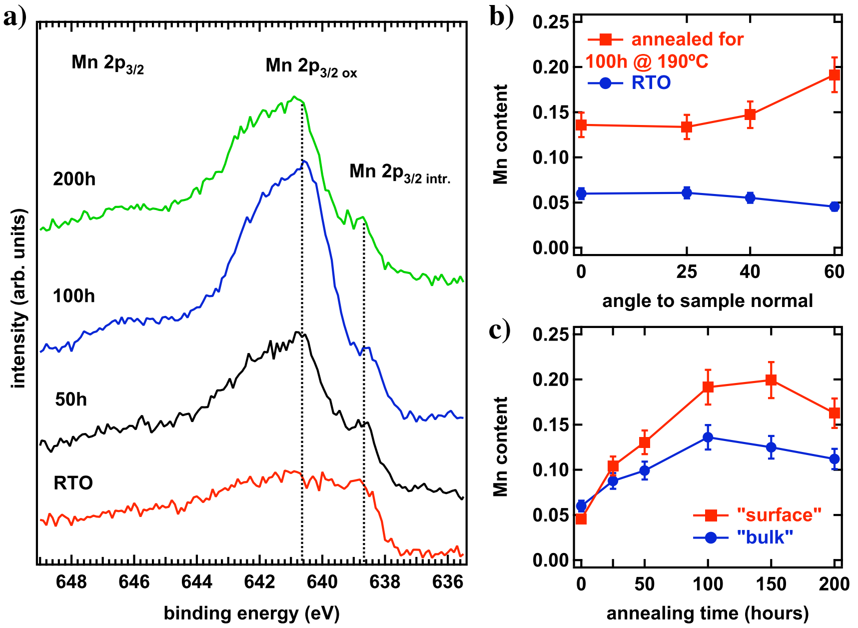

Figure 5.2: *(a) Evolution of Mn $2p_{3/2}$ core level spectra recorded in normal emission geometry on a room temperature oxidized sample (RTO) as function of annealing time at 190 °C. The oxide related Mn component increases at the expense of the intrinsic Mn peak of $Ga_{0.95}Mn_{0.05}As$. (b) Mn content as a function of emission angle for as-grown and 100 h annealed samples. (c) Mn content as function of annealing time for two different probing depths ("bulk" and "surface" corresponding to emission angles of 0° and 60° to the surface normal, respectively).*

The stoichiometric data of the as-grown sample [blue line in Fig. 5.2 (b)] show no angle-dependence. This proves, that a homogeneous depth distribution is present in the initial situation. This is at variance to previous reports which show a Mn concentration gradient *increasing* towards the surface in as-grown samples.[4,176] This discrepancy is not understood yet, especially when keeping in mind that the present samples have been grown at higher temperatures as compared to Ref. 4. Since the mobility of Mn in GaAs is a strong function of growth temperature, this would imply an even stronger gradient to the surface for samples grown at higher temperatures.

The increasing Mn content, together with the formation of a pronounced concentration gradient upon *ex situ* thermal treatment, confirms a surface segregation of Mn. The increase at the surface is larger than in the bulk, resulting in a divergence of surface and bulk content by annealing. The slight decrease of the Mn surface content after 200 h annealing is not fully understood within this reasoning. It may signal the onset of additional processes, such as evaporation, and requires therefore further investigation.

Since the content was determined based on the As-to-Mn ratio it is imaginable that a loss of As may bias the analysis. However, the annealing temperature was kept low enough to avoid evaporation of As as is known from cleaning procedures on pure GaAs[30] and the As-to-Ga ratio in Fig. 5.1 (c) does not show anomalies within the error bars.

Mn 2*p* doublet line shape changes

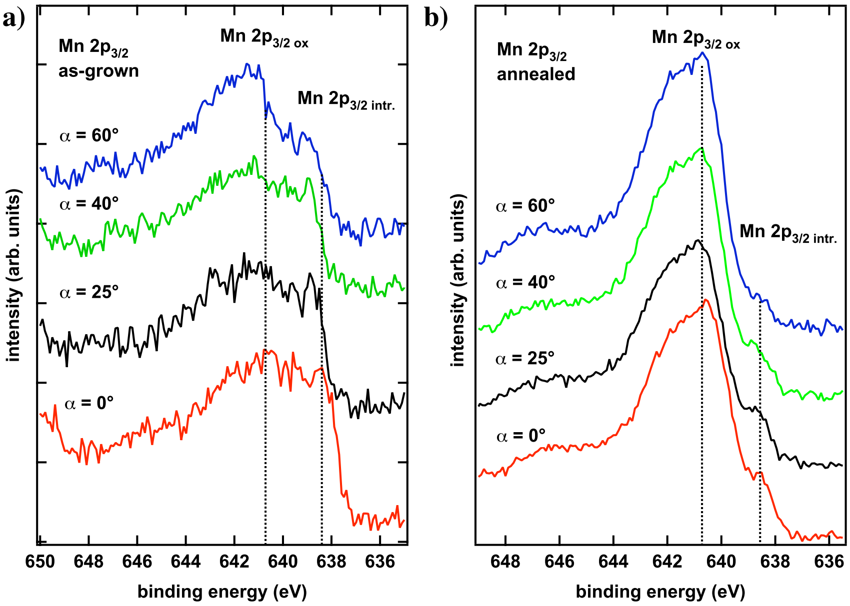

Figure 5.3: *Angle-dependent Mn $2p_{3/2}$ core level spectra of a $Ga_{0.95}Mn_{0.05}As$ sample, as-grown (panel a) and annealed (panel b) for 100 h at 190 °C. The low BE shoulder at ≈ 638.6 eV increases in both samples with the probed depth. In the case of the as-grown sample, only a minor change in the line shape is observed. For the annealed sample, however, the high BE peak clearly dominates the spectra for all angles, and the low BE peak is nearly completely suppressed for the most surface sensitive geometry ($\alpha = 60°$).*

The investigation of the single spectra reveals that not only the total Mn concentration but also the Mn line shape exhibits a strong angle-dependence after the annealing (see Fig. 5.3). Panel (a) shows Mn 2*p*-spectra for four different emission angles of an as-grown sample whereas panel (b) depicts the same angle-series for a 100 h annealed sample. The latter reflects the general behavior of all annealed samples. The evolution of the graphs indicates that the high BE energy peak at around 640.7 eV does not only emerge upon annealing but is also more distinct at the surface, whereas the low BE peak is nearly completely suppressed. For the as-grown sample, only a slight angle-dependence is observed.

The assumption that the high BE peak originates from Mn-oxides at the surface is confirmed in Fig. 5.4. Here, the data are compared to spectra of other Mn compounds,

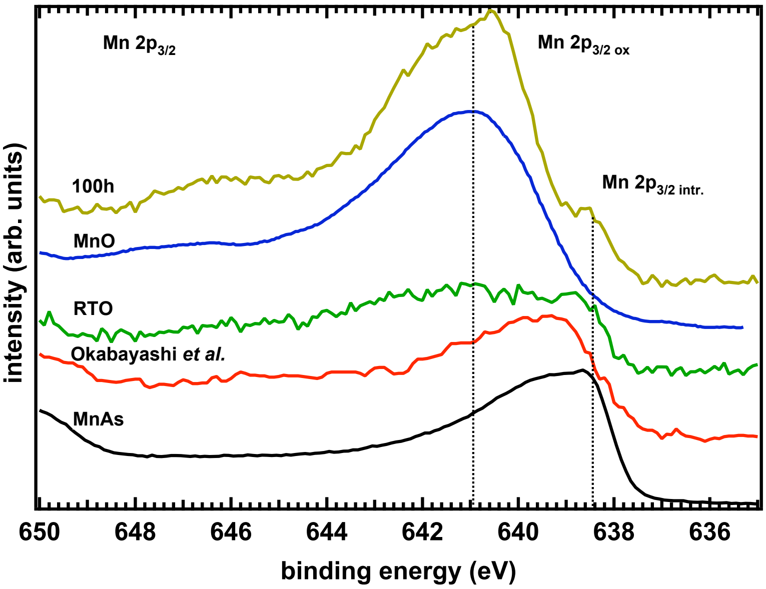

Figure 5.4: *Comparison of the Mn $2p_{3/2}$ core level spectra of (Ga,Mn)As sample, as-grown and annealed at 190°C for 100 h, with reference data of MnAs, MnO (data taken from Ref. 118), and (Ga,Mn)As (data taken from Ref. 166). All spectra were measured in normal emission geometry. It is obvious that the low BE peak shows great similarity with data on bulk MnAs and earlier results on (Ga,Mn)As. In contrast to this, the high BE peak coincides with the peak of divalent Mn^{2+} in MnO. Higher Mn oxidation states would show a considerably larger shift.*

in order to identify the valences of the various Mn species. The low BE feature in the Mn $2p_{3/2}$ spectra resembles strongly the spectrum of bulk MnAs and is, besides a shift of 0.4 eV, consistent to the XPS data on (Ga,Mn)As by Okabayashi and co-workers.[166] It is therefore attributed to bulk Mn, with its small BE reflecting the covalent bonding to As.

In contrast, the high BE peak reflects a strongly oxidized Mn species.[118] Together with its angle-dependence it can thus be assigned to a surface oxide without a doubt. The presented data are in contrast to an earlier report[177] which ascribed the *high* BE feature to Mn covalently bound to As. However, the reference data on MnAs bulk samples show that the *low* BE feature originates from Mn bound to As. Thus, the low BE peak is interpreted as due to emission from intrinsic Mn. Not only is the chemical environment of Mn in (Ga,Mn)As similar to that in MnAs. Additionally, it is precisely this peak which survives after chemical removal of the oxide layer by etching (*cf.* Sec. 5.2). The high BE feature has to be assigned to an oxide component, i.e., divalent Mn^{2+} as in MnO. No clear evidence is seen for higher oxidation states such as Mn^{3+} as in Mn_2O_3 or even Mn^{4+} as in MnO_2, which both would have a larger chemical shift relative to MnO by 0.5 eV and 1.0 eV,[178] respectively. The increase of the MnO-related peak upon annealing further shows, that the segregated Mn is almost exclusively oxidized to Mn^{2+}.

Complementary magnetometric measurements

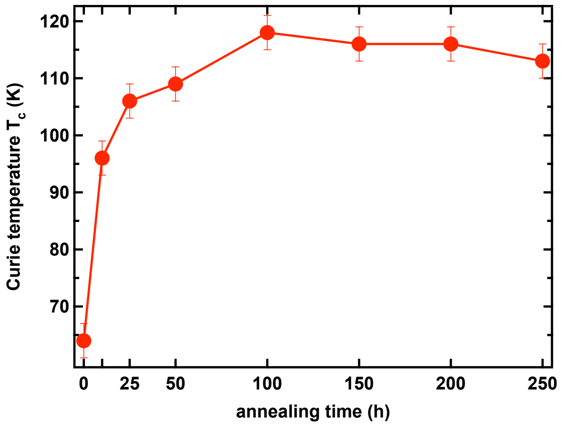

Figure 5.5: *Curie temperature as a function of annealing time as derived from SQUID measurements. The increase by thermal treatment is clearly visible. It reaches a saturation value of* 118 K *after* 100 h *of annealing. This is followed by a slight decrease what is attributed to the starting out-diffusion of substitutional Mn.*

Figure 5.5 shows the influence of the thermal treatment on the magnetic transition temperature and thereby correlates for one and the same sample the findings by HAXPES regarding Mn surface segregation and oxidation with the magnetic properties. In agreement with the literature,[94] T_c is significantly enhanced by annealing in air, for this sample from 64 K up to a maximum value of 118 K after 100 h annealing. By further annealing, T_c is slightly reduced, most likely due to the slow out-diffusion of Mn at substitutional sites which means a loss of magnetically active Mn, a reduction of the hole concentration, and hence, a drop of T_c. The initial increase of the magnetic transition temperature occurs much faster than the increase of the Mn concentration in Fig. 5.2 (b) & (c). This is simply due to the fact that SQUID measurements monitor an improvement of the magnetic response over the whole sample while the concomitant Mn diffusion appears in HAXPES only through an enhanced Mn concentration at the surface, i.e., with some delay. For the sake of completeness it shall be noted that the efficiency of the annealing depends on various factors such as temperature, film thickness—both kept constant in the present study—or the oxide layer itself.[4,94]

The results presented above give strong evidences that it is mainly interstitial Mn, which is affected by the thermal treatment. With the current resolution of 0.7 eV it is not possible to distinguish spectroscopically between interstitial and substitutional Mn. However, the covalently bound Mn on substitutional sites has a higher activation energy than Mn on interstitial sites. Therefore it is concluded that it is essentially interstitial Mn which accumulates at the surface upon annealing, whereas the substitutional Mn remains largely unaffected.

The subsequent oxidation of the segregated interstitial Mn leads to its passivation, as it cannot act as a hole-compensating donor anymore. The magnetometry data confirm the accompanying improvement of the magnetic properties by the annealing. These findings thus corroborate the earlier suggested mechanism[51] for an improvement of the Curie temperature by annealing in oxidizing atmosphere and give a first quantitative estimation of the process. However, the loss of Mn for longer annealing times is not yet fully understood. It appears that for very long annealing times also substitutional Mn seems to contribute to the segregation process despite its higher activation energy.

5.2 Manganese valency in (Ga,Mn)As

After investigating the Mn interstitial segregation upon *ex situ* annealing the goal of this section is to eliminate the oxide components and obtain intrinsic, bulk sensitive core level spectra. The oxide component, especially in the case of Mn, hinders the identification of the true core level line shape (*cf.* Fig. 5.3).

In order to obtain intrinsic, bulk sensitive information, the samples from the previous section (as-grown and annealed) have been investigated after etching by either hydrochloric or sulphuric acid as shown in Sec. 4.3. Since only the line shape and the stoichiometry are of interest, no further treatment such as ion-milling or *in situ* tempering have been conducted. The high volume sensitivity and angle integrated acquisition mode lead to minimized contributions from surface inhomogeneities. The central aims were to observe the intrinsic line shape of Mn $2p$ in (Ga,Mn)As and to identify possible changes in the stoichiometry.

The experimental setup and samples are identically to the previous section. In order to quantify differences in substitutional and interstitial Mn, an as-grown and an annealed sample (100 h) were etched with either hydrochloric (HCl) or sulphuric (H_2OS_4) acid. The etchants were rinsed over the sample for 1 min followed by a 1 min rinse of deionized water to solve acid anions, potentially left on the surface. The etching was performed in inert Ar atmosphere and exposure to air was less than five seconds during the mounting of the sample in the UHV apparatus. Data on the stoichiometry are compared to the results in the previous section.

As- and Ga-oxides and stoichiometry

First, the elements of the host matrix are addressed in order to investigate the success of the cleaning procedure. For As, Fig. 5.6 shows that the etching with both HCl (dashed lines) and H_2SO_4 (dotted lines) is capable to remove all oxides from the surface. The prominent oxide shoulder around 1325.6 eV in the spectra of the untreated samples (solid lines) is completely suppressed. Ga (not shown) behaves identically. Even the thicker oxide layer in the case of the annealed sample is entirely solved. However, if the spectra are compared to the *in situ* filed GaAs reference sample (blue solid line), a small but

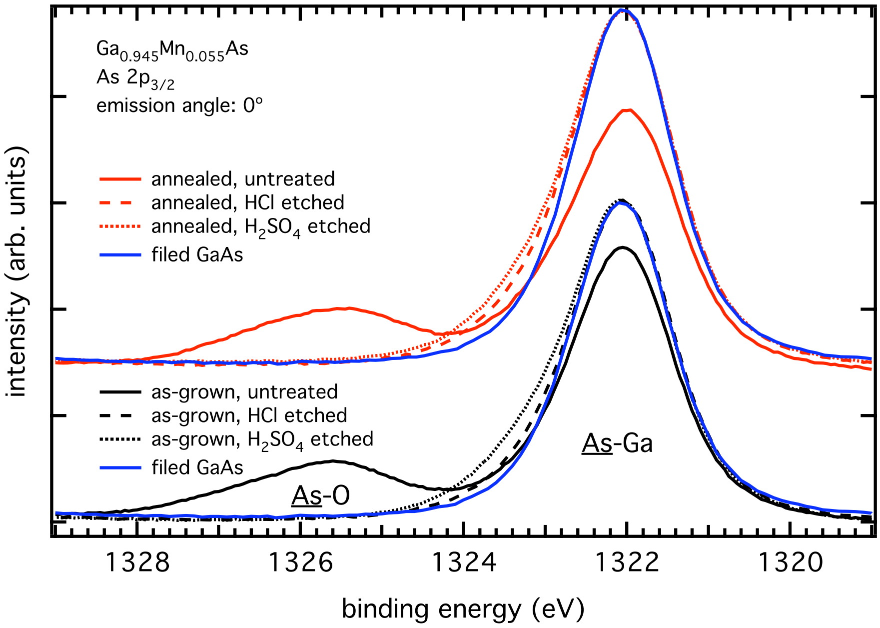

Figure 5.6: *As $2p_{3/2}$ in the course of annealing and wet-chemical etching with hydrochloric (dashed line) and sulphuric (dotted line) acid, measured with HAXPES ($h\nu = 4.5\,\text{keV}$). The wet-chemical etching leads to a complete suppression of the oxide component of both as-grown and annealed samples. However, a small asymmetry at higher binding energies is observed in any case, as can be seen by comparison to the intrinsic spectrum of a* in situ *filed GaAs sample (blue line).*

detectable asymmetry in the As $2p_{3/2}$ line shape to higher binding energies is observed. Based on the findings in Sec. 4.3 this asymmetry is interpreted as residual elemental As (As^0) not affected by the etching. As the issue of As^0 has been addressed in Sec. 4.3 and it would only bias the stoichiometric analysis, the contributions of elemental As have been subtracted from the spectra in the upcoming analysis. This is readily performed by fits as elemental As has a chemical shift of $\approx 1.0\,\text{eV}$ due to the less screened core potential.[171]

As appears from the stoichiometric data summarized in Tab. 5.1 and plotted in Fig. 5.7 no significant changes in the stoichiometry are observed, i.e., the stoichiometry is essentially independent of the detection angle, after the subtraction of the As^0 contributions. The data for the as-grown sample in panel (a) of Fig. 5.7 basically scatter around the nominal ratio of 1.06 given by the chemical formula $\text{Ga}_{0.945}\text{Mn}_{0.055}\text{As}$ (red dashed line). The variance of the HCl etched sample (triangles) is higher than for the untreated sample (circles) and the H_2SO_4 etched sample (squares), however, not significant within the error bars. The data of the annealed sample in panel (b) are in even better accordance to the nominal value.

Concerning other contaminations both acids work comparably well. The core levels of both C and O are drastically reduced in intensity, almost down to the detection limit.

Table 5.1: *Results of the stoichiometric analysis of the as-grown samples, untreated, HCl and H_2SO_4 etched, depending on the angle of detection. Contributions of elemental As to the total As content have been taken out.*

	0°	25°	40°	60°
as-grown				
non-etched	1.09	1.04	1.11	1.18
HCl etched	1.08	1.23	1.04	0.86
H_2OS_4 etched	1.03	–	1.05	1.18
annealed				
non-etched	1.09	1.06	1.05	1.13
HCl etched	1.09	–	1.07	1.30
H_2OS_4 etched	1.06	–	0.95	0.97

The absence of oxide components suggests that the remaining O signal originates from water left on the surface by the rinsing process. Thus, the oxygen is not chemisorbed but loosely physisorbed. For carbon, it has been shown that wet-chemical etching can hardly deal with it.[12] Further cleaning steps such as ion-milling described in Sec. 4.2 have to be used to remove all the carbon. Similar can be said for the remaining oxygen contaminations.

Furthermore, the rinse with deionized water showed again to be successful. No signal of neither chlorine nor sulphur were detected indicating that no anions remained stuck on the surface.

In summary, the findings of Sec. 4.3 have been confirmed by HAXPES. The entire oxide layer, even of intentionally oxidized samples (annealed), is solved by the etching. All oxide components of the As and Ga core levels are suppressed. Further C and O contaminations, not covalently bound to the surface, are pushed down to the detection limit. Besides elemental As, which is easily dealt with by fits, the stoichiometry is not altered, but the probed depth exhibits the nominal As-to-Ga ratio of 1.06.

Mn concentration and valency

Now, the main interest is turned to manganese. In regard to the core level line shape, everything stated for the As and Ga also holds for Mn. As can be seen in Fig. 5.8, HCl (and analogously H_2SO_4) completely remove the higher binding energy peak, even for the heavily oxidized annealed sample. After the etching only the low BE peak survives. Furthermore, the pronounced angle dependence of the spectral line shape disappears upon etching. Spectra taken in normal emission and under grazing emission are superimposable. This indicates that only one Mn species is present in the entire probed depth.

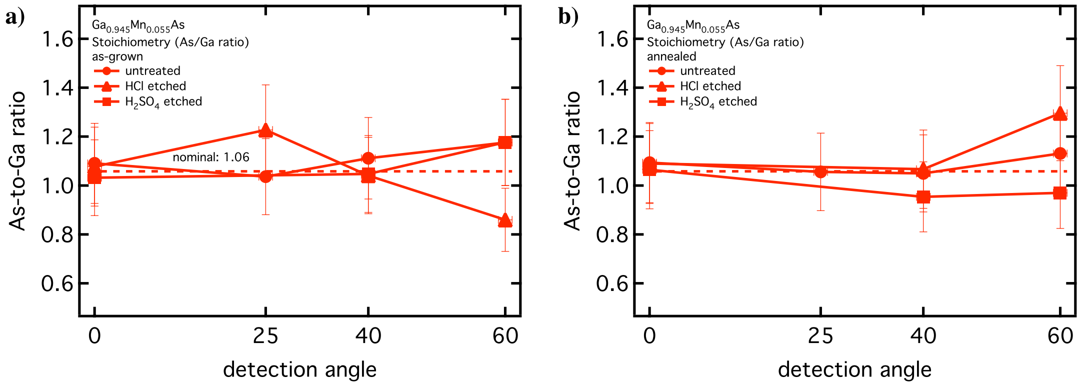

Figure 5.7: *Plot of the stoichiometric data (As/Ga ratio) of Tab. 5.1, panel (a): as-grown sample, panel (b): annealed sample. All sample show, within the error bars, the nominal As-to-Ga ratio of* 1.06 *given by the chemical formula* $Ga_{0.945}Mn_{0.055}As$*. Furthermore, no pronounced angle dependence is observed.*

The Mn concentration determined from the Mn $2p_{3/2}$ and the As $2p_{3/2}$ (Tab. 5.2 and Fig. 5.9) agrees, independently of the probed depth, excellently with the nominal value of 5.5 % for the as-grown/untreated [open circles in panel (a) of Fig. 5.9] and as-grown/HCl etched sample (open triangles). The sulphuric acid shows slightly lower values.

Concerning the annealed sample [*cf.* open circles in Fig. 5.9 (b)] the dramatically increased Mn concentration has been exploited in the previous section, i.e., segregated Mn_{int}. The dissolving of the oxide layer by acids leads to a tremendous decrease even below the value of the as-grown sample. For the annealed sample, hydrochloric (open triangles) and sulphuric (open squares) acid result in a comparable loss of Mn, again independent of detection angle.

As the chemical environment of an atom is reflected in the core level spectra the Mn valency can be identified. In the case of Mn, two different species have been identified in Fig. 5.8. As shown in the previous section and illustrated in Fig. 5.10, the high BE peak originates from MnO, i.e., Mn in an ionic bonding to O (red dotted line).[118] In this case, Mn is in $3d^5$-configuration since its two $4s$-electrons have been transferred to the more electronegative ligand. The intrinsic Mn line shape (and valency), reflecting (Ga,Mn)As has been identified to be located at lower binding energies which is in contradiction to previous results.[177] This is in particular supported by the excellent agreement of the etched-spectra to the pioneering works of Okabayashi *et al.*[166] on *in situ* grown and measured samples (red solid line in Fig. 5.10). Furthermore, it shows a great similarity to the Mn $2p$ spectrum of MnAs (black solid line in Fig. 5.10). For MnAs, in turn, it has been shown[179] that there Mn is far from being in an ionic d^5-state. The naive assumption here would be that Mn is in a $3d^4$-configuration [same as in (Ga,Mn)As, without the bound hole]. However, if this is true the Mn $2p$ spectrum would be shifted to even higher binding energies due to the less screened core potential, as is the case

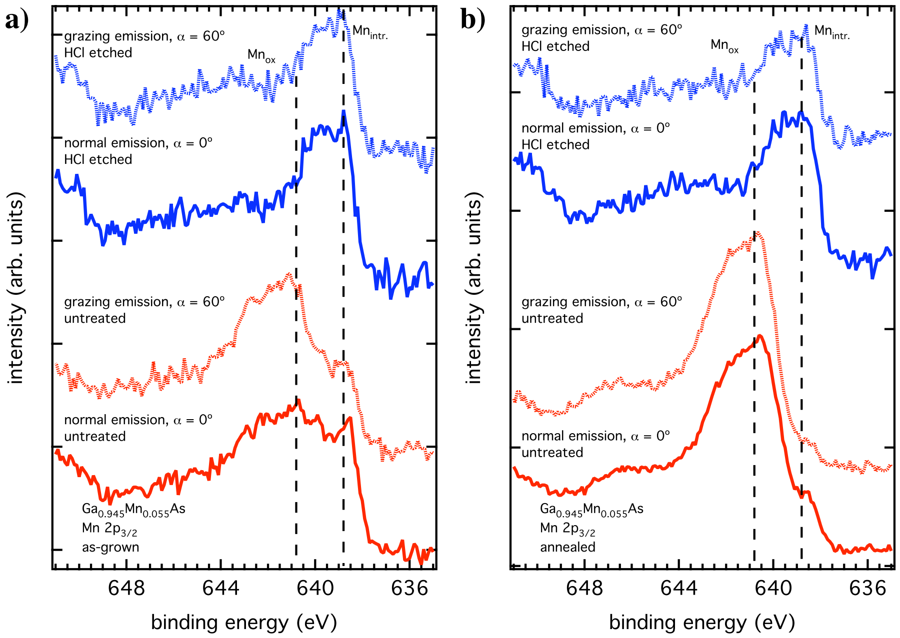

Figure 5.8: *Mn $2p_{3/2}$ core level spectra of as-grown (panel a) and annealed (panel b) (Ga,Mn)As both untreated (red lines) and HCl etched (blue lines). The line shape of the oxidized samples was discussed previously. The etching leads to a complete suppression of the high BE peak and the spectra are dominated by the low BE peak. Furthermore, the angle dependence of the line shape is absent in etched samples. This shows that a single Mn species is present within the entire probed depth. Sulphuric acid (not shown) shows identical results in regard to the line shape.*

in the MnO_x-series.[178] Hence, the d-electron count is most likely larger than five, as is also predicted by theoretical calculations which find an occupancy between $6-7$.[179] Additional evidences for a more than half-filled Mn $3d$-shell come from x-ray absorption spectroscopy in magnetic circular dichroism (XAS-MCD) results.[69] Furthermore, the huge difference in electronegativity between As and O (2.18 and 3.44 in Pauling notation) makes a picture of a complete electron transfer most unlikely. Therefore, Mn has to be in a much more covalent bonding to As. It is therefore conclude that the naive ionic picture of Mn being in a $3d^5$-configuration with a loosely bound or ionized hole[48,68] is oversimplified.

Unfortunately, it is not possible to discriminate spectroscopically between contributions from substitutional and interstitial Mn in the $2p$-spectra. This can be seen if one compares the Mn $2p$-spectra of the annealed/HCl etched sample (Mn content: 4.5 %) with the one of the as-grown/etched sample (Mn content: 5.8 %). In the first one, the segregated and passivated (by oxidation) Mn_{int} has been washed away by the acid and the spectra should exclusively resemble Mn_{sub}, assuming that the segregation process is completed. However, the spectra of as-grown/HCl etched and annealed/HCl etched are quite alike (*cf.* Fig. 5.8). On the other hand, the difference in the Mn content (1.3 %)

Table 5.2: *Mn concentration of the as-grown samples, untreated, HCl and H_2SO_4 etched, depending on the angle of detection. Contributions of elemental As to the total As signal have been taken out.*

	0°	25°	40°	60°
as-grown				
non-etched	5.6	6.7	5.2	4.5
HCl etched	5.8	4.7	5.7	4.2
H_2OS_4 etched	4.4	–	4.0	4.4
annealed				
non-etched	13.6	13.4	14.7	19.2
HCl etched	4.5	–	3.5	2.9
H_2OS_4 etched	3.6	–	4.0	3.5

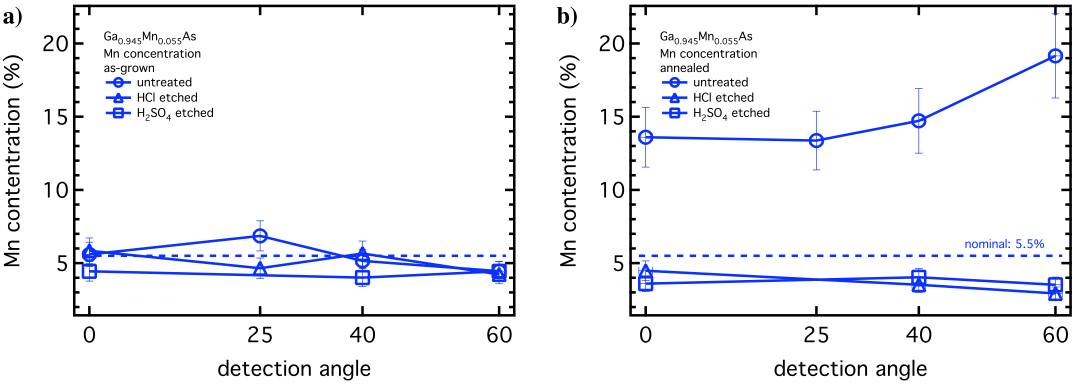

Figure 5.9: *Plot of the stoichiometric data (Mn concentration) of Tab. 5.2, panel (a): as-grown sample, panel (b): annealed sample. For details, see text.*

represents the loss of Mn_{int}. Hence, the Mn_{int} concentration in the as-grown sample relative to the total Mn signal should be:

$$Mn_{int} = \frac{Mn_{tot} - Mn^{*}_{tot}}{Mn_{tot}} \tag{5.1}$$

where Mn_{tot} and Mn^{*}_{tot} are the manganese contents in the as-grown/etched and annealed/etched sample, respectively. Even though the Mn content shows some variations with probing depth, the difference between the as-grown/HCl etched and annealed/HCl etched sample is nearly constant. A percentage value of 23 % suggests that at least one out of five Mn atoms in the as-grown/etched sample is removed after the annealing and etching. Thus, one fifth to one fourth of the Mn atoms in the as-grown samples reside on interstitial position. These values is in surprisingly good agreement with other reports.[21,180] The same analysis of the H_2SO_4 sample yields a value of 19 %.

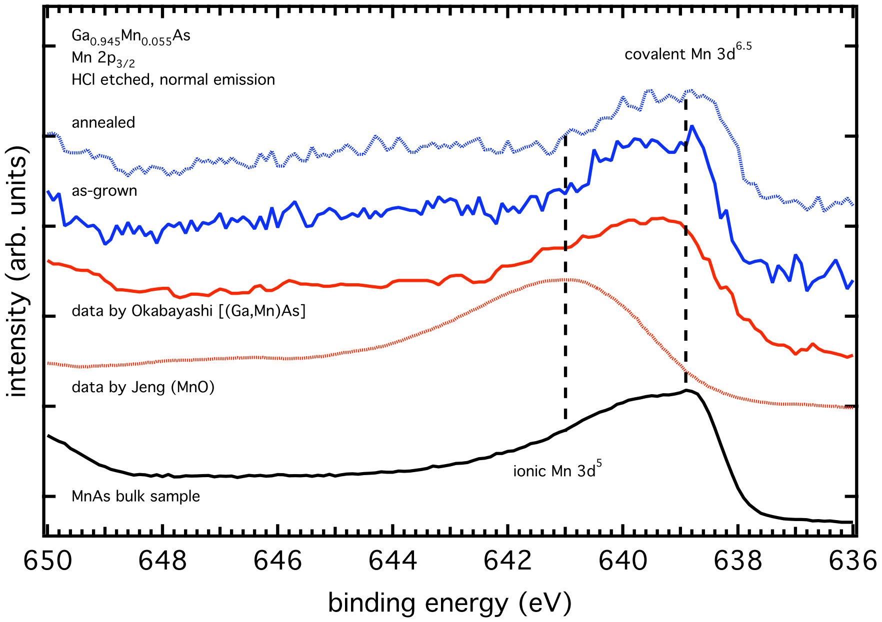

Figure 5.10: *Comparison of the Mn $2p_{3/2}$ core level line of the as-grown/etched and the annealed/etched sample to reference data. The position of the main peak is identical to the covalent $3d^{6.5}$-configuration in MnAs. An ionic $3d^5$-configuration would yield a spectrum comparable to the data on MnO. Note the remarkable similarity of the etched and the* in situ *data of Okabayashi and co-workers. Reference data from Okabayashi* et al.[166] *and Jeng* et al.[118]

However, it must be stated that these values have to be handled with care. As shown in Fig. 5.9 for the As-to-Ga ratio, contributions of elemental As have been eliminated by fitting. The ratio is equal to the expected value of 1.06. Thus, major contributions of As^0 from the surface can safely be excluded. Nevertheless, only the difference between as-grown/etched and annealed/etched Mn contents from the spectra taken in normal emission are considered, as the bulk sensitivity further ensures minimal contributions of the surface. Furthermore, only the hydrochloric etched samples are taken into account. For sulphuric acid, the Mn content of the as-grown/etched sample is significantly lower compared to the other two samples [panel (a) of Fig. 5.9]. The origin of this discrepancy is unclear, although it has been reported that in the case of MnAs thin films, wet-chemical preparation with H_2SO_4 leads to a selective etching of Mn.[171,181] Notwithstanding, the qualitative picture is clear and considering the high overall Mn content of 5.5 %, a value of one $19-23\,\%$ of Mn_{int} in as-grown samples is not unrealistic.

The stoichiometric analysis already indicates that the etching does not have major effects on the topology. In contrast to the conventional procedure of combining an etching agent, an oxidizing agent, and water, only highly concentrated acids and water have been used in the present case. The aim was to keep the etching rates as low as possible, which are known to depend crucially on the composition of the etching-

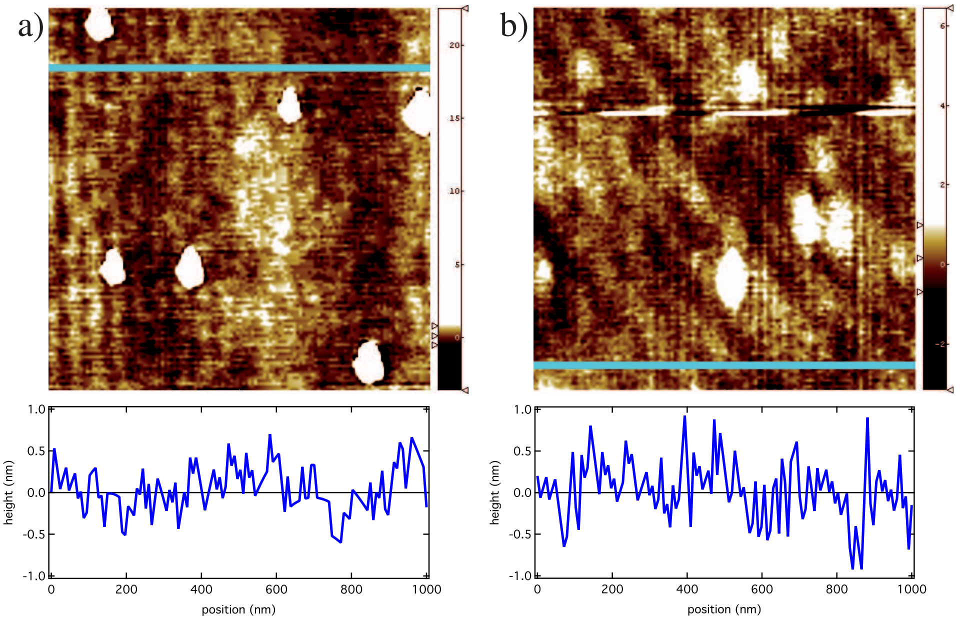

Figure 5.11: *AFM images of an as-grown (panel a) and an as-grown/H_2SO_4 etched (panel b) (Ga,Mn)As. The lateral scale is 1 μm by 1 μm. The line profiles at the bottom are taken along the turquoise lines in the pictures. Within the resolution no increasing surface roughness can be seen. In either case the maximal peak-to-peak height is around 1.5 nm. The large bright clusters are probably α- or/and β-point defects since Ga-splitting are much larger.*[41]

solution.[32] Indeed, the single observation that after 60 s of etching a manganese signal in the same order of magnitude as before was measured shows clearly that the etching was smooth enough not to solve the entire 60 nm thick film. It appears that for both the as-grown and the annealed sample the acids do only solve the As and Ga oxides at the surface via complex formation, while leaving the (Ga,Mn)As intact.

In order to confirm the surface morphology, AFM images have been taken after the HAXPES measurements. Figure 5.11 gives an 1 μm by 1 μm pictures of an as-grown/untreated [panel (a)] and as-grown/sulphuric acid etched [panel (b)] sample. As can be seen clearly, the surface roughness is not significantly enhanced by etching. In either case, the maximal peak-to-peak height is approximately 1.5 nm. This means that the etching preserves the surface morphology. The bright spots are natural defects, in particular α- and β-type oval defects, originating from thin film/substrate contaminations.[41] Ga-splitting are not to be expected in the images since they are usually much larger.

In conclusion, the results of the HAXPES-experiments on etched samples yield three important findings. First, etching with highly concentrated acids enables the observation of intrinsic Mn 2p properties with surface sensitive methods of samples, which have been exposed to air. Second, the Mn valency in (Ga,Mn)As is far from the simple Mn^{2+} (d^5-configuration) scenario as commonly assumed in both experiments and theoretical calculations. Rather, a covalent bonding of Mn as in MnAs is found. Unfortunately, no spectroscopic discrimination between Mn_{int} and Mn_{sub} is possible. Though, a tentative quantification of the Mn content shows that at least one out of five Mn atoms in as-grown samples is of interstitial nature.

5.3 Resonant photoemission spectroscopy on (Ga,Mn)As

In order to gain a direct probe of the electronic structure near the Fermi edge resonant photoemission spectroscopy (ResPES) experiments have been performed on (Ga,Mn)As. ResPES allows for a identification of the element-selective contributions of a single constituent to the overall electronic structure (*cf.* Sec. 3.1.2). In particular, the Mn $3d$-states in the VB are of utmost interest, since their correlation governs the rich physics of (Ga,Mn)As.

The experiments at the Mn L_3-edge ($2p \rightarrow 3d$ excitation) at $h\nu \approx 640\,\mathrm{eV}$ were performed at the beamline UE56-2/PGM-2 at the BESSY storage ring, Berlin. Calibration of the energy scale and determination of the resolution have been done by using a Ag sample. The overall energy resolution was determined to be 0.5 eV.

Samples were nearly identical to the ones in the HAXPES study. Two different samples with Mn contents of 3.5 % and 4.5 % and nominal thicknesses of 480 nm and 70 nm, respectively, grown at 270°C, were measured. Spectra were recorded for as-grown and optimized samples, annealed according to the protocol in the previous two sections.

Since experiments in the soft x-ray regime are more surface sensitive and possible surface states may greatly affect the line shape, the sample surfaces were treated in the manner described in Sec. 4.4. In brief, the samples were wet-chemical etched *ex situ* by HCl followed by two cycles of ion-milling and tempering *in situ*. Blurry LEED patterns were observable indicating a sufficient success of the cleaning.

The first breakthrough experiments by Okabayashi and co-workers[182] on (Ga,Mn)As by ResPES have been performed on as-grown samples measured *in situ* after the growth (*cf.* Fig. 5.12, lower panel, black dotted line). Their results have provided a benchmark for all theoretical calculations. Not only their absolute value for the *p*-*d* interaction J_{pd} determined from an analysis of the experimental data with a configuration-interaction (CI) cluster model,[166] but also the position of the Mn $3d$ main peak has spurred many theoretical calculations. The results led to the finding that the on-site Coulomb repulsion U between two holes on the same Mn site has to be considered in order to correctly predict the main centroid at around 4.5 eV below E_F.[46,184] Both GGA[75,91] and LDA[61,62,89] calculations without a Hubbard U result in a main peak located around 2 eV below E_F.

The results of Okabayashi *et al.* on as-grown samples at the Mn M-edge ($3p \rightarrow 3d$ excitation, $E_{ph} \approx 50\,\mathrm{eV}$) have been confirmed by Rader *et al.*[167] at the Mn L-edge, who also investigated as-grown samples (*cf.* Fig. 5.12, lower panel, red dash-dotted line).

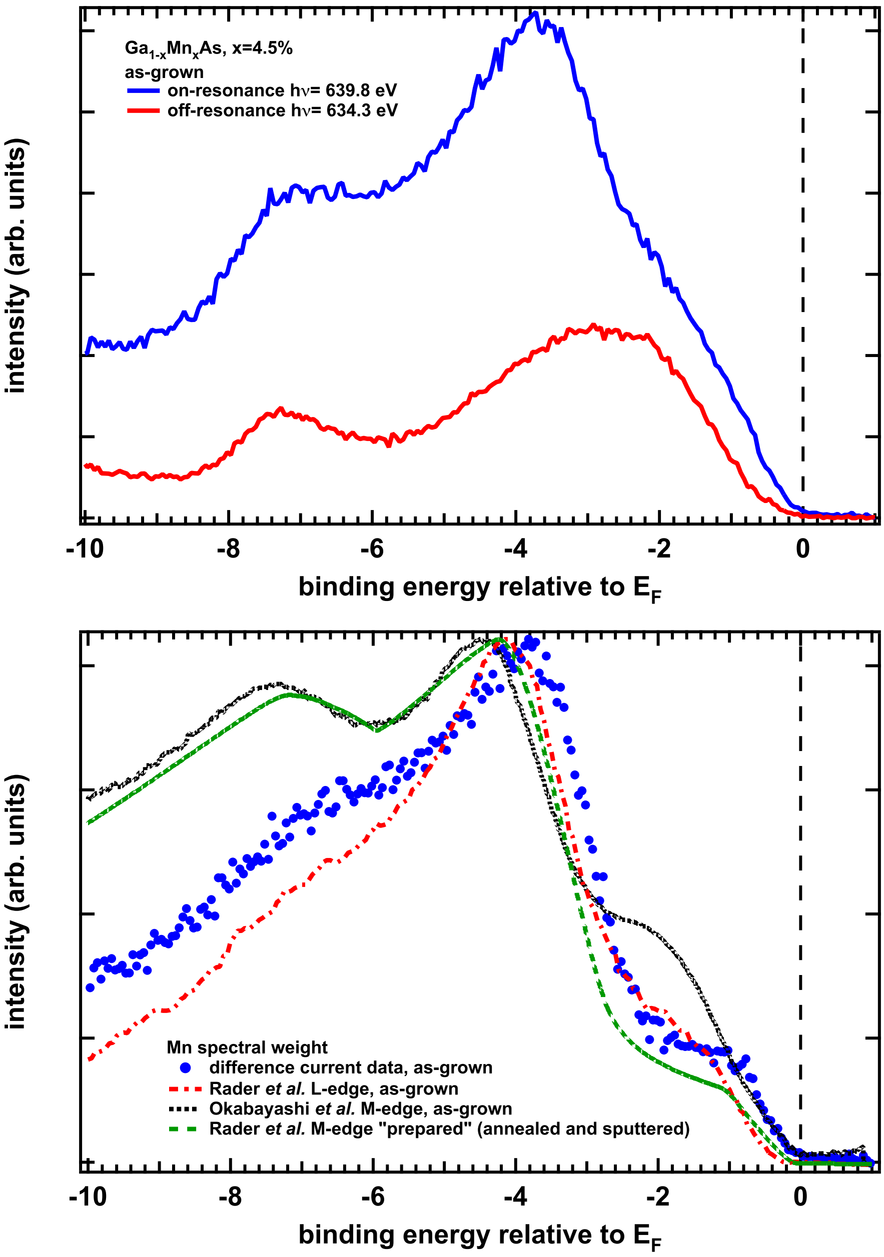

Figure 5.12: *Upper panel: VB spectra of a as-grown (Ga,Mn)As sample with* $x = 4.5\,\%$ *recorded at two different photon energies. Red line: with a pre-edge energy of* $h\nu = 634.3\,\mathrm{eV}$*, blue line: with the on-resonance energy of* $639.8\,\mathrm{eV}$*. The Mn partial density-of-states (PDOS) is obtained via subtraction (blue symbols in the lower graph). Also shown in the lower graph, previously reported Mn PDOS results. Data from the literature were recorded at the Mn* M*-edge (black dotted and green dashed line)*[182,183] *and* L*-edge (red dash-dotted line).*[167] *The current data of the as-grown sample are in general agreement with previous results.*

An other approach was chosen by Åsklund and co-workers,[185] who obtained the partial density-of-states (PDOS) by subtracting the VB of a pure GaAs sample from the VB of various as-grown (Ga,Mn)As samples. Their results indicate a lower binding energy of the Mn main peak at around $-3.4\,\mathrm{eV}$, in contrast to the $\approx -4.2\,\mathrm{eV}$ from the ResPES experiments. Also, a value of $-3.8\,\mathrm{eV}$ has been reported,[186] also determined by means of ResPES at the L-edge.

Despite those primary works the effects of an improvement of the electronic and magnetic properties upon annealing have just recently been addressed.[183] The recent results of Rader *et al.*[183] on annealed and sputtered (Ga,Mn)As at the Mn M-edge did not show any significant changes caused by the optimization of the electronic and magnetic properties. The logical consequence was that conclusions drawn earlier for not optimized samples are still valid.

Nonetheless, it is still of outmost importance to check, if the results and conclusions obtained in the early stage of (Ga,Mn)As growth and preparation also hold for samples with apparently better quality (measured by a high ratio of substitutional to interstitial Mn). It might be that the previous results were mainly affected by defects such as Mn_{int}.

Concerning the substitutional-interstitial issue, ResPES provides another advantage. It is hard to distinguish between interstitial and substitutional Mn when doing core level PES.[97,166] The chemical shift between these two species is hardly resolvable by XPS. Fortunately, they are supposed to have different spectroscopic fingerprints in their $3d$ PDOS which was shown in theoretical calculations.[49,52] The major part of the contribution of interstitial Mn is located in an impurity band at $-1.2\,\mathrm{eV}$[49] or $-0.5\,\mathrm{eV}$[52] below E_F. This PDOS is also quite robust under the inclusion of an on-site repulsion U whereas the substitutional Mn shows a shift of the main spectral weight to higher binding energies known from previous calculations.[46,184]

Figure 5.12 illustrates how the Mn PDOS is obtained from the ResPES data. The upper panel gives pre-edge (off-resonance) and on-resonance spectra. By subtraction, the Mn PDOS is obtained (blue dots in lower panel). Also shown in the lower panel are the results reported in the literature.[167,182,183] The results resemble the previous data of as-grown (Ga,Mn)As samples at the L-edge by Rader *et al.*[167] quite well. Basically, a three peak structure can be identified as in Ref. 167. Also, the relative intensities are comparable and the same slight difference to the as-grown M-edge data of Okabayashi *et al.*[182] can be seen. Data recorded in the VUV regime show, in general, a more pronounced structure at around $-1\,\mathrm{eV}$, and also the shoulder at $-7\,\mathrm{eV}$ is mildly higher. Furthermore, the position of the main peak in the current data is shifted to lower binding energies ($-3.8\,\mathrm{eV}$), comparable to the as-grown data of Adell *et al.*[186] The data in Fig. 5.12 do not show considerable intensity at the Fermi edge.

Figure 5.13 shows a comparison of the Mn $3d$ PDOS for two doping levels (black: 3.5 %, red: 4.5 %). Within the experimental accuracy no significant change can be observed. The slight deviations are surely too small to draw any final conclusion. Possible changes in the PDOS as a function of doping are therefore not discussed. Further investigations in a wider doping range have to be conducted in order to reveal a definite trend.

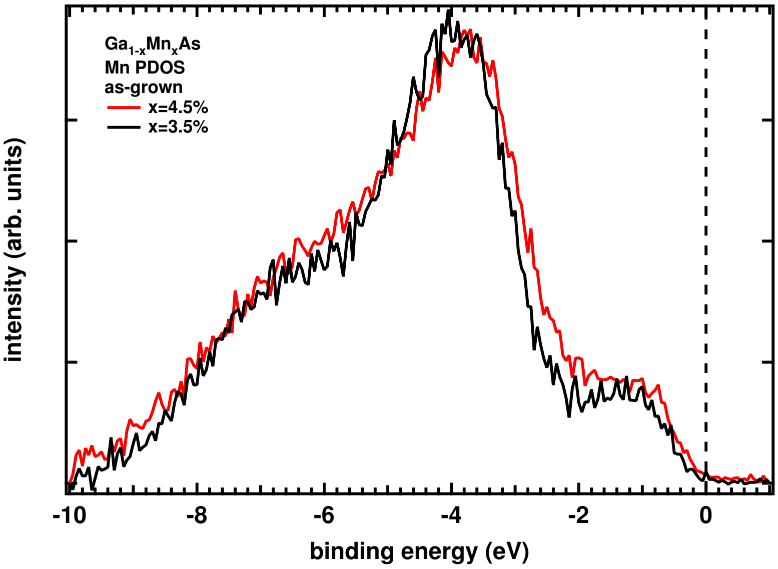

Figure 5.13: *Mn 3d partial density-of-states (PDOS) in (Ga,Mn)As obtained by ResPES at the Mn L-edge for two different dopings (3.5 % and 4.5 %). No significant changes between the two doping levels can be seen.*

In contrast to the doping, dramatic changes in the Mn PDOS can be seen upon annealing. Figure 5.14 compares the PDOS of the 3.5 % sample both as-grown and annealed in air for 100 h at 190°C. In order visualize the changes, also the plain difference of the two spectra is shown as blue line. Note, that the two PDOS curves have been shifted in y-direction for the sake of clarity. The dashed line parallel to the abscissa gives "zero" counts.

As is apparent, the data are in sharp contrast to the M-edge data on annealed samples, reported by Rader and co-workers (*cf.* red dash-dotted line in lower panel of Fig. 5.12).[183] The spectral shape changes dramatically upon annealing. The satellite shifts to higher binding energies from $-6.7\,\text{eV}$ to around $-7.1\,\text{eV}$ and becomes much sharper. Oppositely, the main centroid shifts to lower energies (from $-3.8\,\text{eV}$ to $-3.4\,\text{eV}$) and an additional spectral weight becomes apparent at around $-2.2\,\text{eV}$.

In the light of the results presented above, a detailed analysis of the spectra by means of CI calculations seems not to be feasible. None of the previously reported CI calculations showed significant spectral contribution at around $-2.2\,\text{eV}$. It is therefore not possible to reproduce the experimental results with such an ansatz. The results are thus only discussed qualitatively. The apparent sharpening of the $-7.1\,\text{eV}$ peak, as well as both structures around it ("negative" peaks at $-8.4\,\text{eV}$ and $-5.0\,\text{eV}$ in the difference spectrum, blue line in Fig. 5.14) cannot definitively be ascribed as arising from certain processes. CI-calculations[182] show that the intensity in this region originates either from the unscreened $3d^4$ or the double-screened $3d^6\underline{L}^2$ final-state. Most likely, an increase or

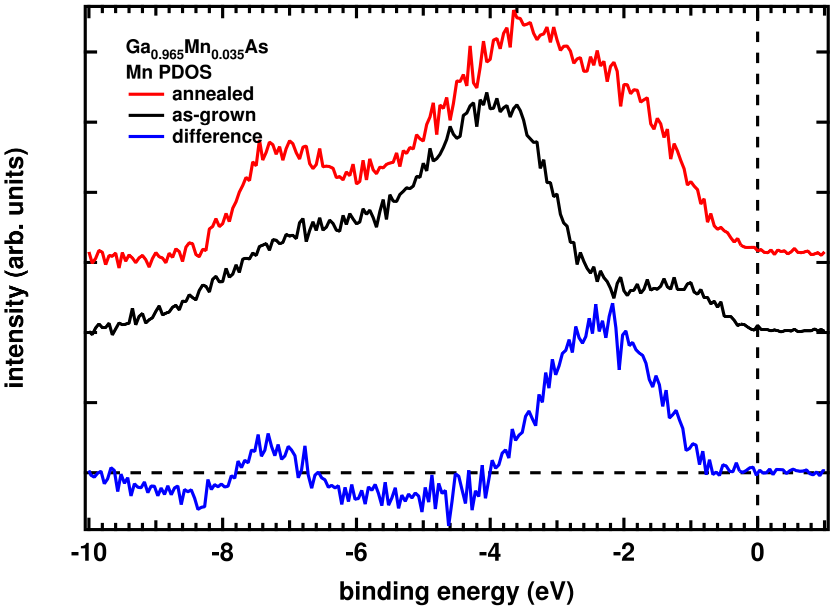

Figure 5.14: *Mn 3d partial density-of-states (PDOS) obtained by ResPES at the Mn L-edge for an as-grown (black line) and an annealed (red line) sample with a nominal Mn concentration of 3.5 %. Dramatic changes in the Mn PDOS can be seen upon annealing. In order to visualize the change, the plain difference between the two spectra is plotted as blue line.*

a decrease of the local-screening probability cannot be related to the annealing due to the local character of the screening process (*cf.* Sec. 3.2.2). Rather, minimal changes in the higher binding energy tail of the background due to secondary electrons are made responsible for those slight differences. In any case, the peak around −7.1 eV is not to be mistaken for the −7 eV peak in Ref. 187. There, contribution from the GaAs X_3 critical point of the host matrix are observed, which are absent under resonant conditions.

The most pronounced difference between the present data and the data on annealed samples from Rader *et al.* is the additional intensity around −2.2 eV. As described above, the CI-calculations for a $MnAs_4$-cluster with a Mn $3d^5$-configuration predict no spectral intensity in this region. These calculations, even though being able to describe the spectra of as-grown samples well, are not capable to reproduce the spectra of annealed samples in Fig. 5.14. It seems that the annealing leads to the emergence of another Mn valency. The suppression of the $3d^5$-contribution to the spectra might be linked to the loss in interstitial Mn. As has been shown in the previous section, it is present in a significant amount in as-grown samples, has also a $3d^5$-configuration, and is the only Mn species that is affected by the annealing. Without further theoretical investigation, a definitive assignment of the emerging spectral weight to a specific Mn valency is not possible, nevertheless, the structure gives strong evidences that valence hybridization is an inherent property of (Ga,Mn)As.

Finally, the hump around $-1.2\,\text{eV}$, in particular present in the data of the as-grown sample in Fig. 5.13 shall be addressed. Theoretical calculations[49] suggest that the main spectral contribution of interstitial Mn is located $-1.2\,\text{eV}$ below E_F. However, the difference spectra of as-grown and annealed samples does not show a distinct peak at $-1.2\,\text{eV}$. This suggests, that this peak is also present in the annealed sample, although masked by the main structures. Its intensity is nearly unchanged, which rules out the possibility that it is a fingerprint for Mn_{int}, as the annealed sample is supposed to be free of interstitial Mn. Obviously, interstitial Mn has negligible contributions to the spectra in this energy region.

Furthermore, none of the PDOS spectra show significant intensity near the Fermi edge. Angular-resolved PES (ARPES) measurements, however, showed nondispersive states $0.5\,\text{eV}$ below E_F, which where induced by Mn.[188] This impurity band has caused a lot of debate, in particular if it is of substitutional or interstitial nature. On the one hand, it was seen as a prove for the double-exchange picture, which explicitly requires an impurity band formed by *substitutional* Mn (*cf.* Sec. 2.2.3). On the other, theoretical calculations[52] predict, that the main spectral contributions of interstitial Mn is not at $-1.2\,\text{eV}$, but at $-0.5\,\text{eV}$, and the experimentally observed impurity band thus formed by *interstitial* Mn. It is therefore not an intrinsic property of (Ga,Mn)As and no prove for the IB – DE picture. Unfortunately, this issue cannot be addressed with the current data set due to the low count rates near E_F.

Now, the question arises, what causes the differences of the present data to the results of Rader *et al.*[183] which have also been obtained on annealed samples. Since the data of the *ex situ* and *in situ* treated as-grown sample are in absolute agreement with all previous reported results and both the annealing and cleaning procedures have been investigated in detail, the present results are believed to reflect the intrinsic electronic structure of annealed (Ga,Mn)As thin films. Technically, there are only two differences between the current L-edge results and the M-edge results of Rader and co-workers in Ref. 183 on annealed samples, i.e., details in the cleaning procedure and the excitation energy. It is therefore imaginable that the disagreement is caused by residual contaminations or by the increased surface sensitivity of the experiments of Rader and co-workers at the M-edge, The present ResPES experiments at the L-edge are still relatively surface sensitive, however, the probed depth is significantly larger than at the M-edge ($E_{ph} \approx 50\,\text{eV}$, *cf.* Fig. 3.10). Surface sensitivity and insufficient cleaning might have led to a pollution of the results in Ref. 167 by residual or replenished Mn_{int} at the surface.

For the data presented here, contributions of surface effects or residuals on the surface can, in addition to the reasoning in Chap. 4, be excluded by the following considerations. According to Ref. 187, a peak at $-5.2\,\text{eV}$ is a signature of segregated, elemental Mn (Mn^0) at the surface. Since this is close to the minimum at $-5.8\,\text{eV}$ of the data shown above, the presence of Mn^0 can safely be ruled out. It has also been reported that annealing may lead to the formation of MnAs nanoclusters in the hypothetical zinc blende structure.[183,189] Such nanoclusters are characterized by a main centroid around

4 eV, i.e., at lower binding energies than as-grown (Ga,Mn)As.[186] However, at this energy no changes upon annealing are observable (*cf.* difference spectra in Fig. 5.14), and the main centroid of the Mn 3*d* PDOS shifts to even lower binding energies. Hence, MnAs nanoclusters are also ruled out, contrary to the argumentation in Ref. 183.

Summarizing the data presented above, dramatic changes in the Mn 3*d* PDOS upon post-growth annealing are observed, at variance to recent results in the literature.[183] This proves that the electronic structure of the VB is greatly affected by annealing, making previous results on as-grown samples partially questionable. A determination of concrete values, e.g., for J_{pd} or the exact Mn 3*d*-electron count, would require extensive theoretical calculations, since common approaches fail to explain the observed line shape. Nevertheless, a qualitative discussion of the data provides the following findings.

The electronic structure after annealing differs significantly from the pure Mn $3d^5$ picture. All previous reported data have consistently been explained by an ionic Mn $3d^5$ configuration on substitutional sites. The greatly altered line shape of the Mn 3*d* PDOS after annealing suggests, that earlier results may have suffered from unwanted contributions of interstitial Mn. As shown in the previous sections, it is present in as-grown samples to a sizeable amount. Since it is in $3d^5$-configuration after donating its to 4*s* electrons, its removal by the post-growth annealing and surface preparation would lower the $3d^5$-contribution to the PDOS. With the different line shape of the annealed sample reflecting the intrinsic electronic structure, it is therefore imaginable, that a valence hybridization of Mn in (Ga,Mn)As is present. Mn on substitutional sites appears to be not only in a dominate $3d^5$-configuration, but also in at least one other valency, whose spectroscopical fingerprint is mainly located 2.2 eV below E_F. Bearing in mind that the 3*d*-count has been determined to be slightly larger than five,[69,166] a certain amount of Mn_{sub} appears to be in a $3d^6$-state. This seems to be counterintuitive, however, taking the covalency of the As-Mn bound into consideration, such a configuration becomes plausible. This, in turn, would give rise to the double exchange mechanism as driving force of the magnetic interaction in (Ga,Mn)As.

Regarding the other essential part of the DE picture, i.e., the impurity band of substitutional Mn, the current data set allows for no conclusion. The impurity band observed by Okabayashi *et al.*[188] 0.5 eV below E_F by means of ARPES is not reflected in the current ResPES data, since so close to E_F no intensity is observed. It is therefore not possible to assign it to either Mn_{sub} or Mn_{int}. However, it can be excluded that the peak at $E_B = -1.2$ eV is derived from interstitial Mn, as predicted by the theoretical calculations,[49] as this energy range, at best, *gains* in intensity upon post-growth annealing and surface preparation.

5.4 Investigation of the Mn 2p core level spectra

After observing a potential valence hybridization in the Mn 3*d*-PDOS, a complementary investigation of the Mn 2*p* doublet by means of core level spectroscopy is intended to give further insight into this issue. Core level XPS is also a might tool to investigate the electronic structure of solids, since low energy excitations in the VB find their resemblance in core level spectra. To this end, and to conclude the XPS studies of Sec. 4.4, the Mn $2p$ doublet shape of differently prepared (Ga,Mn)As samples has been studied by means of XPS ($h\nu = 1486.6\,\mathrm{eV}$, Al K_α).

Bulk plasmon in (Ga,Mn)As

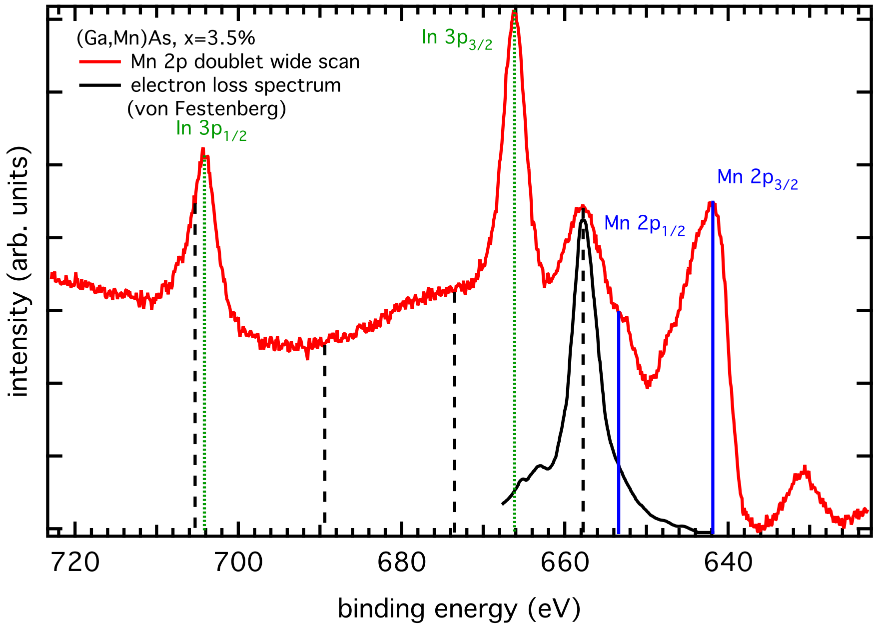

Figure 5.15: *Wide scan of the Mn 2p-doublet. The sample was prepared as described in Sec. 4.4. The positions of the Mn 2p-peaks are indicated by the blue straight lines. The two dominating peaks in the entire scan are due to In contaminations originating from the sample preparation (green dotted lines). The black solid curve shows the electron loss spectrum from von Festenberg.*[113] *Its zero is set to the center position of the Mn* $2p_{3/2}$*-peak. Multiple plasmon excitations, equidistantly spaced by 16 eV, are indicated by the black dashed lines.*

A detailed understanding of the Mn $2p$-spectra is essential for a correct interpretation. For this purpose, Fig. 5.15 depicts a wide scan of the Mn $2p$-doublet. The sample is identically to the one shown in Chap. 4 both regarding Mn content as well as preparation. The Mn $2p_{3/2}$-peak is clearly visible at 641.7 eV. The peak at 657.6 eV is *not* the Mn $2p_{1/2}$-peak since the splitting of 16 eV is too large. Expected values would be 11.3 eV for bulk MnAs and 12.3 eV for MnO. Instead, the shoulder at around 653.4 eV has to be assigned to the Mn $2p_{1/2}$-peak. The In $3p$-doublet (originating from the crept In glue) shows the correct positions as well as the correct intensity ratio. As described in the previous chapter, it dominates the entire spectrum. This complicates the spectral analysis but does not make a qualitative analysis impossible.

The black solid line shows the characteristic electron loss spectrum of von Festenberg for pure GaAs.[113] Due to differences in carrier concentration and effective mass of the charge carriers, the plasmon frequency of (Ga,Mn)As might differ from the value of GaAs. However, these discrepancies are assumed to be of minor importance for a qualitative interpretation.

The zero of the loss function was set to the center position of the Mn $2p_{3/2}$ position. The loss maximum at 16 eV below the main peak coincides perfectly with the peak at 657.6 eV. This strongly suggests that this peak originates from a plasmon excitation. The dashed black lines, equidistantly spaced by 16 eV, give the positions of multiple plasmon excitations.

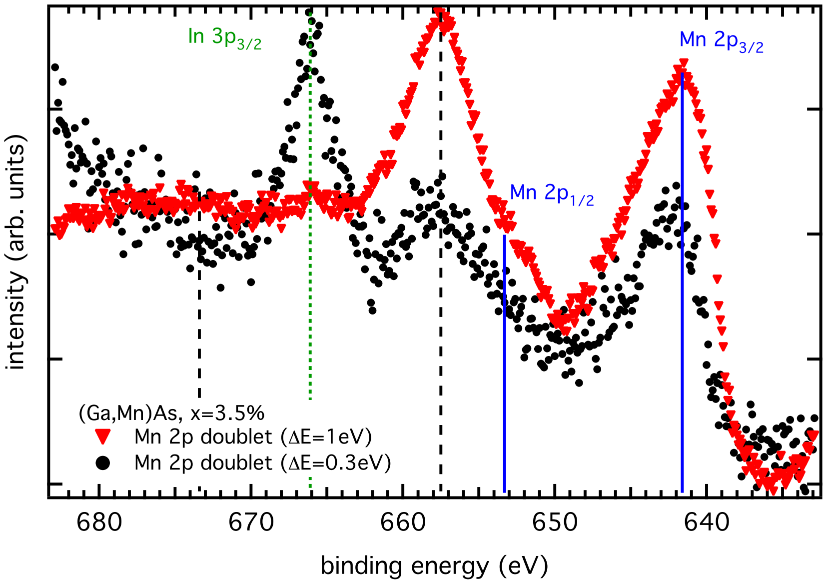

Figure 5.16: *Narrow scan of the Mn 2p-doublet. Red triangles: prepared sample, additionally sputtered to remove the In contamination. The energy resolution was $\Delta E = 1.0$ eV like in the previous spectra. Black circles: the same sample, additionally tempered for 50 h* in situ *in order to retrieve the In contribution. The resolution for this measurement is $\Delta E = 0.3$ eV, close to the maximal resolution of the laboratory setup.*

As described in Sec. 3.2.1 plasmon excitations have to be expected in the spectra. However, when comparing the Mn-related plasmon (note, that the plasmon is a direct consequence of the corresponding main peak) to the As-related (*cf.* Fig. 3.6, the Ga-related shows a similar behavior as the As-related) the intensity is much stronger. For As $3d$ the intensity ratio is around 0.15. For Mn $2p_{3/2}$ it is more than 0.5. The energy dependence described in Sec. 3.2.1 would suggest a value smaller than 0.15 since the Mn $2p$ core level has a higher binding energy, i.e., the photoelectrons have a lower kinetic energy. Moreover, only the first order plasmon is observed, since the second is superposed by In structures and the third order already does not show significant intensity. In contrast to the present results, a similar strong plasmon was not observed in the HAXPES study.

It can furthermore be excluded that the structure is related to contaminations, e.g., In. The red triangles in Figure 5.16 shows a Mn $2p$-spectrum for a clean and additionally sputtered (Ga,Mn)As sample. The In contributions at 666.1 eV are drastically reduced. However, the satellite at 657.6 eV remains unaffected. Upon additional *in situ* tempering for 50 h, the In contaminations reappear at 666.1 eV in the spectra (black circles in Fig 5.16).

Besides the features known from Fig. 5.15, the clean sample (red line) now allows to investigate the higher binding energy range ($683 - 663$ eV). Within this range two structures are apparent. The small peak at 666.1 eV would correspond to the plasmon related to the Mn $2p_{1/2}$-peak, if it is assumed that the In contaminations are completely suppressed. The second structure at 673.5 eV corresponds to an energy loss of twice the bulk plasmon energy of 16 eV from the Mn $2p_{3/2}$ position. As for the former, remaining In contributions cannot entirely be excluded. For the latter, however, such residual In spectral weight is insignificant. It is therefore interpreted as the second order bulk plasmon related to the Mn $2p_{3/2}$ core level.

Valence hybridization in the Mn $2p$ doublet XPS spectra

As has been shown, the Mn $2p$ doublet XPS spectra differs from the HAXPES spectra, as the former contains much more structures, which are obviously suppressed in the latter. However, the thorough analysis in the previous paragraph gives a detailed understanding of the spectral shape which now allows for an investigation of the Mn valency in core level spectra.

The possibility of several chemical Mn species producing the complex Mn $2p$-spectra is addressed in Fig. 5.17. It shows a set of Mn $2p$-spectra of as-grown and annealed samples, both untreated (no *ex situ* or *in situ* surface cleaning) and treated (*ex situ* wet-chemical etching and *in situ* sputtering and tempering according to Sec. 4.4). The untreated surfaces are clearly dominated by oxidized Mn (*cf.* Sec. 5.1). The spectra show a peak corresponding to MnO for both spin-orbit components, even the charge-transfer satellites 4.9 eV below the main lines, is observed.[118] The as-grown sample (black line) shows a residual signal of intrinsic Mn at lower BE of both core level peaks, whereas this contribution is nearly completely suppressed for the *ex situ* annealed sample (blue line). The plasmon peak is masked by the CT satellite of the Mn $2p_{1/2}$-peak.

Upon surface treatment, the spectral shape changes dramatically. The Mn $2p_{3/2}$ core level gains in width and the Mn $2p_{1/2}$ core level is shifted by 3 eV to lower BE. The CT satellite of the oxidized Mn vanishes and the plasmon peak becomes apparent at 657.7 eV.

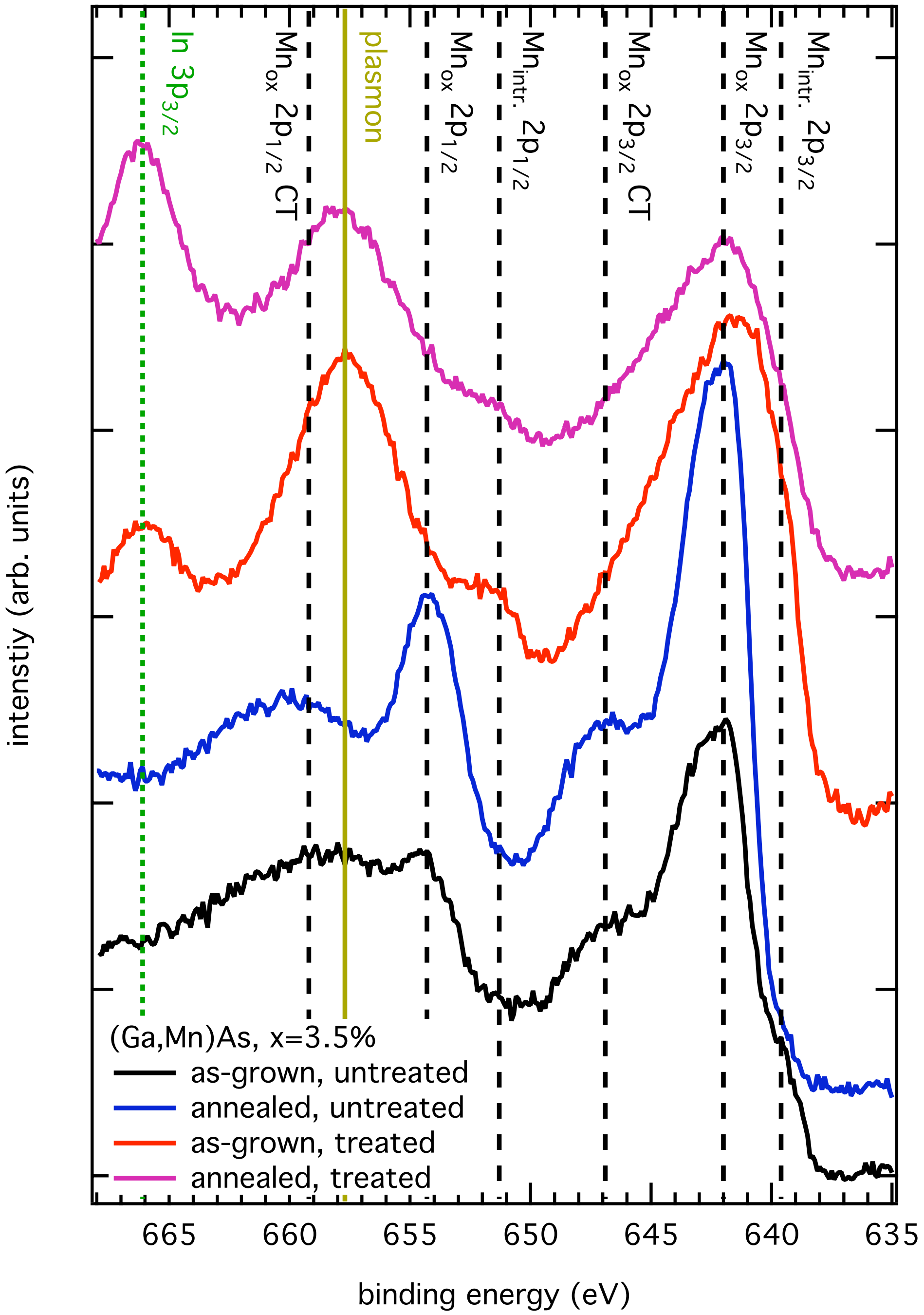

Figure 5.17: *Comparison of the Mn* $2p$*-doublet in the course of sample treatment. In both the as-grown and post-growth annealed samples (black and blue line) the plasmon is overlayed by the CT of the Mn* $2p_{1/2}$ *core level. The plasmon appears only after surface cleaning (removal of passivated Mn) and is slightly higher compared to the Mn* $2p_{3/2}$ *main peak for the annealed sample (purple line). The plasmon is hence an inherent feature of* Mn_{sub}.

These findings are all in accordance to the previous chapter. The sample surface is free of oxidized Mn and the spectra represent the bulk properties of Mn in (Ga,Mn)As. Therefore, the very broad Mn $2p_{3/2}$-peak is an intrinsic feature of bulk (Ga,Mn)As and not caused by Mn-oxides or surface species. Furthermore, multiplet splitting alone can also be ruled out as the source of the broadening. As stated in Sec. 3.2.3, the splitting is proportional to the *d*-electron count. Thus, divalent Mn in MnO has the largest splitting and, as a consequence, the largest broadening, as reported in the literature.[190] Since MnO obviously dominates the untreated spectra and shows much sharper peaks, multiplet splitting cannot be the only reason for the broad Mn $2p_{3/2}$-peak of the clean samples.

Therefore, the presence of several different Mn species becomes reasonable. The resolution in the current experiment is too low to identify different Mn valences within the broad peak. However, a superposition of several Mn valences caused by a valence hybridization, can explain the line broadening. A chemical shift of the first order momentum between two different valences would result in the observation of a single broad, unresolved peak. The different multiplet splitting of the two species would lead to a further smear out of the single peaks. Moreover, the congruent spectra of treated as-grown (red line in Fig. 5.17) and annealed (purple line) samples show that the absence of interstitial Mn in the annealed sample does not change the peak width. This further proves that the broadening is an intrinsic feature of (Ga,Mn)As, not linked to, e.g., interstitial Mn.

In summary, the XPS studies on the Mn $2p$-doublet further support the findings of the ResPES experiments of the previous section. Optimally prepared samples, i.e., post-growth annealed and treated, show broad Mn $2p$ peaks, which can readily be explained by a valence hybridization. An experimentally unresolved superposition of two different Mn valence states in the spectra appears to be the reason for the broad line shapes. The exact valences cannot be determined in a qualitative analysis of the spectra but require further theoretical investigations. However, the comparison to Mn in pure $3d^5$-configuration (MnO) (*viz.* spectra of oxidized samples in Fig. 5.17) shows a shift of the main centroid to *lower* binding energies, which indicates a more strongly screened core potential. This, together with the dominantly covalent character of the bound between Mn and As indicates a $3d$-electron count larger than five.

It is also proven, that the broad line shapes are an inherent feature of bulk (Ga,Mn)As and not an artifact of interstitial Mn, as annealed samples show even wider peaks than as-grown samples. In any case, such an observation cannot be explained by a pure $3d^5$-configuration of substitutional Mn. Thus, the XPS data further support an interpretation of the ferromagnetic ordering in terms of a double exchange mechanism, as they point toward a valence hybridization d^5-d^6 as the reason for the observed broad line shape, which is the key characteristic of the DE model.

6 Temperature dependent transport measurements on (Ga,Mn)As

6.1 Doping dependence of the resistivity

As stated in the introduction, transport and magnetic properties are strongly interlinked in (Ga,Mn)As. From the early stage, transport measurements have provided fruitful information on the physics of DMS.[23] In order to complete the microscopic picture from spectroscopy as presented in the previous sections, complementary temperature dependent transport measurements have been conducted in order to gain insight into the macroscopic properties. The results for three different doping levels are shown in Fig. 6.1.[191]

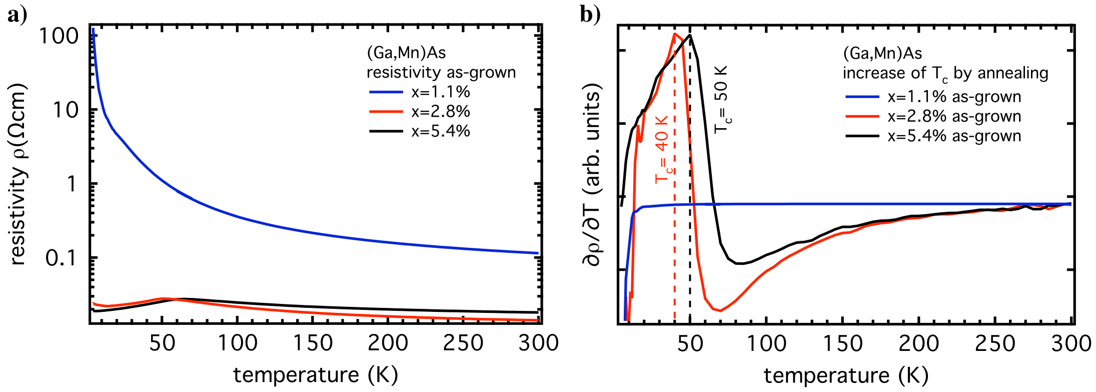

Figure 6.1: *Doping dependence of the $\rho(T)$-curve. Panel (a): resistivity curves of three* as-grown *(Ga,Mn)As samples with various doping levels. Panel (b): derivative $\partial\rho/\partial T$ of the curves in panel (a). The maximum of the derivative gives the exact position of T_c according to Ref. 103.*

The general behavior of the resistivity in Fig. 6.1 (a) is very similar to the earliest results on (Ga,Mn)As by Matsukura and co-workers,[23] as depicted in Fig. 2.7. The 2.8 % and 5.4 % samples show metallic behavior, whereas the 1.1 % sample is obviously on the insulating side of the metal-insulator-transition (MIT). Metallic behavior is in this case defined as a decreasing resistivity by lowering the temperature. For the metallic samples, also a clear peak in the resistivity curve is observed. The origin of this prominent peak in the $\rho(T)$-curve is still under debate. Some authors attribute the peak to scattering of carriers by spin fluctuations,[23,77,103] whereas others explain it in terms of spin-disorder scattering.[56]

Interestingly, the peak is located near T_c,[23] however, not exactly at T_c, as occasionally assumed in the literature.[192] Actually, T_c is slightly lower than the position of the peak. This becomes apparent, when the derivative of the $\rho(T)$-curve is calculated [panel (b)]. The theoretical framework of the resistivity curve gives a point singularity in $\partial\rho/\partial T$, which reflects the exact position of T_c.[103] A singularity is experimentally not observed, but the maximum is smeared out. However, T_c is easily determined for the two higher doped samples to be 40 K (2.8 %) and 50 K (5.4 %), respectively. The determination of T_c via the resistivity curves is an accepted way complementary to magnetometric measurements.

The 5.4 % sample shows clearly a larger value for T_c. In the high-temperature region, however, the resistivity lies above the one of the 2.8 % sample, even though the carrier concentration should be larger. Increasing scattering by the larger amount of impurities and increasing crystal imperfections due to the higher Mn content is made responsible for the throughout larger resistivity of the higher doped sample. For the 1.1 % sample, no structures are observed in the resistivity or its derivative. This suggests, that this sample does not show magnetic ordering, although samples with lower Mn content have been reported to be ferromagnetic yet insulating.[23] Magnetometric data are not available for comparison, thus the sample has to be assumed to be non-magnetic.

In conclusion, the samples presented here, show the expected behavior and give a snapshot of the (Ga,Mn)As phase diagram in Fig. 2.6. Both the metallic character and the determined Curie temperatures of the two higher doped samples are in accordance with numerous reports in the literature. Metallic transport of the lower doped sample would probably require a further improvement of the growth procedure.

6.2 Annealing dependence of the resistivity

After the characterization of the as-grown samples the effects of post-growth annealing according to the procedure described in Sec. 2.2.4 have been investigated. The main results are shown in Fig. 6.2.

The figure shows the three samples from the previous section both as-grown as well as annealed for different times (100 h and 250 h, respectively). In case of the 1.1 % sample, little changes are observed. The resistivity is reduced over the entire temperature range, however, it is still insulating. No maximum becomes apparent in panel (b), showing that the sample is still non-magnetic, even after 100 h of annealing. For the 5.4 % sample, the Curie temperature increases from 50 K to 80 K, as shown in the derivative plot in panel (b). However, the resistivity curve of the annealed sample is above the as-grown sample in the higher temperature range. The 2.8 % sample was annealed for 250 h in order to get insight into the process occurring when (Ga,Mn)As is annealed longer than assumed to be optimal. Here, T_c increases by only 5 K after 250 h of annealing. In the

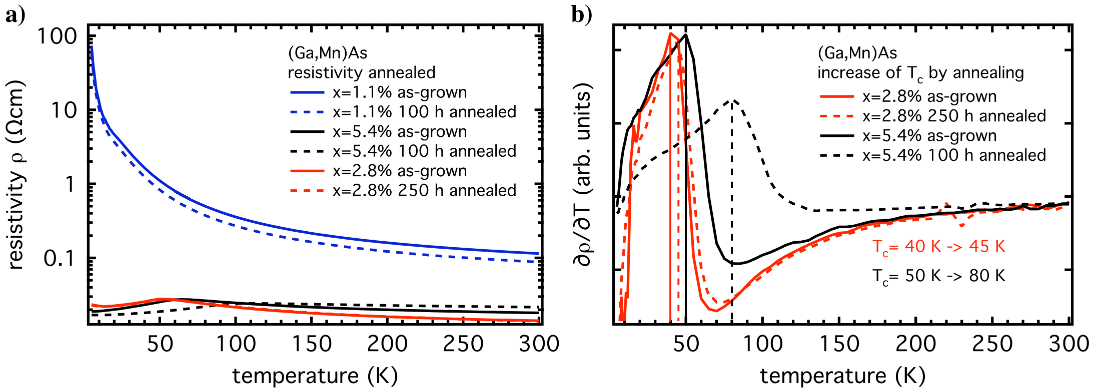

Figure 6.2: *Changes in the resistivity curves upon post-growth annealing. The samples from the previous section have been annealed* ex situ *under oxidative atmosphere. Panel (a) shows the resistivity curve, whereas panel (b) shows the derivative. Values for T_c are indicated. The values for the annealed 2.8 % sample in panel (a) (red dashed line) lie on top of the as-grown data (red solid line).*

high temperature range, no significant change is observed. This is why the annealed data are hidden by the *as-grown* data in the plot of Fig. 6.2 (a).

In the case of the 1.1 % sample, the annealing did not lead to metallic behavior. This indicates that even a removal of compensating interstitial Mn defects provides not enough carriers. The Mn content itself is too low. The increase of T_c of the 5.4 % sample is expected, however, the increase of the resistivity in the high temperature region is in clear opposition to the data reported by Edmonds *et al.*[95] A possible explanation lies in the data of the 2.8 % sample. Here, the increase of the Curie temperature by only 5 K after 250 h upon annealing shows that the annealing was inefficient. The lower Mn content already suggests that the increase will be smaller than for higher Mn concentrations due to the smaller amount of defects, 5 K is, however, very small. As reported in Sec. 5.1 annealing for excessive times $\geq$ 100 h has negative consequences on the sample quality. The segregation of substitutional Mn becomes noticeable and phase separation can occur. The small change in the magnetic and transport properties is therefore explained by those negative effects caused by the "*over*-annealing".

Within this framework, a similar scenario can be imagined for the 5.4 % sample. The annealing leads to an out-diffusion of interstitial Mn and thus, larger areas of the sample show collective ferromagnetism. The SQUID data in Sec. 5.1 already showed that the maximal T_c is reached after 100 h. However, transport measurements are much more sensitive to defects. Small defects, such as MnAs precipates, can alter the ρ-signal, before other techniques can detect a negative effect of the annealing. Thus, shorter times are required for optimal transport properties. Further, also the thickness of the (Ga,Mn)As film determines the time scale.[96]

Further evidence for this claim comes from the time resolved annealing study of the 2.8 % sample in Fig. 6.3. Here, the higher temperature branch of the $\rho(T)$-curve was

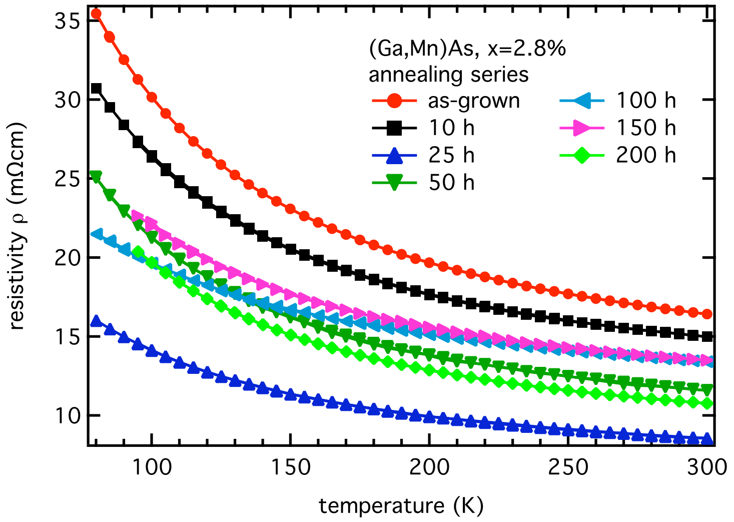

Figure 6.3: *Annealing time series for a 2.8 % (Ga,Mn)As. The resistivity has been measured down to liquid nitrogen temperature. The various annealing times give a snapshot of the evolution of the transport properties with annealing time.*

measured down to liquid nitrogen temperature for several pieces of one and the same 2.8 % wafer, which have been annealed for various times.

As expected, the resistivity decreases monotonically from the as-grown to the 25 h annealed sample. Subsequently, the resistivity steadily increases up to the 150 h annealed sample, followed by a drop for the 200 h annealed sample. Obviously, other processes besides the simple out-diffusion of Mn_{int} gain significance for longer annealing times. It is conceivable, as stated above, that Mn_{sub} segregation, precipates, or other crystal defects are initiated.

The results of the transport measurements on annealed samples outline the necessity to investigate the processes taking place during annealing by complementary methods. If the segregation is only determined by means of PES via the stoichiometry, it was shown in Sec. 2.2.4 that saturation of the Mn segregation is reached after 150 h. On the other hand, SQUID measurements (*cf.* Sec. 5.1) showed the highest T_c after 100 h. The resistivity curves in Fig. 6.3 lead to the conclusion that the optimal annealing time is 25 h. It is therefore clear, that due to the complex interplay between annealing time and temperature, the annealing procedure requires further improvement.

6.3 Low temperature behavior of the resistivity

The interest is now focused on the low-temperature part of the resistivity curves, since this region contains several additional information. For instance, little can be said about the insulating 1.1 % sample in Sec. 6.1, as neither a peak in the resistivity curve nor a

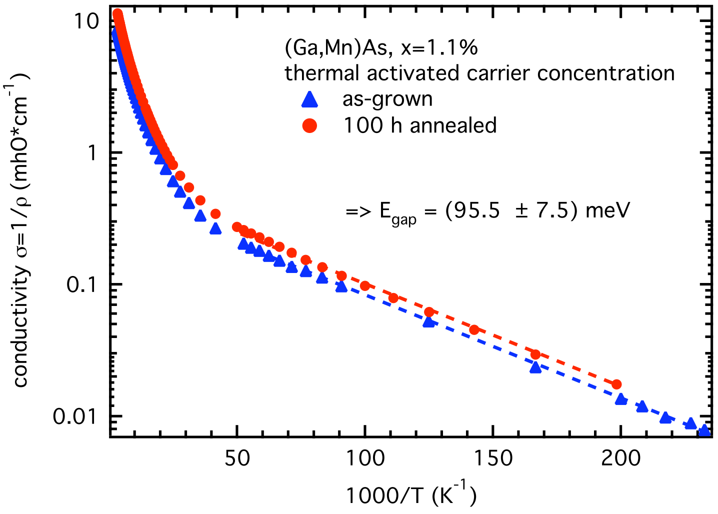

Figure 6.4: *Conductivity of the* 1.1 % *sample in a Arrhenius plot; blue triangles: as-grown sample, red circles:* 100 h *annealed sample.*

maximum in the derivative was observed. When re-analyzing the data with the help of an Arrhenius-plot as in Fig. 6.4, interesting conclusions can be drawn. The linear slope indicates that the carriers are thermally activated via an exponential function $(\exp\{(-E_{gap})/2k_BT\})$. A linear fit to the data gives an activation energy of 95.5 meV, which is in perfect agreement with the literature value of 95 meV.[9]

The gradient from $5-20$ K proves that the carrier generation is thermally activated in this sample and behaves like a conventional doped semiconductor. Furthermore, the slope of the gradient does not change upon annealing, further supporting the assumption that the annealed 1.1 % sample is still insulating (semiconducting). The impurity states do not show an overlap of their wave functions forming an impurity band, but remain isolated impurity states.

But not only the low-temperature resistivity of insulating samples, also metallic samples exhibit an interesting behavior. Already apparent in Fig. 6.1, upon cooling the resistivity decreases, only to increase again for the lowest temperatures ($\leq$ 10 K). In particular this ascent has spurred a lot of interest. Three entirely different models have been prosed since 1997. First investigations by van Esch and co-workers[56] at very low temperatures led to the conclusion that the carrier transport is governed by variable-range hopping. This model is similar to a mechanism proposed by Mott in 1972 for extrinsic semiconductors.[20] In this model, the holes hop directly from impurity to impurity. The resistivity is then given by:[20,56]

$$\rho(T) = \rho_0 \exp\left[\left(\frac{T_0}{T}\right)^{1/4}\right] \tag{6.1}$$

The most interesting point in this approach is that it is in line with the presence of an impurity band, supporting the DE picture.

The second model is based on a Kondo effect in (Ga,Mn)As,[193,194] where polarized holes are scattered by the free local moments, represented by antiferromagnetically coupled Mn_{int}-Mn_{sub} pairs. In this case, one ends up with a temperature dependence of ρ as:

$$\rho(T) = \alpha \ln(T) \tag{6.2}$$

where α is a material specific constance.

The third, and latest, model by Honolka *et al.*[195] is a 3D scaling theory of Anderson's transition in the presence of spin scattering in semiconductors. Within this model, a large fraction of the carriers stays delocalized or weakly localized even down to the mK-region. Within this model, the temperature behavior of the conductivity reads:[195]

$$\rho(T) \propto T^{-1/3} \tag{6.3}$$

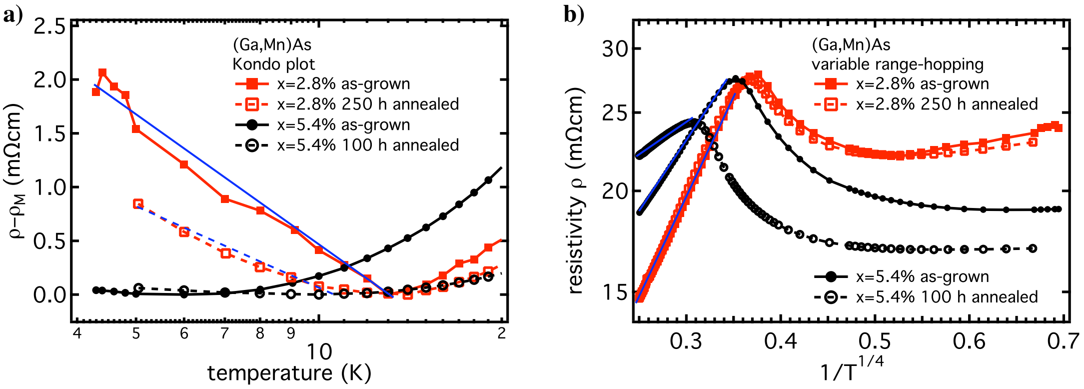

Figure 6.5: *Comparison of the low-T part of the resistivity curves. The left panel gives a plot of* ρ *over* $\log T$*, which would indicate the presence of a Kondo-effect, where* $\rho = \alpha \ln T$*.*[194] *The right panel gives a plot in which* $\log \rho$ *is shown over* $1/T^{1/4}$*, which would give hints to a variable-range hopping mechanism.*[56]

Figure 6.5 shows two plots of the resistivity data from Figs. 6.1 and 6.2. The data and axes have been scaled in a way appropriate for the Kondo-model [panel (a)] and Mott-model [panel (b)]. Technically, the data fit both models equally well. For the Kondo-model, the normalized resistivity (resistivity minus minimum-resistivity) gives a straight line [blue lines in Fig. 6.5 (a)] when plotted over $\log T$ between 4 K and the temperature of the resistivity minimum T_M ($\approx 10-15$ K). Straight lines are also obtained when plotting $\log \rho$ over $1/T^{1/4}$, as expected in the Mott-model.[56,196]

However, a closer inspection of the plots reveals a physical reason against the Kondo-model. The scattering centers in this model are Mn_{int}-Mn_{sub} pairs. Therefore, annealing, which leads to a reduction of the interstitial Mn, should result in a lower slope. This seems to be correct for the 2.8 % sample, but fails for the 5.4 % sample. Since only the amount of Mn_{int} is important, the *over*-annealing is of no relevance. Crystal defects or out-diffusion of Mn_{sub} would only result in a linear offset. The as-grown 5.4 % sample does not show, within the error bars, any slope at all. This is in contradiction to the resistivity curves in Fig. 6.1 which showed that the 5.4 % is affected by a high amount of Mn_{int}. This would predict a higher slope than in the case of the 2.8 % sample, what is clearly not observed. In contrast to this, the agreement with the Mott-model is very good. The resistivity curves give straight lines below the minimum temperature and also the general trend that samples with higher T_c show lower slops is fulfilled.

Unfortunately, the current data cannot be compared to the model of Honolka *et al.*[195] The temperature range is too narrow to allow for a reliable comparison. The authors of Ref. 195 point out that deviations from the variable-range hopping model can only be observed when the resistivity is measured well below 1 K, which is not possible with the present setup. Further measurements with an optimized cryostat are required to test this model.

In summary, it can be stated that transport measurements are an utmost sensitive tool to test the material properties as well as the underlying physics. From the data presented above it has been shown that the annealing is not optimal yet. The amount of interstitial Mn has been dramatically reduced and T_c has reached its maximum after annealing for 100 h. However, the transport measurements showed that obviously other defects have been formed. This further underlines the need to use a set of complementary methods in order to gain a thorough understanding of the processes taking place during post-growth annealing of (Ga,Mn)As.

From the analysis of the low-temperature data it is concluded that the 1.1 % sample is well in the insulating regime, even after annealing, and behaves like a conventional doped semiconductor, presumably due to the low carrier concentration. The activation energy of the Mn acceptors is determined to be 95.5 eV, in excellent agreement with the literature.[9] Furthermore it is observed that variable-range hopping is the dominant conduction mechanism for temperatures below 10 K. This is in line with the presence of an impurity band. As variable-range hopping is present for both the sample with the highest T_c (annealed 5.4 % sample) and the sample which was annealed for 250 h (2.8 % sample), it can safely be assumed to be a intrinsic property of substitutional Mn. Such an impurity band of Mn_{sub} is in contradiction to the unperturbated VB picture, in which the carriers reside in the host VB. Since this is a prerequest of a RKKY interaction, the data presented above, in accordance to the spectroscopical data in the previous chapters, give further evidence that the impurity band – double exchange picture is valid for (Ga,Mn)As.

7 Conclusion and outlook

Besides immense progress in the growth of ferromagnetic (Ga,Mn)As the detailed electronic structure and the possibilities of post-growth sample treatment are widely unexploited. Thus, the main issue of this thesis was threefold.

From the technical point of view, several methods of post-growth surface treatment have been investigated. It was found that various *ex situ* and *in situ* methods are required in order to obtain a clean, stoichiometric, and atomically well-ordered surface. Taking benefit of the individual advantages of wet-chemical etching, ion-milling, and tempering (Ga,Mn)As surfaces of high quality are provided. So, surfaces can reproducibly be restored even after exposure to contaminating air. This means, for instance, that heterostructure fabrication is possible even if the monolithic UHV growth process was interrupted. Furthermore, the cleaning procedure is not only capable to remove the natural grown oxide layer, but also intentional oxidation by post-growth annealing can be countervailed.

Concerning the post-growth annealing protocol, a quantification of the interstitial Mn surface segregation processes was obtained. Using hard x-ray photoemission and reference samples, it was found that the Mn content increases by a factor of 4.3 at the surface. After the removal of the oxide layer, the net loss in Mn was determined to be between $19 - 23\,\%$. It is thus tentatively estimated that in as-grown samples, one out of four to five Mn atoms reside on an interstitial position.

The core level PES results further showed that the simple Mn^{2+} (d^5-configuration) picture is too naive. The system is far from being ionic. The Mn bond has a strongly covalent character with the highest Mn valency appearing to be in $3d^6$-configuration. The broad Mn $2p$ peak shapes clearly show that valence hybridization of Mn are an important and, more importantly, inherent feature of (Ga,Mn)As.

Complementary to the core level PES results, resonant PES data gave further hints for a valence hybridization. In contrast to previous reports, which were mainly investigating as-grown samples, the presented data on annealed samples showed new spectral weight occurring after post-growth annealing. The spectrum is no longer dominated by a Mn $3d^5$ peak but additional intensity is detected at lower binding energies. This is interpreted in the framework of a complex hybridization of various valences in the valence band masked in as-grown sample by defects.

Finally, transport measurements have shown that the post-growth annealing process is not optimal yet. Further fine adjustment of the annealing protocol is to be done until the resistivity data also show optimized electronic properties. Nevertheless, in particular the low-temperature $\rho(T)$ curves are in agreement with early results and suggest that for extremely low temperature variable-range hopping is the dominating conducting mechanism.

Summing up all the fundamental findings, it can be stated that the double exchange mechanism of two substitutional Mn impurities via an anion seems to be the most important driving force for the ferromagnetic coupling. The impurity band – double exchange mechanism shares more characteristics than the valence band – RKKY picture with the complex Mn $d^5 - d^6$ hybridization and indications of a substitutional Mn induced impurity band found in (Ga,Mn)As during the presented study. A complete absence of the RKKY mechanism cannot be proven, however, all experimental results are more consistent with the former model. Also, an interplay of both mechanisms is imaginable.

Despite the important findings in this thesis, several interesting issues still remain. The cleaning procedure has so far been shown to be successful, however, if band-mapping is to be performed, the cleaning has to be further optimized. Then, the way is paved for angle resolved PES measurements to study the $\vec{k}$-resolved band structure. The verification and, especially, the improvement of the early data of Okabayashi *et al.*[188] would help to concretize the double exchange picture in (Ga,Mn)As. The identification of the presumable impurity band and its nature (interstitial or substitutional) is still an open, and challenging, task.

In this sense, this thesis cannot represent a full characterization of (Ga,Mn)As. There is still a lot to be done until the true origin of ferromagnetic coupling is revealed to an sufficient end. Only an ongoing process of the inclusion of the latest findings into theoretical calculations, and, *vice versa*, the test of theoretical predictions in experiments can result in a comprehensive understanding. Only when the driving force of ferromagnetism is clear beyond any doubt, further improvement of the material parameters are possible, and (Ga,Mn)As might make the way to room-temperature DMS devices for future computational architectures.

Bibliography

[1] The International Technology Roadmap for Semiconductors, 2007.

[2] G. E. Moore, Electronics **38** (1965).

[3] G. A. Prinz, Phys. Today **48**, 58 (1995).
G. A. Prinz, Science **282**, 1660 (1998).
S. A. Wolf *et al.*, Science **294**, 1488 (2001).
G. Schmidt and L. W. Molenkamp, Semicond. Sci. Technol. **17**, 310 (2002).

[4] K. Olejník *et al.*, Phys. Rev. B **78**, 054403 (2008).

[5] Y. Ohno *et al.*, Nature (London) **402**, 790 (1999).
H. Ohno *et al.*, Nature (London) **408**, 944 (2000).
D. Chiba *et al.*, Nature (London) **455**, 515 (2008).

[6] H. Ohno *et al.*, Appl. Phys. Lett. **69**, 363 (1996).

[7] V. M. Goldschmidt, Trans. Faraday Society **25**, 253 (1929).

[8] J. S. Blakemore, J. Appl. Phys. **53**, R123 (1982).

[9] S. M. Sze and K. N. Kwok, *Physics of Semiconductor Devices* (John Wiley & Sons Inc., Hoboken, New Jersey, 2007).

[10] D. E. Eastman, T.-C. Chiang, P. Heimann, and F. J. Himpsel, Phys. Rev. Lett. **245**, 656 (1980).

[11] W. F. J. Egelhoff, Surf. Sci. Rep. **6**, 253 (1987).

[12] Z. Liu *et al.*, J. Vac. Sci. Technol. A **21**, 212 (2003).

[13] T. Frey, M. Maier, J. Schneider, and M. Gehrke, J. Phys. C **21**, 5539 (1988).

[14] S. C. Erwin and A. G. Petukhov, Phys. Rev. Lett. **89**, 227201 (2002).

[15] W. Schairer and M. Schmidt, Phys. Rev. B **10**, 2501 (1974).

[16] V. F. Sapega, M. Moreno, M. Ramsteiner, L. Däweritz, and K. H. Ploog, Phys. Rev. B **66**, 075217 (2002).

[17] J. Schneider, U. Kaufmann, W. Wilkening, and M. Baeumler, Phys. Rev. Lett. **59**, 240 (1987).

[18] M. S. Kim and C. H. Park, J. Korean Phys. Soc. **46**, 536 (2005).

[19] S. M. Sze, *Semiconductor devices: Physics and Technology*, 2 ed. (John Wiley & Sons Inc., Hoboken, New Jersey, 2002).

[20] N. F. Mott, Adv. Phys. **21**, 785 (1972).

[21] H. Ohldag *et al.*, Appl. Phys. Lett. **76**, 2928 (2000).

[22] E. J. Singley *et al.*, Phys. Rev. B **68**, 165204 (2003).

[23] F. Matsukura, H. Ohno, A. Shen, and Y. Sugawara, Phys. Rev. B **57**, R2037 (1998).

[24] H. Iwasaki, Y. Mizokawa, R. Nishitani, and S. Nakamura, Jpn. J. Appl. Phys. **17**, 315 (1978).

[25] J. T. Wolan, W. S. Epling, and G. B. Hoflund, J. Appl. Phys. **81**, 6160 (1997).

[26] D. A. Allwood *et al.*, Thin Solid Films **364**, 33 (2000).

[27] T.-B. Ng, D. B. Janes, D. McInturff, and J. M. Woodall, Appl. Phys. Lett. **69**, 3551 (1996).

[28] C. D. Thurmond, G. P. Schwartz, G. W. Kammlott, and B. Schwartz, J. Electro. Chem. Soc. **127**, 1366 (1980).

[29] Z. R. Wasilewski, J.-M. Baribeau, M. Beaulieu, X. Wu, and G. I. Sproule, J. Vac. Sci. Technol. B **22**, 1534 (2004).

[30] M. Yamada and Y. Ide, Surf. Sci. Lett. **339**, L914 (1995).

[31] Y. Asaoka, J. Cryst. Growth **251**, 40 (2003).

[32] M. J. Howes and D. V. Morgan, editors, *Gallium Arsenide*, The Wiley series in solid state devices and circuits No. 1 (John Wiley & Sons Inc., Hoboken, New Jersey, 1985).

[33] J. Massies and J. P. Contour, J. Appl. Phys. **85**, 806 (1985).

[34] Z. Song, S. Shogen, M. Kawasaki, and I. Suemune, J. Vac. Sci. Technol. B **13**, 77 (1995).

[35] W.-X. Chen, L. M. Walpita, C. C. Sun, and W. S. C. Chang, J. Vac. Sci. Technol. B **4**, 701 (1986).

[36] S. J. Pearton, U. K. Chakrabarti, A. P. Perly, and K. S. Jones, J. Appl. Phys. **68**, 2760 (1990).

[37] J. B. Malherbe, Crit. Rev. Solid State Mater. Sci. **19**, 55 (1994).

[38] M. Ohring, *Materials science of thin films*, 2 ed. (Academic Press, New York, London, 2002).

[39] T. D. Bussing, P. H. Holloway, Y. X. Wang, J. F. Moulder, and J. S. Hammond, J. Vac. Sci. Technol. B **6**, 1514 (1988).

[40] G. M. Schott, *Molekularstrahlepitaxie und Charakterisierung von (Ga,Mn)As Halbleiterschichten*, PhD thesis, University of Würzburg, 2004.

[41] J. Wenisch, *Ferromagnetic (Ga,Mn)As Layers and Nanostructures: Control of Magnetic Anisotropy by Strain Engineering*, PhD thesis, University of Wuerzburg, 2008.

[42] J. De Boeck *et al.*, J. Magn. Magn. Mater. **156**, 148 (1996).

[43] T. Tsuruoka *et al.*, Appl. Phys. Lett. **81**, 2800 (2002).

[44] S. Lodha, D. B. Janes, and N.-P. Chen, J. Appl. Phys. **93**, 2772 (2003).

[45] E. R. Weber *et al.*, J. Appl. Phys. **53**, 6140 (1982).

[46] J. H. Park, S. K. Kwon, and B. I. Min, Physica B **281-282**, 703 (2000).

[47] X. Liu *et al.*, Appl. Phys. Lett. **67**, 279 (1995).

[48] H. Ohno, Science **281**, 951 (1998).

[49] F. Maća and J. Mašek, Phys. Rev. B **65**, 235209 (2002).

[50] V. I. Baykov, P. A. Korzhavyi, and B. Johansson, Phys. Rev. Lett. **101**, 177204 (2008).

[51] K. M. Yu *et al.*, Phys. Rev. B **65**, 201303 (2002).

[52] A. Ernst, L. M. Sandratskii, M. Bouhassoune, J. Henk, and M. Lüders, Phys. Rev. Lett. **95**, 237207 (2005).

[53] H. Shimizu, T. Hayashi, T. Nishinaga, and M. Tanaka, Appl. Phys. Lett. **74**, 398 (1999).

[54] M. Kaminska *et al.*, Appl. Phys. Lett. **54**, 1881 (1989).

[55] G. M. Schott, W. Faschinger, and L. W. Molenkamp, Appl. Phys. Lett. **79**, 1807 (2001).

[56] A. van Esch *et al.*, Phys. Rev. B **56**, 13103 (1997).

[57] R. C. Myers *et al.*, Phys. Rev. B **74**, 155203 (2006).

[58] T. Jungwirth *et al.*, Phys. Rev. B **72**, 165204 (2005).

[59] T. Hynninen, M. Ganchenkova, H. Raebiger, and J. von Boehm, Phys. Rev. B **74**, 195337 (2006).

[60] I. Kuryliszyn-Kudelska *et al.*, J. Appl. Phys. **95**, 603 (2004).

[61] T. Ogawa, M. Shirai, N. Suzuki, and I. Kitagawa, J. Magn. Magn. Mater. **197**, 428 (1999).

[62] P. Mavropoulos *et al.*, Phys. Rev. B **69**, 054424 (2004).

[63] J. G. Braden, J. S. Parker, P. Xiong, S. H. Chun, and N. Samarth, Phys. Rev. Lett. **91**, 056602 (2003).

[64] M. A. Ruderman and C. Kittel, Phys. Rev. **96**, 99 (1954).
T. Kasuya, Prog. Theor. Phys. **16**, 45 (1956).
K. Yosida, Phys. Rev. **106**, 893 (1957).

[65] W. K. Heisenberg, Z. Phys. **49**, 619 (1928).

[66] K. Yosida, *Theory of Magnetism* (Springer-Verlag, Berlin, Heidelberg, New York, 1998).

[67] J. Friedel, Nuovo Cimento Suppl. **7**, 287 (1958).

[68] T. Dietl, H. Ohno, F. Mastukura, J. Cibert, and D. Ferrand, Science **287**, 1019 (2000).

[69] T. Jungwirth *et al.*, Phys. Rev. B **73**, 165205 (2006).

[70] C. Zener, Phys. Rev. **81**, 440 (1951).

[71] C. Zener, Phys. Rev. **83**, 299 (1951).

[72] R. Bouzerar, G. Bouzerar, and T. Ziman, Europhys. Lett. **78**, 67003 (2007).

[73] V. I. Litvinov and V. K. Dugaev, Phys. Rev. Lett. **86**, 5593 (2001), Bouzerar2004, Litvinov2004.

[74] G. Alvarez, M. Mayr, and E. Dagotto, Phys. Rev. Lett. **89**, 27202 (2002).

[75] P. Mahadevan and A. Zunger, Phys. Rev. B **69**, 115211 (2004).

[76] K. S. Burch, D. D. Awschalom, and D. N. Basov, J. Magn. Magn. Mater. **320**, 3207 (2008).

[77] B. Beschoten *et al.*, Phys. Rev. Lett. **83**, 3073 (1999).

[78] K. S. Burch *et al.*, Phys. Rev. Lett. **97**, 087208 (2006).

[79] L. P. Rokhinson and Y. Lyanda-Geller, Phys. Rev. B **76**, 161201 (2007).

[80] P. R. Stone *et al.*, Phys. Rev. Lett. **101**, 087203 (2008).

[81] T. Ishiwata, T. Kimura, T. Katsufuji, and Y. Tokura, Phys. Rev. B **57**, R8079 (1998).

[82] K. Alberi *et al.*, Phys. Rev. B **78**, 075201 (2008), Alberi2008a.

[83] A. M. Yakunin *et al.*, Phys. Rev. Lett. **95**, 256402 (2005).

[84] F. Popescu, C. Şen, E. Dagotto, and A. Moreo, Phys. Rev. B **76**, 085206 (2007).

[85] L. Craco, M. S. Laad, and E. Müller-Hartmann, Phys. Rev. B **68**, 233310 (2003).

[86] H. Akai, Phys. Rev. Lett. **81**, 3002 (1998).

[87] C. Zener, Phys. Rev. **82**, 403 (1951).

[88] Y. Ishiwata *et al.*, Phys. Rev. B **71**, 121202(R) (2005).

[89] Y. H. Chang, C. H. Park, K. Sato, and H. Katayama-Yoshida, Phys. Rev. B **76**, 125211 (2007).

[90] J. Inoue, S. Nonoyama, and H. Itoh, Phys. Rev. Lett. **85**, 4610 (2000).

[91] R. Wu, Phys. Rev. Lett. **94**, 207201 (2005).

[92] R. Bouzerar, B. Georges, and T. Ziman, Phys. Rev. B **73**, 024411 (2006).

[93] K. W. Edmonds *et al.*, Phys. Rev. B **71**, 064418 (2005).

[94] K. W. Edmonds *et al.*, Phys. Rev. Lett. **92**, 037201 (2004).

[95] K. W. Edmonds *et al.*, Appl. Phys. Lett. **81**, 3010 (2002).

[96] K. W. Edmonds *et al.*, Appl. Phys. Lett. **81**, 4991 (2002).

[97] B. Schmid *et al.*, Phys. Rev. B **78**, 075319 (2008).

[98] M. Wang *et al.*, Appl. Phys. Lett. **93**, 132103 (2008).

[99] M. Malfait, J. Vanacken, V. V. Moshchalkov, W. Van Roy, and G. Borghs, Appl. Phys. Lett. **86**, 132501 (2005).

[100] F. Kronast *et al.*, Phys. Rev. B **74**, 235213 (2006).

[101] T. Hayashi, Y. Hashimoto, S. Katsumoto, and Y. Iye, Appl. Phys. Lett. **78**, 1691 (2001).

[102] M. Adell *et al.*, Appl. Phys. Lett. **86**, 112501 (2005).

[103] V. Novák *et al.*, Phys. Rev. Lett. **101**, 077201 (2008).

[104] H. Hertz, Ann. Phys. (Leipzig) **267**, 983 (1887).

[105] A. Einstein, Ann. Phys. (Leipzig) **322**, 135 (1905).

[106] S. Hüfner, *Photoelectron spectroscopy*, 3 ed. (Springer-Verlag, Berlin, Heidelberg, New York, 2003).

[107] S. D. Kevan, editor, *Angle-resolved photoemission* (Elsevier, Amsterdam, London, New York, Tokyo, 1992).

[108] A. Damascelli, Phys. Scr. **T109**, 61 (2004).

[109] J. W. Allen, *Resonant photoemission of solids with strongly correlated electrons*Synchrotron Radiation Research: Advances in Surface Science (Plenum Publishing Corporation, 1990), chap. 7.

[110] M. Cardona and L. Ley, editors, *Photoemission in Solids I*, Topics in Applied Physics Vol. 26 (Springer-Verlag, Berlin Heidelberg New York, 1978).

[111] L. Ley and M. Cardona, editors, *Photoemission in Solids II*, Topics in Applied Physics Vol. 27 (Springer-Verlag, Berlin Heidelberg New York, 1979).

[112] H. R. Philipp and H. Ehrenreich, Phys. Rev. **129**, 1550 (1963).

[113] C. v. Festenberg, Z. Phys. **227**, 453 (1969).

[114] M. Henzler, *Oberflächenphysik des Festkörpers* (B. G. Teubner Stuttgart, 1994).

[115] D. Briggs and M. P. Seah, editors, *Practical surface analysis*, 2nd ed. (John Wiley & Sons Ltd., New York, 1990).

[116] P. Steiner, H. Höchst, and S. Hüfner, Z. Physik B **30**, 129 (1978).

[117] S. Tougaard, Surf. Interface Anal. **11**, 453 (1988).

[118] S.-P. Jeng, R. J. Lad, and V. E. Henrich, Phys. Rev. B **43**, 11971 (1991).

[119] B. Hermsmeier *et al.*, Phys. Rev. Lett. **61**, 2592 (1988).

[120] S. P. Kowalczyk, L. Ley, R. A. Pollak, F. R. McFeely, and D. A. Shirley, Phys. Rev. B **7**, 4009 (1973).

[121] J. F. van Acker *et al.*, Phys. Rev. B **37**, 6827 (1988).

[122] M. P. Seah and S. J. Spencer, Surf. Interface Anal. **33**, 640 (2002).
M. P. Seah and R. White, Surf. Interface Anal. **33**, 960 (2002).
M. P. Seah and S. J. Spencer, Surf. Interface Anal. **35**, 515 (2003).
M. P. Seah *et al.*, Surf. Interface Anal. **36**, 1269 (2004).
M. P. Seah, Surf. Interface Anal. **37**, 300 (2005).
M. P. Seah and S. J. Spencer, Surf. Interface Anal. **37**, 731 (2005).
K. J. Kim and M. P. Seah, Surf. Interface Anal. **39**, 512 (2007).

[123] D. A. Shirley, Phys. Rev. B **5**, 4709 (1972).

[124] S. Tougaard, Surf. Interface Anal. **25**, 137 (1997).

[125] C. Fuggle, John and F. A. Santos, Phys. Rev. A **22**, 1615 (1980).

[126] G. Nicolay *et al.*, Phys. Rev. B **62**, 1631 (2000).

[127] P. H. Citrin, G. K. Wertheim, and Y. Baer, Phys. Rev. B **16**, 4256 (1977).

[128] S. Doniach and M. Šunjić, J. Phys. C **3**, 285 (1970).

[129] G. D. Mahan, Phys. Rev. **163**, 612 (1967).

[130] H. Wada and Y. Tanabe, Appl. Phys. Lett. **79**, 3302 (2001).

[131] ASTM*Standard E 673-98, Annual Book of ASTM Standards* Vol. 3.06 (American Society for Testing and Materials, West Conshohocken, Pennsylvania, 2001).

[132] D. R. Penn, J. Electron Spectrosc. Relat. Phenom. **9**, 29 (1976).
D. R. Penn, Phys. Rev. B **13**, 5248 (1976).
J. Szajman, J. Liesegang, J. G. Jenkin, and R. C. G. Leckey, J. Electron Spectrosc. Relat. Phenom. **23**, 97 (1981).
W. H. Gries, Surf. Interface Anal. **24**, 38 (1996).

[133] S. Tanuma, C. J. Powell, and D. R. Penn, Surf. Interface Anal. **11**, 577 (1988).
S. Tanuma, C. J. Powell, and D. R. Penn, Surf. Interface Anal. **17**, 927 (1991).
S. Tanuma, C. J. Powell, and D. R. Penn, Surf. Interface Anal. **21**, 165 (1994).
S. Tanuma, C. J. Powell, and D. R. Penn, Surf. Interface Anal. **25**, 25 (1997).

[134] P. J. Cumpson and M. P. Seah, Surf. Interface Anal. **25**, 430 (1997).

[135] C. E. Mortimer, *Chemistry*, 6 ed. (Wadsworth Publishing Company, 1986).

[136] G. A. Brooks and W. J. Rankin, Metallurgical and Materials Transactions B **25**, 865 (1994).
I. Z. Indutnyi, P. E. Shepeliavyi, and V. I. Indutnyi, Semiconductor Physics, Quantum Electronics & Optoelectronics **2**, 59 (1999).
H. Barten, J. Appl. Cryst. **14**, 68 (1981).
Q. Zhang, J. Lu, J. Wang, and F. Saito, Journal of Materials Science **39**, 5527 (2003).
H. H. Tippins, Phys. Rev. **140**, A316 (1965).

[137] H. Bethe, Ann. Phys. (Leipzig) **397**, 325 (1930).

[138] B. L. Henke, Phys. Rev. A **6**, 94 (1972).

[139] J. Kawai *et al.*, Spectrochim. Acta **47B**, 983 (1992).

[140] B. L. Henke, E. M. Gullikson, and J. C. Davis, Atom. Data Nuc. Data **54**, 181 (1993).

[141] T. A. Carlson and G. E. McGuire, J. Electron Spectrosc. Relat. Phenom. **1**, 161 (1973).

[142] R. Holm and S. Storp, Appl. Phys. A **9**, 217 (1976).

[143] K. Siegbahn *et al.*, *ESCA - Atomic, Molecular and Solid State Structure Studied by Means of Electron Spectroscopy* (Almqvist and Wiksells, 1967).

[144] C. J. Powell, J. Electron Spectrosc. Relat. Phenom. **47**, 197 (1988).

[145] C. J. Powell, A. Jablonski, I. S. Tilinin, S. Tanuma, and D. R. Penn, J. Electron Spectrosc. Relat. Phenom. **98-99**, 1 (1999).

[146] A. Jablonski and C. J. Powell, J. Electron Spectrosc. Relat. Phenom. **100**, 137 (1999).
A. Jablonski and C. J. Powell, J. Electron Spectrosc. Relat. Phenom. **107**, 201 (2000).
C. J. Powell and A. Jablonski, Surf. Interface Anal. **33**, 211 (2002).

[147] R. J. Baird, C. S. Fadley, S. Kawamoto, and M. Metha, Chem. Phys. Letters **34**, 49 (1975).

[148] C. S. Fadley, R. J. Baird, W. Siekhaus, T. Novakov, and S. Å. L. Bergström, J. Electron Spectrosc. Relat. Phenom. **4**, 93 (1974).

[149] N. Yamamoto and J. C. H. Spence, Thin Solid Films **104**, 43 (1983).

[150] M. Gajdardziska-Josifovska *et al.*, Ultramicroscopy **50**, 285 (1993).

[151] Y. C. Wang, T. M. Chou, M. Libera, and T. F. Kelly, Appl. Phys. Lett. **70**, 1296 (1997).

[152] J. Chung and L. Rabenberg, Appl. Phys. Lett. **88**, 013106 (2006).

[153] C. S. Fadley, Prog. Surf. Science **16**, 275 (1984).

[154] M. F. Ebel, G. Moser, H. Ebel, A. Jablonski, and H. Oppolzer, J. Electron Spectrosc. Relat. Phenom. **42**, 61 (1987).

[155] H. Ebel, M. F. Ebel, J. Wernisch, and A. Jablonski, Surf. Interface Anal. **6**, 140 (1984).

[156] A. Jablonski, M. F. Ebel, and H. Ebel, J. Electron Spectrosc. Relat. Phenom. **42**, 235 (1987).

[157] A. Jablonski and C. J. Powell, Surf. Sci. Rep. **47**, 33 (2002).

[158] W. H. Gries and W. Werner, Surf. Interface Anal. **16**, 149 (1990).

[159] J. J. Yeh and I. Lindau, Atom. Data Nuc. Data **32**, 1 (1985).

[160] H. Ebel, M. F. Ebel, and A. Jablonski, J. Electron Spectrosc. Relat. Phenom. **35**, 155 (1985).

[161] A. Jablonski and H. Ebel, Surf. Interface Anal. **11**, 627 (1988).

[162] N. M. Ravindra and D. L. Weeks, R. A. Kinser, Phys. Rev. B **36**, 6132 (1987).

[163] K. Roensch, *Entstehung und Wachstum von atomaren Nanodrähten aus Platin auf Ge (001)*, Master's thesis, University of Würzburg, 2009.

[164] A. Jablonski, Surf. Interface Anal. **14**, 659 (1989).

[165] F. Maccherozzi *et al.*, Phys. Rev. B **74**, 104421 (2006).

[166] J. Okabayashi *et al.*, Phys. Rev. B **58**, R4211 (1998).

[167] O. Rader *et al.*, Phys. Rev. B **69**, 075202 (2004).

[168] J. B. Malherbe, Crit. Rev. Solid State Mater. Sci. **19**, 129 (1994).

[169] J. B. Malherbe and W. O. Barnard, Surf. Interface Anal. **18**, 491 (1992).

[170] I^{2}R, *GLOVE BAG, inflatable glove chamber, model: X-27-27.*

[171] S. Engelbrecht, *Untersuchung der elektronischen Struktur von Ferromagnet-Halbleiter-Hybridsystemen mittels Photoelektronenspektroskopie*, Master's thesis, University of Würzburg, 2008.

[172] M. Adell, J. Adell, L. Ilver, J. Kanski, and J. Sadowski, Appl. Phys. Lett. **89**, 172509 (2006).

[173] F. Maccherozzi *et al.*, Surf. Sci. **601**, 4283 (2007).

[174] H. Raebiger, M. Ganchenkova, and J. von Boehm, Appl. Phys. Lett. **89**, 012505 (2006).

[175] W. Drube, T. M. Grekh, R. Teusch, and G. Materlik, J. Electron Spectrosc. Relat. Phenom. **88-91**, 683 (1998).

[176] W. Limmer *et al.*, Phys. Rev. B **71**, 205213 (2005).

[177] S. Hatfield *et al.*, Surf. Sci. **585**, 66 (2005).

[178] M. A. Stranick, Surf. Sci. Spec. **6**, 39 (1999).
M. A. Stranick, Surf. Sci. Spec. **6**, 31 (1999).

[179] P. Ravindran *et al.*, Phys. Rev. B **59**, 15680 (1999).

[180] S. Ueda *et al.*, Physica E **10**, 210 (2001).

[181] Y. Takagaki, E. Wiebicke, L. Däweritz, and K.-H. Ploog, Appl. Phys. A **76**, 837 (2003).

[182] J. Okabayashi *et al.*, Phys. Rev. B **59**, R2486 (1999).

[183] O. Rader *et al.*, Phys. Stat. Sol. B **246**, 1435 (2009).

[184] K. Nakamura, K. Hatano, T. Akiyama, and T. Ito, Phys. Rev. B **75**, 205205 (2007).

[185] H. Åsklund, L. Ilver, J. Kanski, J. Sadowski, and R. Mathieu, Phys. Rev. B **66**, 115319 (2002).

[186] M. Adell, J. Adell, L. I. and. J. Kanski, J. Sadowski, and J. Z. Domagala, Phys. Rev. B **75**, 054415 (2007).

[187] M. Adell *et al.*, Phys. Rev. B **70**, 125204 (2004).

[188] J. Okabayashi *et al.*, Phys. Rev. B **64**, 125304 (2001).

[189] K. Ono *et al.*, J. Appl. Phys. **91**, 8088 (2002).

[190] S. P. Kowalczyk, L. Ley, F. R. McFeely, and D. A. Shirley, Phys. Rev. B **11**, 1721 (1975).

[191] H. Fink, *Temperaturabhängige Leitfähigkeitsmessungen und Entwicklung eines Apparates zur in situ Leitfähigkeitsmessung*, Master's thesis, University of Würzburg, 2008.

[192] C. P. Moca *et al.*, Phys. Rev. Lett. **102**, 137203 (2009).

[193] J. Kondo, Prog. Theor. Phys. **32**, 37 (1964).

[194] H. T. He *et al.*, Appl. Phys. Lett. **87**, 162506 (2005).

[195] J. Honolka, S. Masmanidis, H. X. Tang, D. D. Awschalom, and M. L. Roukes, Phys. Rev. B **75**, 245310 (2007).

[196] L. Chen *et al.*, Appl. Phys. Lett. **95**, 182505 (2009).

List of publications and conference contributions

2007

Talk at the DPG Spring Meeting, Regensburg

Title: *Investigation of different Mn states in $Ga_{1-x}Mn_xAs$ by HX-PES*
Authors: **B. Schmid**, A. Müller, M. Sing, R. Claessen, J. Wenisch, K. Brunner, M. Molenkamp, W. Drube

Poster presentation at the VUV XV conference, Berlin

Title: *Hard x-ray photoemission study of the diluted magnetic semiconductor GaMnAs*
Authors: **B. Schmid**, A. Müller, M. Sing, R. Claessen, J. Wenisch, K. Brunner, M. Molenkamp, W. Drube

2008

Talk at the DPG Spring Meeting, Berlin

Title: *Influences of thermal treatment on the As valence in MnAs thin films on GaAs substrate*
Authors: **B. Schmid**, S. Engelbrecht, M. Paul, M. Sing, R. Claessen, J. Wenisch, C. Gould, K. Brunner, M. Molenkamp, W. Drube

Physical Review B 78, 075319 (2008)

Title: *Surface segregation of interstital manganese in $Ga_{1-x}Mn_xAs$ studied by hard x-ray photoemission spectroscopy*
Authors: **B. Schmid**, A. Müller, M. Sing, R. Claessen, J. Wenisch, C. Gould, K. Brunner, M. Molenkamp, W. Drube

2009

Poster presentation at the DPG Spring Meeting, Dresden

Title: *Effects of thermal treatment on the electronic structure of $Ga_{1-x}Mn_xAs$*
Authors: **B. Schmid**, D. Fertig, S. Engelbrecht, M. Sing, R. Claessen, L. Ebel, C. Gould, K. Brunner, M. Molenkamp

Acknowledgment

At the end, I would like to thank:

Prof. Dr. Ralph Claessen, for the chance to contiue my research in such a intersting and fascinating field.

Dr. Michael Sing for the inspiring discussion, his sheer unlimited vocabulary, and for correcting the manuscript of this thesis.

Prof. Dr. Laurens W. Molenkamp, **Prof. Dr. Karl Brunner**, **Dr. Charles Gould**, **Dr. Jan Wenisch** and, **Lars Ebel** for all the (Ga,Mn)As samples, various microscopy and SQUID measurements.

Dr. Wolfgang Drube, **Heiko Schulz-Ritter**, and **Mike Sperling** for the support during the beamtimes at HASYLAB and BESSY.

Holger Fink for the transport measurements.

Monika Seifer for her kindness and helpfullness.

Alexey Shuvaev for the introduction into Russian philosophy.

Thomas Demarczyk for his colleagueship and the matutial psychotherapies.

Markus Paul for all the frustrating discussions and his friendship.

Andreas Müller, **Sebastian Engelbrecht**, **Nadine Schütz**, **Dominic Fertig**, and **Michael Eitel**, my "whelps", for their work and their challenging and perserving curiosity.

All group members (former and current) of **EP4** for the working atmosphere.

Corina Kabitschke for the critical reading of the manuscript.

All my friends and my family for their support during the last 4 years.

Curriculum Vitae

Personal details

Name: Benjamin Schmid
Date of birth: December 5, 1979
Place of birth: Augsburg
Nationality: German
Marital status: single

Education

1986 – 1990: Grundschule in Augsburg
1990 – 1999: Jakob-Fugger Gymnasium in Augsburg
1999 – 2000: Military service at the 220th transport batalion, Günzburg
2000 – 2006: Diploma study in physics, University of Augsburg
topic of Diploma thesis: *Electron and X-ray spectroscopy of ferromagnetic semiconductors*
Supervisor: Prof. Dr. Ralph Claessen
2004 – 2006: Study at the University of Osaka, Japan
Supervisor: Prof. Dr. Shigemasa Suga
2006 – 2010: Ph.D. work at the Physikalisches Institut, University of Würzburg

Eidesstattliche Erklärung

Hiermit versichere ich an Eides statt, dass ich die vorliegende Dissertation eigenständig angefertigt habe und keine anderen als die angegebenen Quellen und Hilfsmittel benutzt habe.

Würzburg, 31.03.2010

Benjamin Schmid

Erklärung

Hiermit erkläre ich, dass ich die vorliegende Dissertation nicht in gleicher oder anderer Form bereits in einem anderen Fach vorgelegt habe.

Würzburg, 31.03.2010

Benjamin Schmid